Lawrence Berkeley National Laboratory

Title

Geotechnical Support and Topical Studies of Nuclear Waste Geologic Respositories: Annual Report, Fiscal Year 1988

Permalink

https://escholarship.org/uc/item/0qj4738m
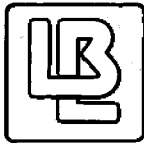
Author

Lawrence Berkeley National Laboratory

Publication Date

1989

Lawrence Berkeley Laboratory

UNIVERSITY OF CALIFORNIA

EARTH SCIENCES DIVISION

Geotechnical Support and Topical Studies of
Nuclear Waste Geologic Repositories:
Annual Report, Fiscal Year 1988

January 1989

DISCLAIMER

GEOTECHNICAL SUPPORT AND TOPICAL STUDIES

FOR NUCLEAR WASTE GEOLOGIC REPOSITORIES

Annual Report, Fiscal Year 1988

Earth Sciences Division
Lawrence Berkeley Laboratory
1 Cyclotron Road
Berkeley, California 94720

Prepared for

Office of Civilian Radioactive Waste Management
Office of Facilities Siting and Development
Siting and Facilities Technology Division
U.S. Department of Energy

January 1989

Table of Contents

Executive Summary

Chin-Fu Tsang

This multidisciplinary project was initiated in fiscal year 1986. It comprises two major interrelated tasks:

1. Technical Assistance. This part of the project includes: (a) reviewing the progress of the Yucca Mountain project in the DOE Office of Civilian Radioactive Waste Management (OCRWM) Program and advising the Engineering and Geotechnology Division on significant technical issues facing it; (b) analyzing geotechnical data, reports, tests, surveys and plans for the Yucca Mountain project; (c) reviewing and commenting on major technical reports and other program documents such as Study Plans; and (d) providing scientific and technical input at technical meetings.

2. Topical Studies. This activity comprises studies on scientific and technical topics, and issues of significance to in-situ testing, test analysis methods, and site characterization of nuclear waste geologic repositories. The subjects of study were selected based on discussions with DOE staff. Currently the major task, with subtasks involving various geoscience disciplines, is a study of the mechanical, hydraulic, geophysical and geochemical properties of fractures in geologic rock masses. One additional topic, initiated at DOE's suggestion, was a consideration of field experiments that could be done at Yucca Mountain to characterize some of its key features within a short period of time. This has led to a proposed work statement to DOE on the

characterization of the hydrologic properties of fault zones and fractured rock.

Two important features of this project should be pointed out here. First, this project is multidisciplinary, involving LBL staff with expertise in a broad range of earth science disciplines. As seen from the list of LBL personnel below all major geoscience disciplines are represented. This group of scientists has many years of combined experience in the nuclear waste geologic isolation problem. Many times, the major issues and results presented to DOE have undergone multidisciplinary discussions and the scrutiny by the whole LBL team.

Name	Principal Expertise
Chalon L. Carnahan	Geochemistry
Steven Flexser	Geology
Harold A. Wollenberg	Geology
Neville G. W. Cook	Geomechanics
John Kemeny	Geomechanics
Larry R. Myer	Geomechanics
Ernest L. Majer	Geophysics
Thomas V. McEvilly	Geophysics
H. Frank Morrison	Geophysics
Iraj Javandel	Hydrogeology
Marcelo J. Lippmann	Hydrogeology
Chin-Fu Tsang	Hydrogeology

Second, both parts of the project, the technical assistance and the topical studies, are largely performed by the same personnel (with additional LBL staff participating in some of the topical studies). This ensures the participation of highly respected

- 3 -

researchers working at the forefront of the state-of-the-art in providing DOE with comments and results relevant to the geotechnical aspects of nuclear waste geologic repositories. Often, technical reviews influence the direction and emphasis of topical studies, and topical studies provide inputs to the reviews.

The present report lists the technical reviews and comments made during the fiscal year 1988 and summarizes the technical progress of the topical studies.

In the area of technical assistance, there were numerous activities detailed in the next section. These included 24 geotechnical support activities, including reviews of 6 Study Plans (SP) and participation in 6 SP Review Workshops, review of one whole document Site Characterization Plan (SCP) and participation in the Assembled Document SCP Review Workshops by 6 LBL reviewers; the hosting of a DOE program review, the rewriting of the project statement of work, 2 trips to technical and planning meetings; preparation of proposed work statements for two new topics for DOE, and 5 instances of technical assistance to DOE. These activities are described in a Table in the following section entitled "Geoscience Technical Support for Nuclear Waste Geologic Repositories."

At DOE's suggestion, LBL considered what field experiments could be done at Yucca Mountain to characterize some of its key features within a short time (approximately one year). This suggestion prompted several multidisciplinary in-house discussions and led to a proposed work statement to DOE entitled "Hydrologic Properties of Fault Zones and Fractured Rock, and Evidence for Shallow Groundwater at Yucca Mountain, NV". It addresses Performance Issues 1.1 and 1.6 by seeking to determine if the fault zones are potential conduits for ingress of fluids to the candidate horizon or for movement of fluids away from the horizon. These studies would be complementary to the exploratory shaft investigations and the results would help plan those investigations. This is attached as an Appendix of this report.

The subject of fracture studies forms the main part of the topical studies. The problem was approached from many directions:

Solid Mechanics,

Fluid Dynamics,

Geology,

Geophysics, and

Geochemistry.

The progress of our fracture studies is described in this report, with the article titles and authors listed in the Table of Contents. This multidisciplinary program included laboratory experiments and theoretical analyses as well as numerical simulations. Some of the studies are of a fundamental nature, which we expect will provide the basis for important practical geotechnical issues to be addressed, clarified or resolved in the next one or two years. Other studies have already yielded results that provide new insights and analysis techniques for understanding the physics and chemistry of fractured repository rock systems at Yucca Mountain. A complete publication list of 27 reports from this project is presented at the end of this report.

The major accomplishments of the past year of this project may be summarized as follows:

- Scanning electron microscope examinations of microcracks in core at different distances from an in-situ heater (simulating radioactive waste) are being compared with the relationships between the rocks mechanical and geochemical properties and proximity to the heater (page 17).

- Evidence for mobility of uranium decay series elements was observed in core of tuff from an active hydrothermal system (page 17).

- Pre-heater baseline mechanical and geochemical properties of core of welded tuff from a heater test in "G" tunnel at NTS are being determined, and will be compared with properties of post-heater-test drillback core (page 17).

- Laboratory studies were carried out to evaluate the effects of multiple fractures on seismic wave velocity and attenuation. Using idealized fractures, experimental results were in accordance with predictions of a new model representing fractures as displacement discontinuities. The effect of multiple fractures is independent of spacing between the fractures until it is on the order of 1/10 wavelength of the propagation wave and on the order of the spacing between contacting asperities within each fracture (page 32).

- A new approach to modeling the mechanical deformation of fractures was developed. Using energy-minimization methods, interaction between asperities, as well as deformation of the asperities themselves, is taken into account. The approach has led to the identification of a roughness coefficient which may be useful for quantitatively relating easily measured geometrical characteristics of fractures to their mechanical properties (page 32).

- A detailed analysis is carried out on a 2D single fracture with variable apertures and the flow through channels is demonstrated. The channels defined this way are not rigidly set pathways for tracer transport, but are the preferred flow paths in the sense of stream-tubes in the potential theory. It is shown that such variable-aperture channels can be characterized by an aperture probability distribution function, and not by the exact deterministic geometric locations. We also demonstrate that the 2D tracer transport in a fracture can be calculated by a model of a system of 1D channels characterized by this distribution function only. Due to the channeling character of tracer transport in fractured rock, random point measurements of tracer breakthrough curves may give results with a wide spread

in value due to statistical fluctuations, and it is suggested that such a wide spread can probably be greatly reduced by making line/areal (or multiple) measurements covering a few spatial correlation lengths (page 81).

- A new analytic solution has been developed that can determine the overall transmissivity of a fault or other potentially conductive features under saturated conditions (page 105).

- Coupling of precipitation/dissolution reactions to diffusive transport via porosity changes has been implemented in the computer program THCC, a simulator of reactive chemical transport. The coupling is accomplished without increasing the set of primary unknowns. Porosity is included explicitly in the transport equations and is tracked by accounting for changes of volumes of precipitates. The coupling prevents the volume of a precipitated solid from exceeding available pore volume. Results of calculations are presented for two examples, each done with and without variable porosity (page 115).

- Work continued on the development and application of the Beam87 code and the development of a 3-D code ANRAY. These will be used to model seismic studies at Yucca Mountain (page 124).

- A model for the mechanics of normal faulting in the Basin and Range is developed, and applied to faulting within the Yucca Mountain site area. In this model, the propagation of slip along a single, planar, normal fault is explicitly considered. The propagation of slip can initiate either from an aseismically deforming detachment fault, or from aseismic slip below the brittle-ductile transition. The model calculates seismic source parameters associated with slip along normal faults, such as earthquake magnitude, energy release, and regional stress changes. By varying the parameters in the model, bounds on the seismic hazard

associated with faulting at Yucca Mountain can be estimated. Also, from the regional stress changes, fluctuations in water level can be estimated (page 136).

Geoscience Technical Support
for Nuclear Waste Geologic Repositories

D. C. Mangold and C. F. Tsang

The Geoscience Technical Support activities in the Geologic Repository Project (GRP) at LBL covered a broad range of reports and reviews in FY88, particularly reviews of Study Plans (SP) of the Yucca Mountain site and their associated Comment Resolution Workshops. It also included the rewriting of the Statement of Work for the project after Congress passed legislation in December 1987 selecting Yucca Mountain as the only site for further site characterization activity. Furthermore, topical reports and plans for selected new work have been prepared, based on requests from DOE/HQ. The accompanying table, "Geotechnical Support Activities: Fiscal Year 1987," gives the type of technical review or other activities, the date when a report was sent to DOE, and a brief description of the material reviewed or meeting attended.

The reviews were performed by a pool of highly knowledgeable and respected research scientists, who represent a broad range of disciplines in the earth sciences. The individuals and their specialities are listed in the table below. The diversity of backgrounds of the participating scientists is representative of the multidisciplinary teamwork that has characterized LBL's effort in this project. They have developed a close working relationship through frequent internal LBL discussion meetings and through cooperative topical studies (reported in subsequent parts of this report) and based on this, they are able to perform the many different technical support tasks given by DOE in a timely and effective manner.

Name	*Principal Expertise*
Chalon L. Carnahan	Geochemistry
Steven Flexser	Geology
Harold A. Wollenberg	Geology
Neville G. W. Cook	Geomechanics
John Kemeny	Geomechanics
Larry R. Myer	Geomechanics
Ernest L. Majer	Geophysics
Thomas V. McEvilly	Geophysics
H. Frank Morrison	Geophysics
Iraj Javandel	Hydrogeology
Marcelo J. Lippmann	Hydrogeology
Chin-Fu Tsang	Hydrogeology

In total, there were 24 geotechnical support activities, including reviews of 6 Study Plans (SP) and participation in 6 SP Review Workshops; review of one whole document Site Characterization Plan (SCP) and participation in the Assembled Document SCP Review Workshops by 6 LBL reviewers; the hosting of a DOE program review, and the rewriting of the project statement of work; writing a proposed work statement at DOE's suggestion; 2 trips for technical and planning purposes; and 5 instances of technical assistance to DOE. Each activity is described in the accompanying table at the end of this section. A brief summary of the activities for each of the categories is given below.

Study Plan Reviews

The Study Plans of the NNWSI (Nevada Nuclear Waste Storage Investigations Project) site were reviewed by LBL scientists in the areas of geology, geomechanics, geophysics, hydrology, and geochemistry. In general, reviews were done by a few specialists in each area in order to cover the technical aspects in each Study Plan. The comments on the technical aspects of these Study Plans were also provided to DOE in a timely way.

Those who performed the technical review were also participants in the rest of the review process. They held overall review discussions at LBL on the Study Plans to achieve a multidisciplinary overview and understanding of each one. After these discussions, many of the same scientists who reviewed a given chapter or section of a Study Plan also attended the SP Comment Resolution Workshops where all comments on that portion were considered. There they worked with the authors and DOE review leaders to suggest changes or revisions to improve the technical content of the text, particularly by helping to clarify technical points in the documents. Also, they later dealt with the dispositions of their comments by others so that a well-balanced review would be achieved.

Site Characterization Plan Reviews

Prior to the change in direction of DOE/OCRWM in December 1987, the chapters for the Site Characterization Plan Reviews of the SRP (Salt Repository Project) site were reviewed by LBL scientists during October and November in the areas of geology, geomechanics, geophysics, hydrology, geochemistry, the repository, and the site study programs in these areas. A total of 9 LBL staff scientists reviewed 22 portions of the SRP SCP. In November, 6 LBL reviewers attended the Assembled Document Review Workshops in Washington, DC for one to two weeks, working with DOE and the SRP authors to improve the technical content and presentation in the SCP.

DOE Program Review and Rewriting the Statement of Work

In July LBL hosted a program review of the GRP project (this project) at DOE's request. LBL scientists gave presentations of their research work at this program review on laboratory studies of fracture properties and behavior, fracture network modeling, multi-phase flow in fractured media, and geophysical detection of fractures. A copy of the viewgraphs from the presentations was sent to DOE.

The Statement of Work for the project was rewritten at DOE request after Congress passed legislation in December 1987 selecting Yucca Mountain as the only site for further site characterization activity. This was followed by a review by DOE and its suggested revisions being incorporated into the new Statement of Work.

Proposed Work Statement for Field Experiments at Yucca Mountain

At DOE's suggestion, LBL considered what field experiments could be done at Yucca Mountain to characterize some of its key features within a short time (approximately one year). This suggestion prompted several multidisciplinary in-house discussions and led to a proposed work statement to DOE entitled "Hydrologic Properties of Fault Zones and Fractured Rock, and Evidence for Shallow Groundwater at Yucca Mountain, NV". It addresses Performance Issues 1.1 and 1.6 by seeking to determine if the fault zones are potential conduits for ingress of fluids to the candidate horizon or for movement of fluids away from the horizon. These studies would be complementary to the exploratory shaft investigations and the results would help plan those investigations. The resulting report is attached as an Appendix, "Proposed Work Statement on the Hydrologic Properties of Fault Zones and Fractured Rock, and Evidence for Shallow Groundwater at Yucca Mountain, Nevada."

Trips

Besides trips to attend technical review meetings and Comment Resolution Workshops, two LBL investigators were invited to make a presentation of their GRP-sponsored research work to the Exploratory Shaft Test Plan Committee (ESTF) in Las Vegas, NV, in April. Afterward they visited G-tunnel and had further discussions with LLNL and other researchers on collaboration among them for studies in G-tunnel and plans for ESTF experiments.

A group of scientists from LBL visited the Yucca Mountain site in June to see first-hand the geological features, tour G-tunnel, and view the core processing facility.

Other Technical Assistance to DOE

In March, two reports of research from Task 2 of this project, Tracer Transport in Variably Saturated Media, were sent to DOE with executive summaries showing the importance of measuring fracture apertures in the field for tracer tests in order to measure the transport properties of a site. Two more reports were sent in July to show the progress in the findings of the research on this important topic. The purpose of these reports was to supply timely input to the preparation of Study Plans by the Yucca Mountain Project.

As mentioned above, there were discussions between LBL researchers in this project and those from LLNL and SNL and others concerning a possible collaboration among them on studies of heated fractured rock in the G-tunnel experiments that would have application to the ESTF experiments. These activities provide a means of direct input of this project to the Yucca Mountain Project.

At DOE request, a memorandum concerning Long Valley as a natural analog for investigations in tuff was sent to DOE/HQ in April, with 5 reports by LBL scientists (and other researchers) on Long Valley.

Conclusion

LBL tried to be responsive and active in meeting DOE's need for geoscience technical support for nuclear waste repositories. The ability of scientists from many disciplines to work together at LBL was an important part of the effort to provide DOE with timely, helpful, and balanced technical comments and topical reports to meet its on-going responsibilities.

GEOTECHNICAL SUPPORT ACTIVITIES

FISCAL YEAR 1988

Activity	Delivery	Description
SP Review	10/9/87	Study Plan 8.3.1.2.2.4, Characterization of Yucca Mountain Unsaturated Zone Percolation—ESF Study
SP Review Workshop	10/19–20/87	Comment Resolution Workshop for Study Plan 8.3.1.2.2.4, Characterization of Yucca Mountain Unsaturated Zone Percolation—ESF Study, held at DOE/HQ in Washington, DC
SP Review	10/22/87	Study Plan 8.3.1.2.2, Water Movement Tracer Test Using Chloride and Chlorine-36
SP Review	10/22/87	Study Plan 8.3.1.15.2.1, Characterization of Site Ambient Stress Conditions
Assembled Document Review	10/27–30/87 11/2–6/87	Review of the SRP SCP, 22 portions by 9 technical reviewers in the areas of Geology, Tectonics, Geoengineering, Postclosure Performance Assessment, Hydrology, and Geochemistry
SP Review Workshop	10/30/87	Comment Resolution Workshop for Study Plan 8.3.1.2.2, Water Movement Tracer Test Using Chloride and Chlorine-36 held at DOE/HQ in Washington, DC
SCP Review Workshops	11/9–13/87 11/16–19/87	Participation in the Assembled Document Review Workshops of the SRP SCP by 6 technical reviewers, held at DOE/HQ in Washington, DC
SP Review Workshop	12/3–4/87	Comment Resolution Workshop for Study Plan 8.3.1.15.2.1, Characterization of Site Ambient Stress Conditions held at DOE/HQ in Washington, DC
Statement of Work	1/4/88– 3/9/88	Rewrote Statement of Work for GRP Project at DOE request to reflect Congressional choice of the Yucca Mountain site, followed by a DOE review and its suggested revisions being incorporated into the new statement of work
Technical Assistance	3/24/88	Memorandum sent to DOE describing the discussions between LBL, LLNL, and SNL researchers on possible collaboration among them on studies of heated fractured rock in the G-tunnel experiments

GEOTECHNICAL SUPPORT ACTIVITIES

FISCAL YEAR 1988 (Continued)

Activity	Delivery	Description
Technical Assistance	3/29/88	Two reports produced in Task 2 were sent to DOE with executive summaries to show the importance of measuring fracture apertures in the field for tracer tests to measure the transport properties of a site
Trip Report & Technical Assistance	4/19/88	Memorandum sent to DOE describing the invited presentation by two GRP investigators to the Exploratory Shaft Test Plan Committee in Las Vegas, NV, their visit to G-tunnel afterward, and the further discussions between LBL, LLNL, and other researchers on collaboration among them for studies in the G-tunnel experiments and plans for ESTF experiments
Technical Assistance	4/20/88	A memorandum concerning Long Valley as a natural analog for investigations in tuff, and 5 reports by LBL staff (and other researchers) on Long Valley were sent to DOE
Proposed Work Statement	5/10/88	Proposed Work Statement on the Hydrologic Properties of Fault Zones and Fractured Rock, and Evidence for Shallow Groundwater at Yucca Mountain, NV, sent to DOE from LBL, an outgrowth of a suggestion made by DOE to LBL to consider field experiments which would examine key features of Yucca Mountain within a short time period
SP Review	6/8/88	Study Plan 8.3.1.15.1.3, Laboratory Determination of Mechanical Properties of Intact Rock
SP Review	6/16/88	Study Plan 8.3.1.3.2.1, Mineralogy, Petrology, and Chemistry along Transport Pathways
SP Review	6/20/88	Study Plan 8.3.1.2.3.1.7, Reactive Tracer Experiments in the C-Wells and Other Wells in the Yucca Mountain Vicinity
Trip	6/22–23/88	LBL staff scientists visited the Yucca Mountain site to saw the geological features, and had tours of G-tunnel and the core processing facility

GEOTECHNICAL SUPPORT ACTIVITIES

FISCAL YEAR 1988 (Continued)

Activity	Delivery	Description
SP Review Workshop	7/6–7/88	Comment Resolution Workshop for Study Plan 8.3.1.15.1.3, Laboratory Determination of Mechanical Properties of Intact Rock held at DOE/HQ in Washington, DC
Hosted DOE Program Review	7/7–8/88	At DOE's request, LBL hosted a two-day program review of the GRP project, and copies of the view-graphs of the presentations were sent to DOE at DOE's request
Technical Assistance	7/27/88	Two reports produced in Task 2 were sent to DOE, both of which were given as papers at the International Conference on Fluid Flow in Fractured Rocks, one being an invited paper
SP Review Workshop	8/4/88	Comment Resolution Workshop for Study Plan 8.3.1.3.2.1, Mineralogy, Petrology, and Chemistry along Transport Pathways held at DOE/HQ in Washington, DC
SP Review Workshop	9/1–2/88	Comment Resolution Workshop for Study Plan 8.3.1.2.3.1.7, Reactive Tracer Experiments in the C-Wells and Other Wells in the Yucca Mountain Vicinity held at DOE/HQ in Washington, DC with participation by 3 LBL staff scientists
Technical Assistance	9/9/88	A letter was sent to DOE concerning the water table anomaly near the proposed repository site, and its significance for further investigation

Geochemical and Geomechanical Investigations of Fractured, Heated Rock

H. Wollenberg, S. Flexser and L. Myer

Introduction

The local geochemical - hydrological regime will be affected by high temperatures in the near field of a nuclear waste canister. These hydro-geochemical processes must be understood if the transport of radionuclides away from a breached canister is to be modeled and predicted. The objective of our investigations is to develop an understanding of the interaction, under elevated temperatures, of radionuclides in the fluids with material lining the fractures, and to understand the mechanical response of the fractured rock to the elevated temperatures. To accomplish this, samples of core from holes that penetrate high-temperature zones are examined petrologically, geochemically, and geomechanically. During 1988, emphasis shifted from investigations of granitic rock to tuff. In this respect, a paper covering evidence of the mobility of uranium in open fractures in granitic rock was submitted for publication (Wollenberg and Flexser, 1988). Our examinations compare properties of rock in elevated temperature zones with those in zones of lower and near-ambient temperature. In this report we first describe detailed observations of microcracks in granitic rocks, and then cover distributions of radioelements in heated and unheated tuff.

Microcrack Investigations

The distribution and orientation of open and closed microcracks were investigated in core from the vicinity of the Stripa heater experiment. Samples were obtained from

two core intervals previously studied for their seismic velocity and attenuation characteristics (Wollenberg, et al., 1988). These samples, at 10.5 m and 11.1 m from the collar of the drillback hole, were located approximately 20 cm and 80 cm from the edge of the heater hole (Figure 1), where maximum temperatures reached about 325°C and 200°C, respectively, during the heater experiment. Compressional- and shear-wave amplitudes, and seismic quality factors (Q) were substantially lower in the sample nearer the heater, compared to the more distant sample.

Sections of the core were cut along planes both parallel and normal to the core axis. From these, petrographic thin sections (thickness 30 microns) were prepared, and their surfaces ion-milled for study in the scanning electron microscope (SEM). Care was taken during sectioning and thinning to minimize the possibility of induced fracturing or re-opening of previously sealed fractures.

Stripa core is composed of quartz monzonite characterized by a great abundance and variety of fractures, ranging from extremely fine, discontinuous intragranular and grain boundary cracks, to extensive fractures and breccia zones visible on a megascopic scale. The overwhelming proportion of the fractures on all scales are sealed, but a small number of open fractures are observed, generally on a submicroscopic scale. We have surveyed, by petrographic and electron microscopy, the various types of fractures present in the sections parallel and normal to the core axis; the orientations and distribution of open and closed fractures observed in the SEM are summarized in Figure 2.

In general, the most prominent fractures are sealed. This is seen clearly, for example, in the sections at 20 cm, where a fracture set intersecting these planes is indicated by the parallel diagonal lines. These continuous intergranular fractures are typically sealed with chlorite, quartz, and fine breccia. The remainder of the population of closed microcracks shown in Figure 2 are mainly confined within grains or along grain boundaries, and are filled with material mineralogically similar to the primary grains

(usually quartz and feldspar) which they intersect and border. A sampling of observed open microcracks is shown in the SEM photomicrographs in Figure 3, A-D. These illustrate typical intra- and inter-granular cracks, and the different characteristics resulting from differences in mineralogy and type of deformation.

The orientations of the open fractures thus far observed differ somewhat in the two pairs of core sections. At 20 cm, open cracks in the section parallel to the core axis (Figure 2A) are generally oriented at a high angle to the axis direction, and also to the surface of the section. Open cracks in the section normal to the core axis (generally near-horizontal in the orientation shown in Figure 2B) can be seen both in the SEM and the petrographic microscope to intersect the surface of this section at a low angle (a high angle to the core axis). In both sections at 20 cm, then, the directions of opening (perpendicular to the line of the fractures) appear to be subparallel to the core axis.

In the sections cut at 80 cm, there is a somewhat smaller population of open microcracks (as well as a lesser abundance of fractures generally). In contrast to observations at 20 cm, orientations of open cracks at 80 cm are not distinct from common orientations of closed cracks. In the plane normal to the core axis (B), open fracture orientations appear less consistent at 80 cm than at 20 cm, and there is no evidence of low-angle intersection with the surface as at 20 cm.

In summary, at this stage of the study it appears that a more consistent orientation of open microcracks occurs at 20 cm than at 80 cm from the heater hole. It is unclear whether this might be due to higher temperatures at the closer site, or to greater tensile fracturing there related to the changed stress regime caused by the heater cavity. The direction of microcrack openings at 20 cm, generally sub-parallel to the core axis, seems consistent with the latter interpretation.

Studies of Tuff

A. Hydrothermal System

Samples of core from hole RDO-8, drilled by the Department of Energy in rhyolite of the Long Valley (CA) caldera's hydrothermal system were examined for radioelement distributions. This hole, 2400 ft. deep, penetrates a thermal regime from near ambient temperature to over 200°C, primarily in moderately to strongly welded tuff (Wollenberg et al., 1987). Core samples covering the range 60 to 200°C were examined by gamma-ray spectrometry for their radioelement concentrations. Based on earlier examination of the natural gamma-ray log of the hole and the gamma spectral measurements, anomalous zones were identified where U is the predominant radioelement and there is disequilibrium in the U decay series. The distributions of radioelements in the tuff are shown in Figure 4 with asterisks indicating samples of special interest with regard to U and U-series disequilibrium. The anomalous U zone, associated with calcite-cemented breccia, is at a depth of 925 - 950 ft., where the temperature is ~ 150°C, a position in the tuff where calcite generally first appears. This is also a zone of rapidly increasing temperature with depth, where whole-rock oxygen-isotope ratios are concomitantly decreasing from approximately +3 to approximately -2. The detailed distribution of U in this zone was examined in a sample of calcite-cemented breccia by fission-track radiography. Uranium is concentrated in the range 20 to 70 ppm, and is associated with sulfide-mineral-rich zones in the breccia. The uranium concentration in the calcite not associated with sulfides is 11 to 13 ppm, and its "background" in unbrecciated tuff averages ~ 6 ppm. Thorium in the high-U zone is also somewhat elevated, ~ 24 ppm, compared to a local "background" of ~ 20 ppm, a considerably lower contrast than for U. The U/Th ratio in this zone, ~ 1, is anomalously high, compared to ~ 0.3 in the rest of the core. High-resolution gamma-spectrometry indicates that the U in the breccia zone is not in secular equilibrium with its daughter elements, suggesting recent mobilization/deposition of parent U and/or its

daughters in the hydrothermal environment. Thus there is evidence for mobility of U in an active hydrothermal system in tuff, at temperatures comparable to those expected in a repository environment.

B. Nevada Test Site

In April, 1988, discussions were held with personnel of LLNL and LANL regarding drilling-back into existing and planned heater holes at the G-tunnel test facility, to investigate properties of heated, welded tuff. The facility was visited to examine access for coring and the availability of core to begin mineralogical, geochemical, and geomechanical studies of tuff that has been subjected to temperatures comparable to those expected in a repository environment. Core was selected from a hole that passes within one meter of the position of an electric heater that will simulate the localized thermal field caused by the introduction of high-level waste (Figure 5). The hole, designated NE-2 by the LLNL experimenters, was drilled to slant downward beneath the central portion of the heater; its closest approach to the heater position is ~ 1 meter. Results of geochemical and geomechanical investigations of this core will serve as a baseline for comparison with those of core to be obtained by drilling through the heater location following the heater experiment.

Results of gamma-ray spectral measurements of the core are shown in Figure 6, and indicate a relatively uniform distribution in U concentration over the 22 ft. length of the hole. A somewhat greater variation in Th concentration is noted. The relatively high concentrations of U and Th at 17.5 ft., are associated with a core segment cut by a fracture partly coated with amorphous silica. Radioelement comparisons are shown in Table 1, and indicate a strong linear correlation of Th with K, while the correlations of U with K and Th are relatively weak. This apparently independent behavior of U will be investigated by more detailed gamma spectral measurements and fission-track radiography. Comparison of radioelement concentrations (Table 2) indicate that U and

Th are lower in the Grouse Canyon tuff than in the Topopah Spring tuff, while K concentrations are similar. Mineralogical and geochemical differences between the two units were noted by Connolly et al. (1983), who describe the Grouse Canyon tuff as marginally peralkaline, in contrast to the subalkaline nature of the Topopah Spring tuff. They state that the peralkalinity of the Grouse Canyon tuff permitted this relatively thin unit to become densely welded. Thus, its physical properties are probably more similar to those of thick devitrified portions of the Topopah Spring tuff than if the Grouse Canyon were of calc-alkaline composition.

Following the present heater test and removal of the heater, a hole will be cored through the heater hole at the midplane of the heater. Detailed mineralogical, geochemical, and geomechanical examinations will be made of this core and results compared with those of the NE-2 core for comparison of pre- and post-heating effects on the welded tuff. This will serve as a prototype investigation for those expected to be conducted in the exploratory shaft test facility, once it is excavated in the Topopah Springs tuff.

References

Connolly, J. R., Mansker, W. L., Hicks, R., Allen, C. C., Husler, J., Keil, K., and Lappin, A. R.; Petrology and geochemistry of the Grouse Canyon member of the Belted Range tuff, rock mechanics drift, G-tunnel, Nevada Test Site, Sandia National Laboratories rept. SAND81-1970, 1983.

Schuraytz, B. C., Vogel, T. A., and Younker, L. Y.; Geochemical gradients in the Topopah Spring member of the Paintbrush tuff: evidence for eruption across a magmatic interface, Lawrence Livermore National Laboratory rept. UCRL-53698, 1986.

Wollenberg, H. A., Sorey, M. L., Farrar, C. D., White, A. F., Flexser, S., and Bartel, L. C.; A core hole in the southwestern moat of the Long Valley caldera: early results, EOS 68, p. 529, 1987.

Wollenberg, H. A. and Flexser, S.; Evidence for mobility of uranium in fractured, heated rock, Lawrence Berkeley Laboratory Report LBL-26137, 1988 (submitted to Applied Geochemistry).

Wollenberg, H., Myer, L., Flexser, S., and Scheiner, J.; Geochemical and Geomechanical Investigations of fractured, heated rock; section in GRP project report (LBL-24758), 1988.

Zielinski, R. A., Bush, C. A., Spengler, R. W. and Szabo, B. J.; Rock-water interaction in ash-flow tuffs (Yucca Mountain, Nevada, U.S.A.)- the record from uranium studies, *Uranium*, 2, 361-386, 1986.

Table 1. Correlations Between Radioelement Concentrations

	r^2*
Th vs U	0.43
Th vs K	0.96
U vs K	0.28

* r^2 = coefficient of determination

Table 2. Radioelements in Grouse Canyon and Topopah Spring Tuffs

	U	Th	K	Th/U
Grouse Canyon tuff (NE-2 core)	3.4 ± 0.4	15.6 ± 2.1	3.9 ± 0.5	4.6 ± 0.5
Topopah Spring tuff[a]	4.5 ± 0.5	23.4 ± 2.1	4.0 ± 0.8	5.3 ± 0.5

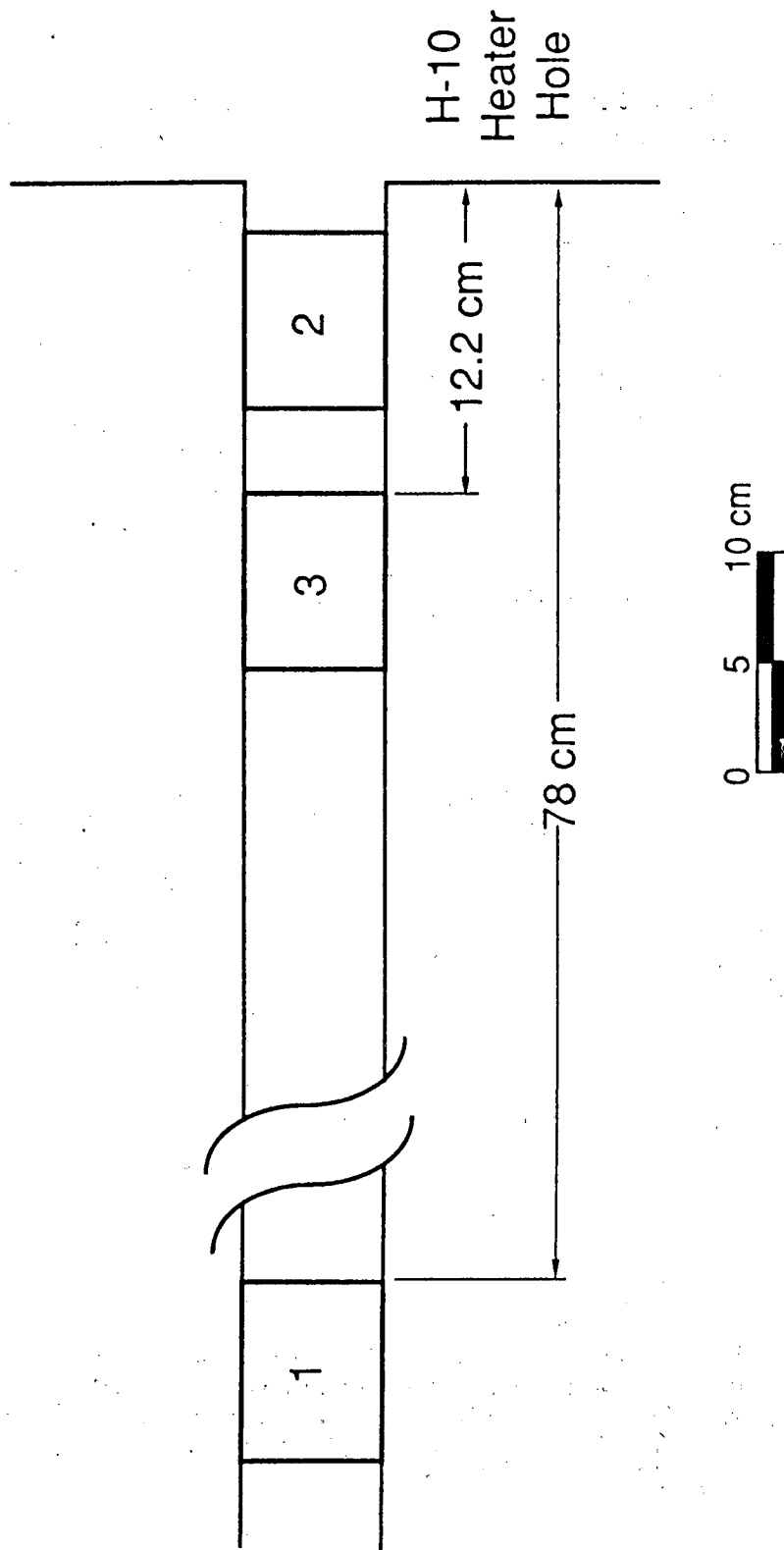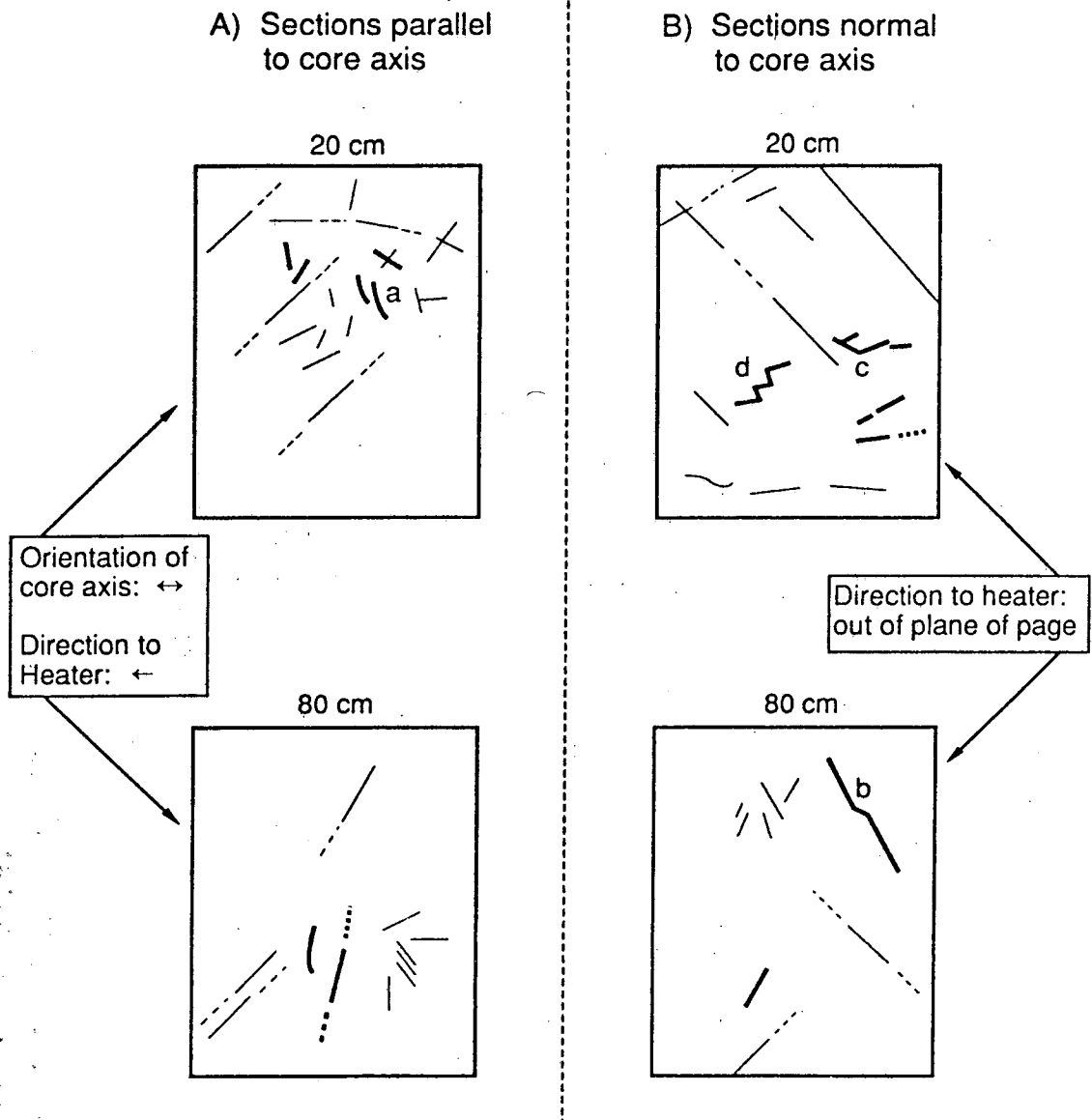[a] from Schuraytz et al. (1986) and Zielinski et al. (1986).

Figure 1.   Detail of locations of drillback core samples for seismic studies.   Micro-cracks were examined in samples 1 and 3.

XBL 8711-10452

A) Sections parallel
to core axis

B) Sections normal
to core axis

20 cm

20 cm

Orientation of
core axis: ↔

Direction to
Heater: ←

Direction to heater:
out of plane of page

80 cm

80 cm

XBL 8810-10497

Figure 2.   Schematic representation of the orientations and distribution of micro-
cracks intersecting planes parallel to (A) and normal to (B) the core axis,
as observed in the SEM. Bold lines indicate open fractures, thin lines
sealed and closed fractures. Locations (a) through (d) correspond to SEM
photographs shown in Figure 3.

Figure 3.   S.E.M. photomicrographs of representative open microcracks observed in the sections shown in Figure 2.
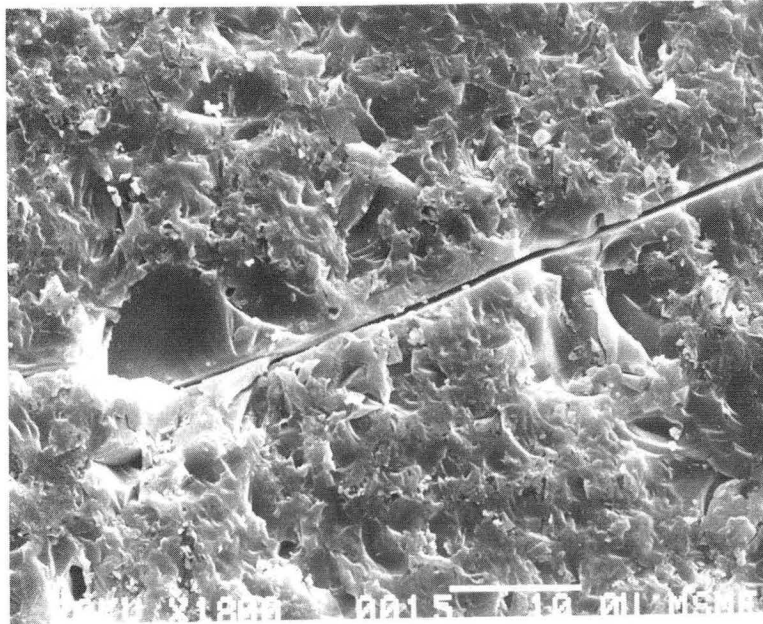

a)   Intra-granular crack cutting quartz grain at location (a), Fig. 2. Bar is 10 microns.
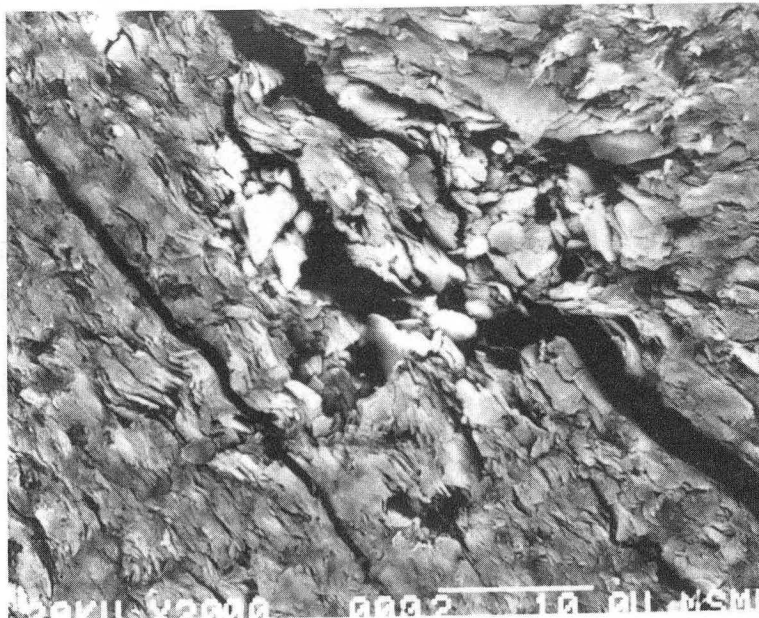
b)   Portion of longer inter-granular crack, with smaller offshoot, in chlorite at location (b), Fig. 2. Cleavage foliation of chlorite, visible in photograph, has caused slight change in direction of cracks. Bar is 10 microns.

Figure 3.   S.E.M. photomicrographs of representative open microcracks observed in
(Cont.)   the sections shown in Figure 2.
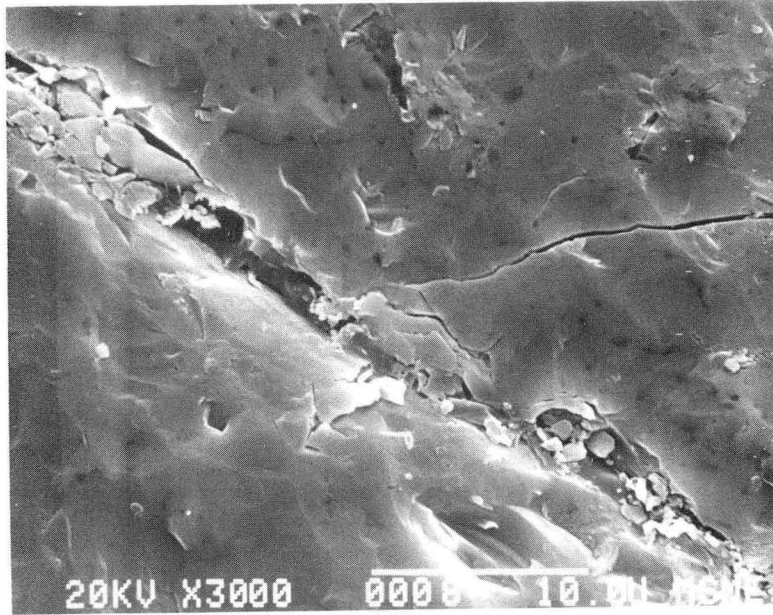
c)   Intra-granular cracks in quartz at location (c), Fig. 2. Larger crack shows
     shear deformation, while finer crack appears to have formed by simple pull-
     apart. Bar is 10 microns.
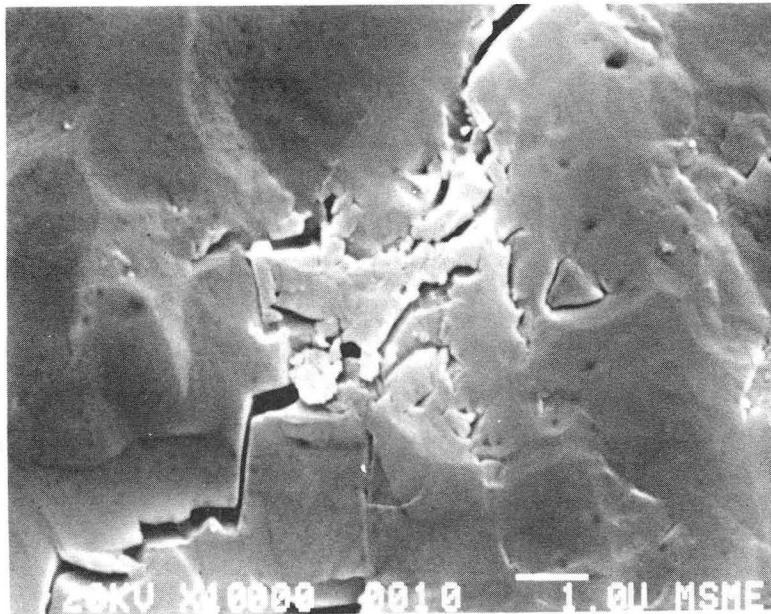
d)   Step-like crack formed by re-activation of sealed grain-boundary cracks
     between quartz grains at location (d), Fig. 2. Direction of displacement in
     this plane is indicated by relative offset of the steps. Bar is 1 micron.
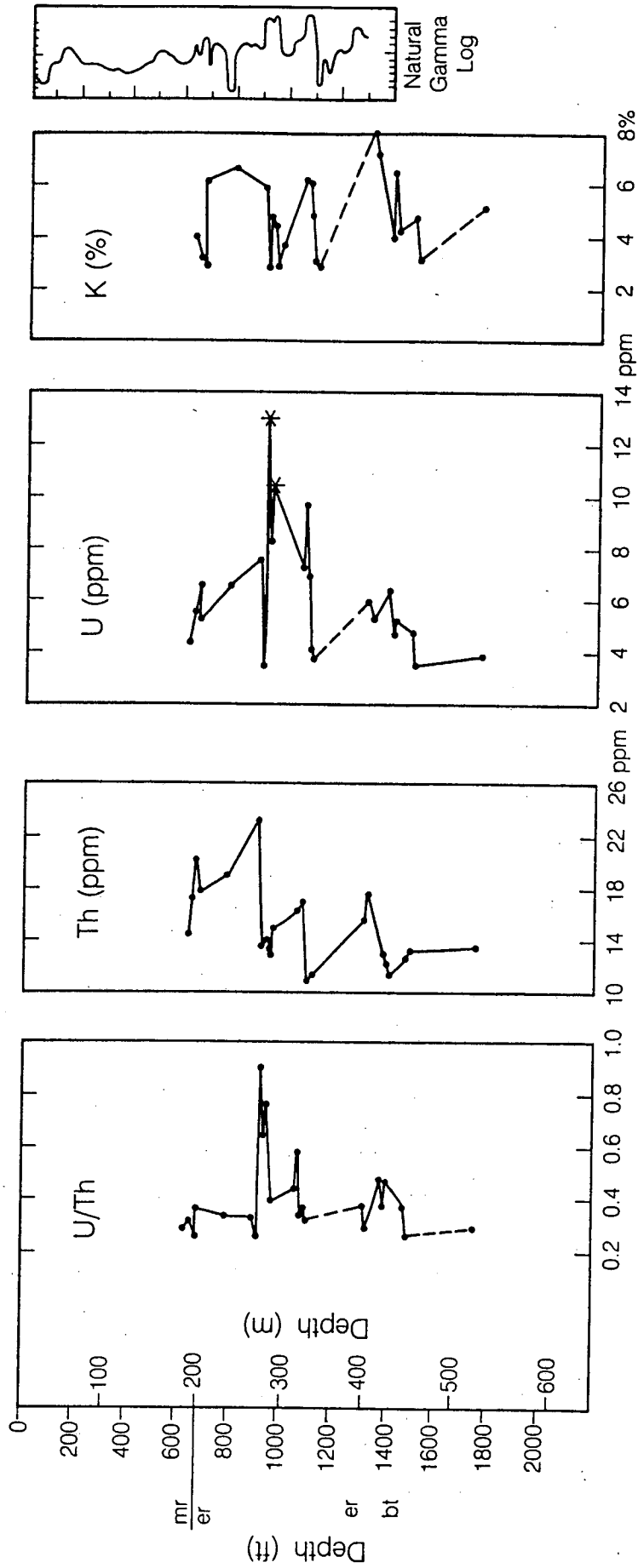
Figure 4. Distribution of radioelements over a temperature range 60°C (at top) to 200°C (at bottom) in tuff of the Long Valley caldera. Asterisks in the U diagram indicate samples where disequilibrium was observed in the U-decay series.

XBL 884-10220
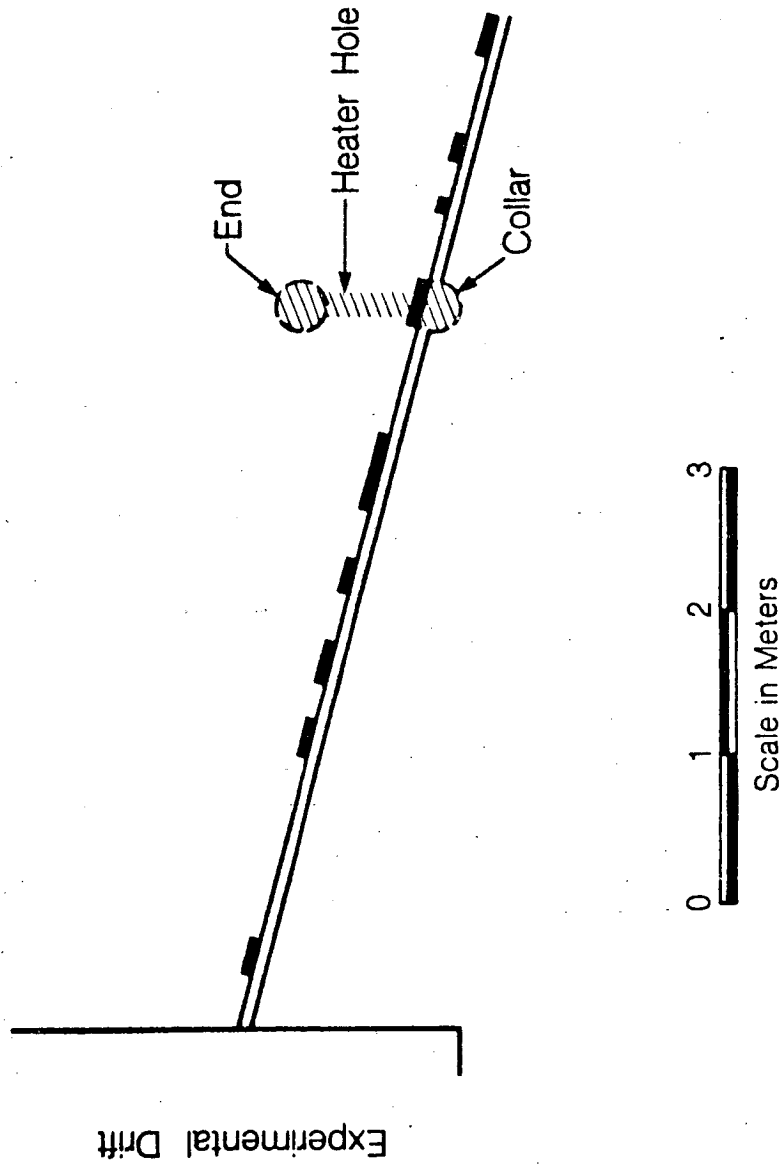
XBL 8810-10496

Figure 5.   Section perpendicular to the heater hole in NTS G-tunnel tuff, showing the NE-2 hole and its sampled intervals.
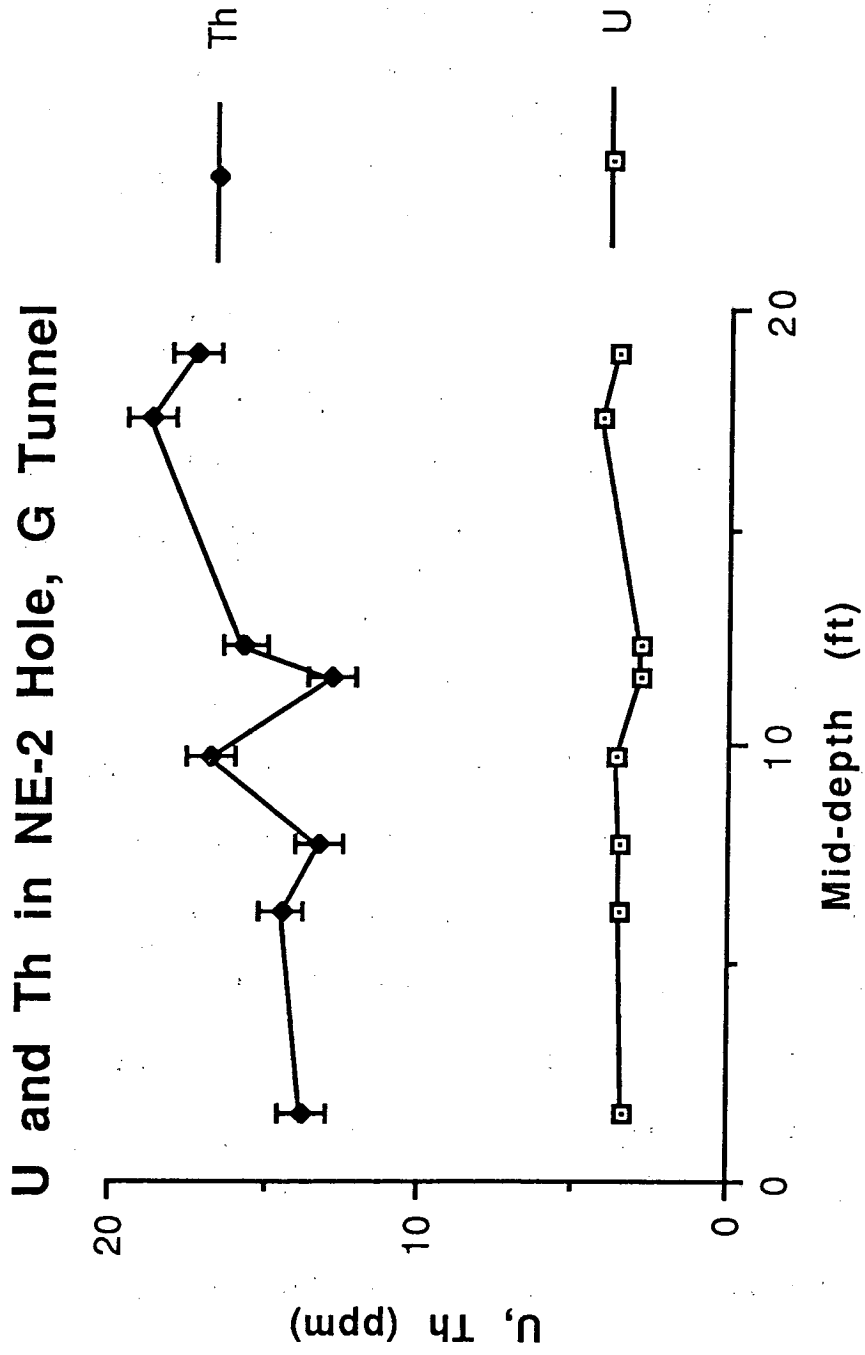
Figure 6. U and Th profiles of the NE-2 hole, NTS G-tunnel.

Seismic and Electrical Properties of Fractured Rock
Under Varying Degrees of Saturation

D. L. Hopkins, L. R. Myer, and N. G. W. Cook

It is well known that the mechanical and hydraulic properties of the Yucca Mountain site depend strongly on joints, fractures, and faults. For site characterization and performance confirmation, it is necessary to locate joints remotely and characterize them. Seismic and electrical geophysical techniques are promising methods for providing such information.

The state of stress in the rock mass will be changed by heat, by activities such as mining and drilling, and by natural tectonic events such as earthquakes, if they occur. These changes in stress can have a significant effect on radionuclide transport because they can result in opening of existing joints, creation of new fractures, and sliding along existing faults. These changes in the nature of the fracturing at the site might also be detected by geophysical techniques. The purpose of this task is to develop relationships between the changes in seismic and electrical signals and specific changes in the fractures.

In previous work, a series of laboratory experiments was performed to study seismic wave propagation across single fractures (Hopkins et al., 1986). Good agreement was found between the laboratory results and a seismic theory in which the velocity and amplitude of a seismic wave propagating across the fracture are related to the

mechanical stiffness of the fracture. However, to be of practical use in detecting and characterizing fractures in the field, the theory must be able to describe seismic wave propagation across multiple fractures. A new series of experiments has been performed to study how multiple fractures affect seismic wave amplitude and frequency content.

The need to calculate the stiffness of the idealized fractures created in the laboratory prompted the development of an analytical model of the deformation of a fracture under normal stress (Hopkins et al., 1986). The model was extended so that it could be used to study changes in fracture aperture as a function of stress (Hopkins et al., 1987). The model has now been reformulated to permit study of the effects of capillary and pore pressure and the relationship between surface roughness and fracture stiffness.

1. Seismic Studies

1.1 Seismic Theory

Only a brief summary of the seismic theory will be given here; for a full description see Hopkins et al., 1986. The seismic theory assumes that stresses are continuous across the fracture while displacements are discontinuous. The discontinuity in displacement results from void closure and is proportional to the specific stiffness of the fracture. It is further assumed that the thickness of the interface is small compared to the incident wavelength. Solution of the wave equation results in frequency dependent reflection and transmission coefficients for both compressional and shear waves.

A fracture can be thought of as two rough surfaces in partial contact. Specific stiffness has the desirable property of approaching zero for an interface with vanishing contact and becoming infinite for a perfectly welded fracture. As the contact area between the fracture surfaces vanishes, the fracture approaches a free surface and all seismic energy is reflected. As the fracture approaches a welded contact, all seismic energy is transmitted. Figure 1 shows the transmission coefficient for P-waves (compressional waves) as a function of frequency for different fracture stiffnesses. A coefficient of one means that all the seismic energy is transmitted across the fracture. The figure shows that the transmission coefficient increases with increasing stiffness for all frequencies.

Because Yucca Mountain is partially saturated, it is important to know how varying degrees of saturation affect seismic wave propagation and fracture deformation. Mechanically, the presence of a liquid results in an internal pressure being generated in the fracture. Liquid presence is not expected to have a significant effect on the stiffness until the fracture is almost fully saturated. At that point, the fluid in the void spaces exerts a reactive force on the fracture surfaces resulting in an increase in the stiffness of the fracture. However, it is likely that seismic wave propagation will be affected by pore fluid well before the fracture is fully saturated. Under unsaturated conditions, the wave amplitudes will be reduced due to energy dissipation by motion in the liquid. Models incorporating this attenuation mechanism have been investigated by Mavko and Nur (1979) and Hudson (1988).

1.2 Seismic Experiments

Experimental work was begun with a series of laboratory experiments designed to study seismic wave propagation across a single fracture using an idealized model in which the fracture is created by placing thin lead strips between steel cylinders. Steel, rather than rock, was used so that the fracture properties could be controlled precisely. Since fracture stiffnesses can be calculated exactly for the idealized fractures, the tests provide a means of validating the theoretical model.

The current series of laboratory experiments was designed with two goals in mind. The first objective was to study the effect of multiple fractures on the frequency content and attenuation of seismic waves. The second objective was to study the degree to which seismic methods can discriminate between fractures. For the current series of experiments, two parallel fractures are created by placing thin lead strips between steel cylinders (see Figure 2). Piezoelectric crystals are used to generate and receive P- or S-waves. For the results presented here, the two fracture stiffnesses were equal to each other. The distance between the two parallel fractures was varied from a minimum value that corresponded to one-tenth of the seismic wavelength to a maximum value of about 1.4 times the wavelength (see Figure 3).

For P-waves, the presence of the fractures results in a delay and widening of the seismic pulse, and a reduction in amplitude (Figure 4). The seismic signal propagated across the two fractures was nearly identical in amplitude and frequency content for all spacings except for the closest, equal to one-tenth the wavelength of the seismic wave. For this close spacing, there was an increase in the signal amplitude (Figure 5). The same series of experiments was performed using S-waves and the results were identical: the amplitude and frequency content of the received signals were the same for all

spacings, except the closest spacing, in which case there was an increase in the signal amplitude (Figure 6).

One explanation for this increase in amplitude is that at close spacings the fractures are interacting mechanically, so the seismic wave "sees" a single interface rather than two distinct fractures. Thus, for spacings on the order of one-tenth of the wavelength of the seismic pulse, the seismic wave is unable to discriminate between two fractures and a single fracture. The result of the mechanical interaction is an effective stiffness which is greater than the combined stiffnesses of the two fractures more widely spaced. Parallel fractures can be regarded as independent until the spacing between them becomes small compared to the seismic wavelength.

For both the P- and S-waves, the waves propagated across the two fractures are significantly reduced in amplitude, delayed in time, and have a different frequency content than waves propagated through solid steel. This result shows that despite the small thickness of the fractures in relation to the seismic wavelength, they significantly affect seismic wave propagation.

Both laboratory and analytical studies of closely spaced fractures are planned for the current year. In the laboratory, additional multi-fracture experiments will be performed. The stiffness of the fractures will be varied to see if the results obtained thus far are, in general, consistent with theoretical predictions. In addition, the effect of closely spaced fractures will be studied. Single fracture experiments will be done in parallel with the multi-layer experiments to see if it is possible to model the effect of two closely spaced fractures with a single fracture. The stiffness of the single fracture will be varied and the transmitted signal will be compared with that obtained for the

two closely spaced fractures.

In conjunction with the laboratory experiments, analytic work will be done to determine when parallel fractures interact mechanically. This will be studied in two ways. In the first, the numerical model described in the following section will be used to calculate the displacement profiles for two fractures for various applied stresses. It will then be possible to determine, as a function of applied stress, at what spacings the displacement profiles overlap. The second method will be to compare stress intensity factor solutions for a single crack to those for parallel cracks. The spacing between fractures will be varied in the parallel crack solution to determine at what point the solution is equivalent to that obtained by applying the solution for a single crack to both fractures independently. The results obtained will be compared to the laboratory results. Results will be used to evaluate the spacing (relative to wavelength) at which two fractures can be regarded as independent, and, when they do interact, the single fracture stiffness which has to be used to correctly predict the transmission of the seismic wave across the two closely spaced fractures.

2. Fracture Deformation Model

An analytical model describing the deformation of a fracture subjected to a normal stress has been developed and described in previous reports (see Hopkins et al., 1986 and 1987). The model was originally developed to calculate the stiffnesses of the idealized fractures created in the laboratory for the seismic experiments. However, due to its applicability to fluid flow problems, the model was extended to permit more general study of fracture stiffness and changes in fracture aperture as functions of

stress.

A fracture can be envisioned as two rough surfaces in partial contact. The fracture surfaces are represented by parallel planes separated by variable height asperities. In reality, a fracture will not likely lie completely within a single plane. However, because linear elasticity is assumed, the fracture can be modeled as described above and the calculated displacements can be superposed on the actual topography to obtain the true deformation of the fracture.

As described in previous reports (see Hopkins et al., 1987) the model presented here differs from asperity models used by other researchers in that it accounts for the deformation of the half-spaces defining the fracture and mechanical interaction between asperities. The deformation at any point on the half-spaces is assumed to be a linear combination of the displacements caused by the forces acting on all asperities in the region. Though more realistic than other approaches, complications are introduced by including half-space deformation and interaction in the model. These complications can be seen by examining three different formulations with increasing degrees of complexity: (I) asperities between incompressible half-spaces; (II) asperities between compressible half-spaces; (III) asperities between compressible half-spaces with interaction.

For all three cases, either the total applied force or the average displacement across the fracture is specified as a boundary condition. Given the boundary condition, the problem is then to determine how the force is distributed among the asperities. It is assumed that the average stress is continuous across the fracture. Since free surfaces are stress-free, the applied force is transmitted across the fracture through the points of contact. Once the force distribution is known, the displacement anywhere

along the fracture can be calculated. The stiffness of the fracture can then be computed as can the aperture at any point.

There are two possible approaches to finding the distribution of force across the fracture depending on how the boundary conditions are specified. In the absence of body forces, these two methods are (Sokolnikoff, p. 73):

1. Determine the equilibrium distribution of stresses and the compatible displacements in the interior of an elastic body given the distribution of the forces acting on the surface of the body.

2. Determine the equilibrium distribution of stresses and the compatible displacements in the interior of an elastic body given the prescribed displacements at the surface of the body.

For each of the three cases stated above, a solution technique is outlined for each of the two boundary conditions.

Case I: asperities between incompressible half-spaces

As previously stated, a fracture can be modeled as two parallel half-spaces separated by asperities of varying height. In all cases, the asperities are modeled as springs with equal diameter and spring constant. It is assumed that the spatial location and heights of the asperities are known. The problem is to determine how a force applied across the fracture is distributed among the asperities. As a first step, assume that the asperities do not interact and that the parallel planes defining the fracture do not deform. Thus, when a force is applied, the fracture planes remain parallel and flat and come together by an amount that depends on the compression of the asperities.

If the problem is formulated with a specified constant displacement boundary condition, then the amount by which the fracture planes come together is known. If the

fracture planes are separated by a distance d in the new equilibrium position, then all asperities with height greater than d are in contact. Hooke's Law for a linear elastic material is:

$$\sigma = E\varepsilon$$

where E is Young's modulus and ε is the strain due to the stress σ. For the case of an asperity modeled as a cylinder, Hooke's Law becomes

$$\left[\sigma = \frac{f}{A}\right] = E\left[\varepsilon = \frac{\Delta h}{h}\right] \quad or,$$

$$f_i = EA\frac{\Delta h_i}{h_i} \tag{2.1}$$

where Δh_i is the compression of the asperity due to force f_i, h_i is the height and A is the cross-sectional area of the i th asperity. Equation 2.1 generates n equations in the n unknown forces where n is the number of asperities in contact at the specified displacement. Assuming the equations are independent, the system of equations can be solved using standard methods.

If instead, the problem is formulated with a specified constant stress boundary condition, then the total force applied to the surface of the body containing the fracture is known. Assuming that stress is continuous across the fracture, this gives

$$F = \sum_{i=1}^{n} f_i \tag{2.2}$$

where F is the total force, f_i is the force carried by the i th asperity, and n is the total number of asperities in contact. In other words, for a constant stress boundary condition, we have an equilibrium constraint on the forces. The problem is more difficult to solve in this case because no information is provided about which asperities are in contact. Equation 2.1 still holds, but the Δh_i are unknown and it is not possible to

solve the system of equations directly to determine the individual forces f_i. However, it is possible to employ an iterative solution technique.

Let d be the separation of the fracture planes at the new equilibrium position. For asperities in contact, the compression of the ith asperity is

$$\Delta h_i = h_i - d$$

where h_i is the height of the asperity. Equation 2.1 can be rewritten as:

$$f_i = EA \frac{(h_i - d)}{h_i} \quad . \tag{2.3}$$

Since d is unknown, this represents a system of n equations in $n+1$ unknowns. However, we have the additional equation due to the equilibrium constraint on the forces (Equation 2.2) resulting in a system of $n+1$ equations in $n+1$ unknowns. Assuming the equations are independent, this would be a system that could be solved directly except that the number of asperities in contact (n) is unknown.

To solve the problem iteratively, a starting position is arbitrarily chosen; i.e. a value d' is chosen as the initial distance between the fracture surfaces after some force has been applied. Once d' has been specified, the number of asperities in contact with the fracture surfaces at this position is known and the resulting $n'+1$ equations can be solved to yield the forces f_i' that would be necessary to close the fracture the specified amount. The total force needed to reach the position d' is just the sum of the f_i'. This total force F' can then be compared with F, the total force actually applied. Assuming that F' is less than F, then the fracture surfaces are actually closer than d'. The value of d' can now be decreased until the next tallest asperity comes into contact at position d''. In the range between d' and d'', there is a linear relationship between force and displacement so that the total force for any value of the separation d is

easily computed. If the known total force F has not been reached by the time the next asperity comes into contact, the new set of $n'+2$ equations is solved to determine the new distribution of forces. The procedure continues until a separation and force distribution are reached which yields a total force equal to that applied.

2.2 Case II: asperities between compressible half-spaces

The problem becomes somewhat more complicated when the half-spaces defining the fracture are allowed to deform. When an asperity is in contact with both fracture surfaces, it exerts forces on those surfaces that causes them to deform (see Figure 7). In this case, the amount that the fracture closes depends on the compression of the asperities and the amount of deformation of the half-spaces.

Modeling the asperities as cylinders, the deformation of the half-spaces defining the fracture can be obtained from the Boussinesq solution for displacement below a uniformly loaded circle assuming a constant stress across the cylinder. For points inside the loaded area, the displacement in the direction of the force is (Timoshenko, 1970, p. 404):

$$w_i = \frac{4(1-v^2)qa}{\pi E} \left[\int_0^{\pi/2} \sqrt{1-(r^2/a^2)\sin^2\theta} \; d\theta \right] \qquad (2.4)$$

where: $E = Young's \; modulus$

$v = Poisson's \; ratio$

$a = the \; radius \; of \; the \; asperity$

$r = the \; distance \; from \; the \; center \; of \; the \; asperity$

$q = \dfrac{f_i}{a} = the \; stress \; on \; the \; asperity.$

To get the total displacement of the fracture surface beneath an asperity Equation 2.4

is integrated over the area of the asperity. Let d_{ii} be the total displacement of the half-space below the i th asperity due to the force (f_i) on that asperity:

$$d_{ii} = \int_0^{2\pi} \int_0^a w_i \, dr \, d\theta \quad . \tag{2.5}$$

where w_i is as defined in Equation 2.4 and a is the radius of the asperity. The average displacement of the half-space beneath the asperity, $\overline{d}_{ii}$, is just the total displacement divided by the area of the asperity:

$$\overline{d}_{ii} = \frac{d_{ii}}{\pi a^2} \quad .$$

Thus, the average displacement at the asperity in the normal direction is,

$$\overline{d}_i = \Delta h_i + 2\overline{d}_{ii} \tag{2.6}$$

where Δh_i is the compression of the asperity, $\overline{d}_{ii}$ is the deformation of the half-space and the two is to account for both fracture surfaces; i.e. the asperity will indent both the upper and lower half-spaces. The compression of the asperity, Δh_i, depends on the force f_i as given in Equation 2.1 and $\overline{d}_{ii}$ is a function of f_i through q, the stress on the asperity (see Equation 2.4). Define w' such that the displacement at a point inside the loaded area is:

$$w_i = f_i w' \quad .$$

Equation 2.5 can be rewritten as:

$$d_{ii} = f_i \int_0^{2\pi} \int_0^a w' \, dr \, d\theta$$

since the force is assumed constant across the cylinder. As above, the average displacement of the half-space is the total displacement divided by the area of the asperity: becomes

$$\overline{d}_{ii} = \frac{d_{ii}}{\pi a^2} = \frac{f_i \int_0^{2\pi} \int_0^a w' \, dr \, d\theta}{\pi a^2} \quad . \tag{2.7}$$

The compression of the asperity (Δh_i) can be expressed as a function of the force (f_i) by rewriting Equation 2.1:

$$\Delta h_i = \frac{f_i h_i}{EA}$$

where E is Young's modulus and A is the cross-sectional area of the asperity. Substituting this into Equation 2.6 along with the expression for d_{ii} obtained from Equation 2.7, the average displacement at the asperity in the normal direction can be rewritten as

$$\overline{d}_i = \frac{f_i h_i}{EA} + 2 \cdot \frac{f_i \int\limits_0^{2\pi} \int\limits_0^a w' \, dr \, d\theta}{\pi a^2} \quad .$$

Solving for the force f_i yields:

$$f_i = \frac{\overline{d}_i}{h_i/[EA] + [2 \cdot \int\limits_0^{2\pi} \int\limits_0^a w']/[\pi a^2]} \tag{2.8}$$

where $w' = w_i / f_i$ and w_i is as given by Equation 2.4. Equation 2.8 specifies the relationship between force and displacement for a single asperity when interaction between asperities is neglected. The problem of determining the distribution of forces across the asperities can now be solved in exactly the same way as described previously for the simpler problem of asperities between infinitely stiff half-spaces for either a constant stress or constant displacement boundary condition. For a constant displacement boundary condition, the number of asperities in contact is known as are the average displacements at the asperities in contact, the $\overline{d}_i$. The system of equations obtained from Equation 2.8 is solved for the unknown forces. For a constant stress boundary condition, the forces are found using Equation 2.8 and the iterative technique described

in the previous section.

2.3 Case III: asperities between compressible half-spaces with interaction

The next level of complexity is to account for the mechanical interaction between the asperities. The displacement at asperity i now has three components: the displacement due to the deformation of the fracture surfaces due to the force on the asperity itself; the displacement due to the compression of the asperity; and the displacement due to the deformation of the fracture surfaces caused by the forces on all neighboring asperities. In this case, it is important to note that an asperity in contact will deform the fracture surfaces over a region larger than the dimension of the asperity itself.

This mechanical interaction can be illustrated with a simple example. Consider fracture surfaces separated by two asperities of different height. For reference, define an initial position to be such that the tall asperity is just barely in contact. Let a_0 be the difference in height between the two asperities; i.e. a_0 is the gap between the short asperity and the fracture surface at the initial position (see Figure 8). If the two asperities are far enough apart so that the mechanical interaction between them is negligible, then the short asperity will come into contact when the average displacement across the fracture is greater than or equal to a_0 (Figure 8a). If, however, the two asperities are next to each other, then there will be displacement below the short asperity due to the force on the tall asperity and the displacement across the fracture will have to be greater than a_0 before the short asperity will come into contact (Figure 8b). Specifying the relationship between force and displacement is much more complicated in this case because the force at asperity i depends on the forces on all neighboring asperities.

For a single asperity, the displacement of the half-space outside the area of contact is also obtained from the Boussinesq solution for displacement below a uniformly loaded circle. For points outside the loaded area, the displacement in the direction of the force is (Timoshenko, p. 404):

$$w_o = \frac{4(1-v^2)qr}{\pi E} \left[\int_0^{\pi/2} \sqrt{1-(a^2/r^2)\sin^2\theta} \, d\theta - \left(1-\frac{a^2}{r^2}\right) \int_0^{\pi/2} \frac{d\theta}{\sqrt{1-(a^2/r^2)\sin^2\theta}} \right] \quad (2.9)$$

$where$: E = $Young's\ modulus$

v = $Poisson's\ ratio$

a = $the\ radius\ of\ the\ asperity$

r = $the\ distance\ from\ the\ center\ of\ the\ asperity$

$q = \frac{f_j}{a}$ = $the\ stress\ on\ the\ asperity.$

As discussed previously, the average displacement across the fracture depends on the deformation of the half-spaces above and below the asperities and their compression. The total displacement of the fracture surface beneath asperity i due to the force at asperity j is found by integrating the expression in Equation 2.9 over the area of the i th asperity:

$$d_{ij} = \int\int w_o \, dR \, d\theta \quad (2.10)$$

where the integration is over the area of the i th asperity. The average displacement of the half-space beneath asperity i due to the force at asperity j is the total displacement divided by the area of the i th asperity:

$$\bar{d}_{ij} = \frac{d_{ij}}{\pi a^2}$$

The displacements at asperity i are now specified. As before, the compression of the asperity (Δh_i) is obtained by rewriting Equation 2.1:

$$\Delta h_i = \frac{f_i h_i}{AE} \quad (2.11)$$

where E is Young's modulus, Δh_i is the compression of the asperity due to force f_i, h_i is the height and A the cross-sectional area of the ith asperity. The deformation of the half-spaces due to the force acting on the asperity (d_{ii}) is given by Equation 2.5, and the deformation of the half-spaces due to forces acting on other asperities (d_{ij}) is given by Equation 2.10.

Having specified all of the components of displacement, it is possible to define a compliance matrix C such that C times the vector of forces acting on the asperities gives the vector of displacements at the asperities. More formally, C is an $n \times n$ matrix where n is the total number of asperities. The diagonal terms (C_{ii}) are such that $C_{ii} \cdot f_i$ is the average displacement at asperity i due to the force acting on asperity i while the off-diagonal terms (C_{ij}) are such that $C_{ij} \cdot f_j$ is the average displacement at asperity i due to the force acting on asperity j. To obtain the compliance terms, the forces f_i are factored out of the displacement equations as explained previously (see Equation 2.7). Define $\bar{d}_{ii}{}'$, $\bar{d}_{ij}{}'$, and $\Delta h_i{}'$ such that

$$\bar{d}_{ii} = \bar{d}_{ii}{}' \cdot f_i$$
$$\bar{d}_{ij} = \bar{d}_{ij}{}' \cdot f_j$$
$$\Delta h_i = \Delta h_i{}' \cdot f_i$$

where $\bar{d}_{ii}$ is the average displacement of the half-space beneath asperity i due to force f_i, $\bar{d}_{ij}$ is the average displacement of the half-space beneath asperity i due to force acting on asperity j, and Δh_i is the compression of the asperity. Then, the terms in the compliance matrix can be written as:

$$C_{ii} = \Delta h_i{}' + 2 \cdot \bar{d}_{ii}{}'$$
$$C_{ij} = 2 \cdot \bar{d}_{ij}{}' \quad .$$

Thus, the total average displacement at the ith asperity is $\bar{D}_i$ where:

$$\vec{D}_i = \sum_{j=1}^{n} C_{ij} \cdot f_j \qquad . \qquad (2.12)$$

In other words, the total displacement at the ith asperity is the linear combination of the displacements caused by the forces acting on all asperities. The full mathematical formulation is:

$$\vec{D} = C \cdot \vec{f}' \qquad (2.13)$$

where $\vec{D}$ is the vector of displacements, C is the compliance matrix and $\vec{f}$ is the vector of forces acting on the asperities. Equation 2.13 gives the desired relationship between force and displacement when deformation of the half-spaces and interaction between asperities are included in the model.

Accounting for interaction introduces another level of complication in the solution technique because specifying the displacement across the fracture no longer specifies which asperities are in contact. As was discussed at the beginning of this section, whether or not an asperity is in contact depends not only on its own height, but also on the deformation of the half-space beneath the asperity that has occurred because of the forces acting on other asperities. Thus, unlike Cases I and II, specifying a constant displacement boundary condition does not lead to a formulation that can be solved directly for the model with interaction. Both the displacement across the fracture and the distribution of force must be specified before the asperities in contact can be determined. Thus, for both stress and displacement boundary conditions, the iterative scheme previously described must be used to find the distribution of forces across the asperities.

The fracture deformation model was first developed assuming a constant stress boundary condition because it was first used to model laboratory experiments which

were conducted at specified stresses. The iterative procedure was used to determine the force distribution and the fracture stiffness. The original model worked well if all asperities were of equal height or if the number of asperities was small; e.g. the original model worked well as a means of calculating the stiffnesses of the artificial fractures created in the laboratory for the seismic experiments (see Hopkins et al., 1986). However, extending the model to rough surfaces and to dimensions deemed necessary for practical applications proved problematic. For the iterative procedure, the distribution of forces must be calculated each time a new asperity comes into contact and this entails inverting the coefficient matrix. Thus, for large numbers of asperities, the solution procedure becomes numerically intensive. Further, some problems with numerical stability were encountered. For these reasons, the problem was reformulated as a constrained energy minimization problem which is amenable to a more direct solution technique. Initial results indicate that the method, described below, should allow the study of complicated surfaces of more practical size.

3. An Energy Model

In the original model, the state of stress across the fracture was determined from the solution of the boundary-value problem described in the previous section (Equation 2.13). An alternative approach, discussed by Sokolnikoff, is a solution based on energy theorems which describe the equilibrium states of elastic bodies (p. 377). For the problem at hand, the deformation of the fracture surfaces and asperities can be described as explained in the previous section (Case III). The solution technique based on minimization of energy is described below. In brief, the work done in deforming

the fracture can be calculated from the displacement profile. From the work, an expression for strain energy can be derived that is subject to the theorem of least work. The theorem provides a vehicle by which the force distribution can be found.

Sokolnikoff defines strain energy to be the total work done against internal forces during loading (p. 247). More specifically, if a stress across the fracture results in displacements u_i, then the strain energy U is equal to the work done by the external forces on the body in bringing it from the original position to the new equilibrium state characterized by the displacements u_i. Equivalently, strain energy is the potential energy stored in the elastic body.

It is important to note that in calculating work, the displacements considered are the work-absorbing components of the actual displacements (see Den Hartog, p.212). For the model of the fracture presented here, the work-absorbing components of the displacements are the deformations of the fracture surfaces directly above and below the asperities in contact, and the compression of the asperities themselves. Thus, the work done when a stress is applied across the fracture can be computed from the compliance matrix defined in the previous section (see Equation 2.13); i.e., the work absorbing displacements are those that result from multiplying the compliance matrix C and the force vector $\vec{f}$. The work is, by definition, the product of the forces and displacements:

$$Work = \vec{f}' \cdot C \cdot \vec{f} \quad . \tag{3.1}$$

The connection between work and strain energy is provided by Clapeyron's Theorem:

> if a body is in equilibrium under a given system of body forces and surface forces then the strain energy of deformation is equal to one-half the work

that would be done by the external forces (of the equilibrium state) acting through the displacements from the unstressed state to the state of equilibrium (Sokolnikoff, p.86).

Substituting from the above equation:

$$Strain \quad energy = \frac{1}{2}[\vec{f}' C \vec{f}] \quad . \tag{3.2}$$

The importance of the above derivation is that it results in an expression for energy which is subject to the energy theorems derived for Hooke's-law materials. The theorem of use here has different names depending on author, but states that the strain energy attains its minimum value when the stress distribution corresponds to that of the equilibrium state. A more formal statement is given by Den Hartog (p. 212):

> The *theorem of least work* states that among all stress distributions in an elastic body or system which satisfy equilibrium, but which do not necessarily satisfy compatibility, the true or compatible stress distribution has the least elastic energy in the system, all other non-compatible stress distributions having greater energy than the true one.

Application of this theorem to the expression for energy given in Equation 3.2 provides a method for computing the distribution of stress across the asperities: the solution is the stress distribution that minimizes the strain energy in the system. Further, the solution is constrained to be physically realizable and satisfy compatibility which ensures continuity of deformation. Thus, the solution is the distribution of stress that minimizes Equation 3.2 subject to the constraints that the forces are positive and produce displacements consistent with those specified by the compliance matrix. The minimization is performed numerically and is more efficient and stable when the solution is constrained as much as possible. For that reason, constraints in addition to those needed to satisfy compatibility are imposed.

For simplicity, consider a single asperity between two half-spaces. Assume that initially the asperity is just barely in contact, i.e. that the initial separation of the half-spaces is h_i, the height of the asperity (see Figure 9a). Assume further that the half-spaces are brought together by an amount d so that the new separation (away from the asperity) is b where $b = h_i - d$, the original separation minus the displacement (Figure 9.b). It is important to note that the surface separation is not constant because the asperity indents the half-spaces; the aperture is only equal to b at distances outside the range of influence of the asperity.

For asperities in contact,

$$\overline{D}_i + \Delta h_i + b = h_i \qquad (3.3)$$

where $\overline{D}_i$ is the total average displacement of the half-spaces, Δh_i is the compression of the asperity, b is the separation of the half-spaces (away from the asperity) and h_i is the height of the asperity (see Figure 9b). The problem, as already discussed, is that even for a constant displacement boundary condition it is not known which asperities are in contact so it is not known for which asperities Equation 3.3 holds. Some asperities taller than the surface separation b will not be in contact because of the displacement beneath them due to the forces on neighboring asperities (see Figure 8). For these asperities,

$$\overline{D}_i + b > h_i \quad . \qquad (3.4)$$

There is no term for compression of the asperity because there is no contact. However,

$$\overline{D}_i + b < h_{\max} - \Delta h_{\max} \qquad (3.5)$$

where $h_{\max}$ is the height of the tallest asperity (see Figure 9c). That is, the maximum possible separation of the half-spaces after a force has been applied is the aperture at

the tallest asperity which is approximately the height minus the compression of the asperity. Combining Equations 3.4 and 3.5 and solving for the displacement of the half-spaces yields the following expression for asperities not in contact:

$$h_i - b < \overline{D}_i < h_{\max} - \Delta h_{\max} - b \quad . \quad \quad (3.6)$$

Combining Equations 3.3 and 3.6 results in bounds on the displacements at all asperities:

$$h_i - b - \Delta h_i \leq \overline{D}_i < h_{\max} - \Delta h_{\max} - b \quad . \quad \quad (3.7)$$

It is also possible to constrain the forces. Assuming a constant displacement boundary condition, the force acting on an asperity cannot be greater than it would be if the asperity were the only one separating the two half-spaces defining the fracture. Without interaction, the force required to close the fracture the specified amount is that given by Equation 2.8 (Case 2 in the previous section). This is an upper bound on the force that will be carried by the asperity; the force will be lower if there are neighboring asperities that carry force and displace the half-spaces at the position of the asperity in question. Thus, for all asperities, the force is bounded by zero and the force given by Equation 2.8. The result is that we have a constrained minimization problem. The objective is to find the distribution of force that minimizes the strain energy given by Equation 3.2 subject to the constraints specified by Equations 2.8 and 3.7.

The function to be minimized is nonlinear in the force variables and is thus among the class termed *nonlinear programming problems*. However, because Equation 3.2 is quadratic, the problem falls in the special category of quadratic programming problems.

Quadratic programming has its roots in linear programming which addresses the

problem of minimizing or maximizing a function of N independent variables subject to constraints. The function to be optimized (minimized or maximized) is called the objective function. The constraints can be of two forms. Primary constraints are constraints on the variables of the form:

$$u_i \leq x_i \leq l_i, \qquad x_i = k \qquad .$$

General constraints are of the form:

$$\begin{bmatrix} l_1 \\ l_2 \\ : \\ l_n \end{bmatrix} \leq \begin{bmatrix} A_{1,1} & A_{1,2} & A_{1,n} \\ A_{2,1} & A_{2,2} & A_{2,n} \\ : & : & : \\ A_{n,1} & A_{2,n} & A_{n,n} \end{bmatrix} \begin{bmatrix} x_1 \\ x_2 \\ : \\ x_n \end{bmatrix} \leq \begin{bmatrix} u_1 \\ u_2 \\ : \\ u_n \end{bmatrix} \qquad .$$

As can be seen in the above expressions, the constraints are linear combinations of the independent variables. Equality constraints can be specified by setting l_i equal to u_i.

A brief but easily readable description of the solution technique is given by Press et al. in their book on scientific computing (Press et al., pp. 312-326). A feasible vector is defined as a set of values of the independent variables $\vec{x}$ that satisfies the constraints. In the abscence of constraints, the solution lies in a full N-dimensional space. The effect of the constraints is to restrict the solution to a smaller region of that space. Because the constraints are linear, each represents a hyperplane that bounds the solution region. (In N-dimensional space, a hyperplane is of dimension $N-1$.) Equality constraints restrict the solution to hyperplanes of smaller dimension while inequalities divide the space into feasible and nonfeasible regions. When all constraints have been imposed, the result is a feasible region to which the solution is confined (assuming that such a region exists). The problem now is to examine the set of feasible vectors in some efficient way to find the one that optimizes the objective function. The linear programming problem is usually solved using the *simplex method* (see Press et al., p.

315).

As explained above, the problem of finding the distribution of force across a rough surface is a quadratic programming problem. Though the objective function is quadratic in the independent variables, the constraints are linear. Thus, the constraints define a feasible region exactly as outlined above for the linear programming case. The problem in this case is to find the feasible vector that optimizes the quadratic objective function.

The NAG mathematical software library, a collection of FORTRAN routines that is well documented and tested, is being used to perform the minimization. The specific routine being used is particularly attractive because it was designed specifically to solve the the problem of minimizing a quadratic function subject to a set of linear constraints on the variables. As described in the library documentation, the solution method has two distinct phases. In the first, an iterative procedure is used to find a feasible starting point. The user sets tolerances which specify the degree to which the constraints can be violated. A feasible point is defined as one such that all constraints are satisfied within the specified tolerances. In the second phase, the quadratic function is minimized using standard techniques (see Press et al., pp. 521-528). In short, the method is an iterative one. A starting point is supplied by the user and successive evaluations of the objective function are made until a minimum is found. The solution technique makes use of the Hessian matrix (the matrix of second partial derivatives of the objective function) to define a search direction at each iteration. Successive line minimizations are performed until convergence within specified limits is achieved. Because of the mathematical properties of the Hessian, efficient algo-

rithms can be employed to find the minimum.

The programming necessary to implement the energy solution has been completed and debugged. Tests are now being made to verify the method. To illustrate, the results of applying the model to a few simple cases will be presented. For the first example, consider the simple case of a row of 49 asperities of equal height. The asperities are of equal diameter (1 mm) and are spaced 0.5 mm apart. Asperities in the middle should carry equal force. Asperities toward the outside should carry slightly more force because they have fewer neighbors and the effect of interaction is smaller. The forces calculated with the energy model are consistent with what would be expected (see Figure 10).

As a second example, consider three variations of a surface profile. Again, the asperities lie on a line and are of equal diameter, but are not of equal height. In the first case, the surface profile is symmetric, the surface looking like a valley between two hills (Figure 1b). At the specified displacement, only two groups of asperities are in contact; asperities not in contact carry zero force. As would be expected, the calculated force curve is symmetric with respect to the topography (Figure 11a). Of the asperities in contact, the tallest ones carry the greatest force because it takes more force to compress them.

For the second case, the hills are of the same width but the second is taller than the first (Figure 11d). In this case, the asperities in the second hill carry more force because it takes more force to compress the taller asperities (Figure 11c). For the third case, the surface profile is not symmetric; the second hill is broader than the first, having more asperities (Figure 11f). The total force carried by the broader hill is greater

than that of the narrower hill because it has more asperities in contact (Figure 11e).

To illustrate a simple case in three dimensions consider the symmetric arrangement of equal height asperities: clusters of seven asperities in a ring around a central cluster (see Figure 12). Within a cluster, the central asperity would be expected to carry less force than the surrounding ones because the interaction effect is strongest at the center. This can be seen by looking at the innermost cluster of seven discs in Figure 12. The highest forces (indicated by solid circles) are on outermost asperities where there is the least interaction. Likewise, the central cluster would be expected to carry less force than the surrounding clusters. Again, the calculated forces are consistent with theory. Note also, that because of the symmetric design, each of the outer clusters carries the same total force (the sum of the forces on the seven discs comprising the cluster).

More complicated test cases are currently being developed and run. In particular, the model will be used to calculate deformation for surface geometries for which analytical solutions exist. One such solution is the Hertzian solution for a sphere in contact with an elastic half-space. A sphere will be modeled by a cluster of asperities and the calculated deformation will be compared to the result obtained from the analytical solution. Once the model has been tested, work will continue to study changes in fracture stiffness and aperture with stress.

4. Extension of the Model to Study Saturation and Surface Roughness

A new formulation of the fracture deformation model is being developed to study the

effects of saturation and surface roughness. Among the objectives of this work is the ability to construct the surface topography from a set of measurements of surface height and the capability of calculating a stress surface, positive at points of contact and zero elsewhere, that describes the distribution of force across the fracture surface. The first problem is to estimate the surface topography based on the measurements of surface height at specified locations. The second problem is to determine how a far-field stress is distributed across the fracture surface given asperities of known location and height.

Estimating fracture topography and a corresponding stress surface could both be treated as curve fitting problems. Several curve fitting procedures, e.g. polynomial fitting, give equal weight to all data points and can result in very smoothed curves and surfaces. This is particularly undesirable for the fracture problem because the rough-ness of the fracture is an important parameter playing a significant role in both mechanical deformation and fluid flow. Thus, the procedure chosen should be one that preserves the roughness of the data. A more attractive method is nonparametric b-spline regression. As explained by B. W. Silverman (1985), spline smoothing does well even if the data points are not regularly spaced and smooths locally so that local variation is preserved (Silverman, p.4). Only a brief description of the method will be given here; for a full discussion see Silverman (1985).

The discussion here will be limited to the one-dimensional case of estimating a curve. The problem is to estimate a curve $Y(x_i)$ on an interval (A, B). In this case, a b-spline of order k is a collection of polynomials of degree $k-1$ defined on a subdivi-sion of the interval (A, B). The spline representation of the curve $Y(x_i)$ is

$$Y(x_i) = \sum_{j=1}^{p} \alpha_j B_j(x_i) \qquad (4.1)$$

where the coefficients α_j are parameters estimated from the data. The B_j are basis functions which are zero except on k adjoining intervals and are usually smooth, bell shaped curves (see Silverman, p.4). Thus, the estimated curve is piecewise polynomial, each point on the curve being a linear combination of the polynomial basis functions. Local variation is preserved because each basis function is only nonzero over k of the subdivisions of (A,B).

4.1 Estimation of surface topography from a sample of surface height measurements

Consider first the problem of constructing the surface topography from the sample points. We assume that measurements of the surface topography have been made; i.e. that we have observations Y_i of surface height measured from some reference plane at points x_i. Again, the discussion will be limited to the one-dimensional case of a surface profile. In this case, the problem is to determine the topography over the length of the profile. We assume that the observations satisfy

$$Y_i = f(x_i) + \varepsilon_i$$

where the ε_i are independent $N(0,\sigma^2)$ errors and f is the unknown curve to be estimated.

If posed as strictly a curve fitting problem, a reasonable criterion for fit would be one based on the residual sum of squares:

$$\sum [Y_i - f(x_i)]^2 \ .$$

If the curve f is not restricted in any way, then the residual sum of squares can be

driven to zero by allowing the curve to pass through all of the data points. As explained by Silverman, an interpolant of this form would usually be rejected by statisticians on the grounds that its rapid fluctuations were implausible.

· The problem that Silverman is addressing is that of estimating a probability density function which is usually quite smooth. Unlike a probability density function, a fracture surface is not necessarily smooth and rapid fluctuations in topography are not necessarily implausible. Instead of restricting the estimate to be smooth, we want to use Silverman's approach to estimate a surface whose roughness is consistent with the rock type and geologic history of the fracture.

Silverman describes two methods that are used to avoid what are considered to be implausible estimates because of rapid fluctuations. In the first, only curves f which fall in some specified parametric class are considered. This is not a realistic solution to the fracture problem because it would not be reasonable to say that the function describing surface topography is given by a specific statistical distribution. The second approach is to introduce a roughness penalty to the model. This requires some measure of rapid local variation such as the integrated squared second derivative. Introducing this term results in a modified sum of squares defined by Silverman to be (p. 4):

$$R(f) = \sum [\, Y_i - f(x_i)\,]^2 \; + \; \alpha \int f''(z)^2 dz \;\; . \tag{4.2}$$

The parameter α is a smoothing parameter which represents the tradeoff between residual error and local variation. Minimizing $R(f)$ yields the best fit curve with the desired smoothness.

For the fracture problem, introducing the parameter α has special appeal because of its physical meaning. As previously discussed, the roughness of the fracture is a

parameter of interest determined by the material properties of the rock and the geologic history of the fracture. Instead of restricting the estimate to be smooth, we want to restrict our attention to those curves Y with roughness consistent with the properties and history of the fracture.

At present, there is no accepted way of computing a value for fracture surface roughness. An attractive feature of the spline approach is that α is an estimable parameter that describes surface roughness. To obtain an estimate of α for any given rock type would require measurements of surface topography from many different fractures. However, such data is now being collected by a number of researchers so that such an analysis will be possible in the future. Further, by estimating the roughness of a fracture for which hydraulic and mechanical properties can also be measured, we can increase our understanding of the relationships between the three.

In the abscence of information about the roughness parameter α, Equation 4.1 can be used to construct a profile of the surface from measurements of surface height at specified points. If information about the roughness is known, then the formulation specified in Equation 4.2 can be used. For either case, the methodology is the same. The surface profile to be estimated is formulated as per Equation 4.1; i.e.

$$Y(x_i) = \sum_{j=1}^{p} \alpha_j B_j(x_i) \quad . \tag{4.3}$$

The problem is to estimate the α_j to minimize Equation 4.1 or 4.2; i.e. to find the α_j that minimize the squared error difference between the measured points and those on the estimated profile (consistent with the surface roughness if known). For work done to date, a library of public domain, mathematical subroutines is being used to estimate the α_j, calculate the basis functions B_j and evaluate the estimated curve Y. The NAG

mathematical software library, as described in Section 3, is being used to perform the minimization.

4.2 Construction of a stress surface from forces calculated at asperities

The same methodology described above can be used to find the distribution of stress across the fracture given forces calculated at asperities. The distribution of force at the asperities obtained from the sampled topography would be calculated using the energy method described in the previous section. The spline method discussed here would then be used to find the distribution of stress over the fracture surface. This case is analogous to the case described above where the fracture topography is estimated from measurements of surface height at discrete points. Using the spline formulation, the stress surface to be estimated ($\sigma(x)$) would be represented as:

$$\sigma_i = \sigma(x_i) = \sum_{j=1}^{p} \alpha_j B_j(x_i) \quad . \tag{4.4}$$

Exactly as above, the α_j would be estimated to minimize Equation 4.1, i.e. to minimize the difference between the squared error difference between the estimated stress surface and the stress calculated at the asperities using the energy model of Section 3.

The second approach is to build the spline formulation into the energy model so that the continuous stress surface is solved for explicitly. More precisely, the unknown force function is formulated as a spline function. The problem then is to specify an expression that can be minimized to yield a curve (in two dimensions) or a surface (in three dimensions) representing the desired stress function. The most important consideration in constructing the function to be minimized is to build in as much physics

to the model as possible. One of the advantages of the energy model presented in the previous section is that it lends itself well to extension to the continuous formulation described here. That is, the energy minimization equations developed in the previous section can be modified to be consistent with the spline representation of stress and can then be solved in the exact same manner as explained previously. The problem, if specified in this way, is to find the distribution of stress, represented by a surface, that minimizes the strain energy in the system, consistent with the compliance matrix based on the data points, subject to the constraint that the integral of the stress over the fracture surface is equal to the applied load.

In addition to the physical constraints, it is possible to specify an error term based on the total displacement across the fracture. From the reciprocal theorem we know that the total displacement of the half-spaces defining the fracture will be the same for the rough surface as it would be if the force were uniformly distributed over the half-spaces (see Timoshenko, p.63). (Note, that while the total volume of displacement will be the same, the displacement profiles will be very different.) Thus, we know that our estimated stress function should yield a total displacement that is equal to what would be obtained for a uniform stress. In terms of the model, the estimated force function should minimize the difference between the total displacement calculated using the estimated force for the rough surface and that calculated for a uniform stress.

To incorporate this term into the model, it is necessary to be able to calculate the deformation of the half-spaces for a uniform stress. If we want to estimate the force distribution for a row of asperities along a line, then the loaded area is rectangular and we can use Timoshenko's solution for displacement below a uniformly loaded rectan-

gle (p. 407). For asperities distributed across a surface, we can assume that the fracture surface is a circular area and use the Bousinesq solution for displacement below a uniformly loaded circle.

A third criterion that can be specified is that the estimated force function be consistent with the topography data. To include such a term in the model requires a way of calculating some measure of surface roughness. As discussed above, one measure suggested by Silverman is the integrated second derivative of the function in question. Assuming that the true force distribution maps the surface topography reasonably well, a possible roughness penalty term is one based on the integrated second derivative of the force function.

Finally, we can state our problem in the form of a function to be minimized: we want to find the distribution of forces that minimizes the strain energy in the system and the squared error difference between the estimated and true total displacement, and one that is consistent with the surface roughness (if known). Mathematically, this may be expressed as minimize:

$$f'C f + [c - f'b]^2 + \alpha \int f''(x)^2 dx$$

subject to the integral of the stress over the fracture being equal to the applied load.

This formulation has been programmed and debugged for the one-dimensional case of a surface profile. Simple test cases are now being run to debug the program and verify the method.

SUMMARY

A new series of laboratory experiments was performed. Pairs of idealized fractures were created by placing thin lead strips between steel cylinders. The objectives of the current program were to study the effect of multiple fractures on the propagation of seismic waves, study the degree to which seismic methods can discriminate between fractures, and test the thoery that specifies seismic wave propagation across a fracture based on its mechanical stiffness. The results of the experiments were the same for both P- and S-waves. The seismic signal propagated across the two fractures was nearly identical in amplitude and frequency content for all spacings except for the closest spacing (equal to one-tenth of the seismic wavelength). At this close spacing there was an increase in the signal amplitude. One explanation for this increase in amplitude is that at close spacings the fractures are interacting mechanically. The seismic wave begins to see a single interface rather than two distinct fractures. Because of mechanical interaction, the closely spaced fractures have a stiffness that is slightly greater than the combined stiffnesses of the two fractures more widely spaced.

For both the P- and S-waves, the waves propagated across the two fractures were significantly reduced in amplitude, delayed in time, and have a different frequency content than waves propagated through solid steel. This result shows that despite the small thickness of the fractures in relation to the seismic wavelength, they do reflect, transmit and delay seismic waves. Further, parallel fractures can be regarded as independent until the spacing between them becomes small compared to the seismic wavelength.

Additional laboratory experiments are planned for the current year. The multi-layer experiments will be repeated with fractures of different stiffnesses to see if

results obtained thus far hold in general and to test how well the seismic theory based on mechanical stiffness holds for multiple fractures. In parallel, analytic work will be done to determine when parallel fractures interact mechanically. For fractures that do interact mechanically, an attempt will be made to determine what single fracture stiffness should be used to correctly predict the transmission of seismic waves across the two closely spaced fractures.

The analytical model originally developed to calculate the stiffnesses of the fractures created in the laboratory, and later extended to study changes in fracture stiffness and aperture with stress, has been significantly modified. Accounting for deformation of the half-spaces and interaction between asperities introduces a level of complexity in the solution that made it difficult to apply the original model to fractures of a dimension deemed necessary to model field conditions. The model has been reformulated so that a solution technique based on energy minimization can be applied. As in the original model, the fracture surface is represented by variable height asperities. The deformation of the asperities is calculated from Hooke's Law. The displacement of the half-spaces defining the fracture is calculated from the Bousinesq solution for displacement below a loaded circle. The work done in deforming the fracture can be calculated from the displacements and can, in turn, be used to derive an expression for strain energy. Being able to calculate strain energy is important because of the existence of theorems derived for Hooke's law materials that state that strain energy is a minimum for the state of stress that satisfies equilibrium and compatibility. The stress across the fracture can be determined numerically by finding the distribution of stress that minimizes the strain energy and is compatible with the displacements. The energy model has been implemented and is now being tested.

The energy model is now being extended to incorporate the effects of pore and capillary pressure and to explicitly include a term corresponding to surface roughness. In this formulation, the force across the fracture is represented by a stress surface, positive at points of contact and zero elsewhere. The method being used to estimate the stress surface is nonparametric b-spline regression. The method can be used in three different ways: 1) to estimate the fracture topography based on a sample of surface height measurements; 2) to estimate a stress surface based on forces calculated at asperities using the energy model; 3) to estimate a stress surface explicitly by building the spline formulation of stress into the energy model. The programming necessary to do any of the three in one dimension (i.e. for a cross-section through the fracture) has been completed and debugged. Simple test cases are now being run to check the program and verify the method.

References

Den Hartog, J.P., *Advanced Strength of Materials*, McGraw-Hill Book Co., New York, 1952.

Hopkins, D.L., L.R. Myer and N.G.W. Cook, Seismic wave properties of idealized fractures in *Geotechnical Support and Topical Studies for Nuclear Waste Geologic Repositories: Annual Report*, Fiscal Year 1986, LBL Report 23069.

Hopkins, D.L., L.R. Myer and N.G.W. Cook, Fracture stiffness as a function of applied stress and fracture geometry in *Geotechnical Support and Topical Studies for Nuclear Waste Geologic Repositories: Annual Report*, Fiscal Year 1987, LBL Report 24758.

Hudson, J.A., Seismic wave propagation through material containing partially saturated cracks, *Geophysical Journal*, 92, pp. 33-37, 1988.

Mavko, Gerald M. and Amos Nur, Wave attenuation in partially saturated rocks, *Geophysics*, v. 44, no. 2, pp. 161-178, February 1979.

NAG Fortran Library Manual Mark 8, Chapter E04NAF, NAG Central Office, Oxford, U.K., 1980.

Press, William H., Brian P. Flannery, Saul A. Teukolsky, and William T. Vetterling, *Numerical Recipes - The Art of Scientific Computing*, Saul A. Teukolsky, and William T. Vetterling, Cambridge University Press, Cambridge, 1986.

Silverman, B.W., Some aspects of the spline smoothing approach to non-parametric regression curve fitting, *J. Royal Statistical Society*, 47, No. 1, pp. 1-52, 1985.

Sokolnikoff, I.S., *Mathematical Theory of Elasticity*, McGraw-Hill Book Co., New York, 1956.

Timoshenko, S.P. and J.N. Goodier, *Theory of Elasticity*, McGraw-Hill Book Company, New York, 1970.
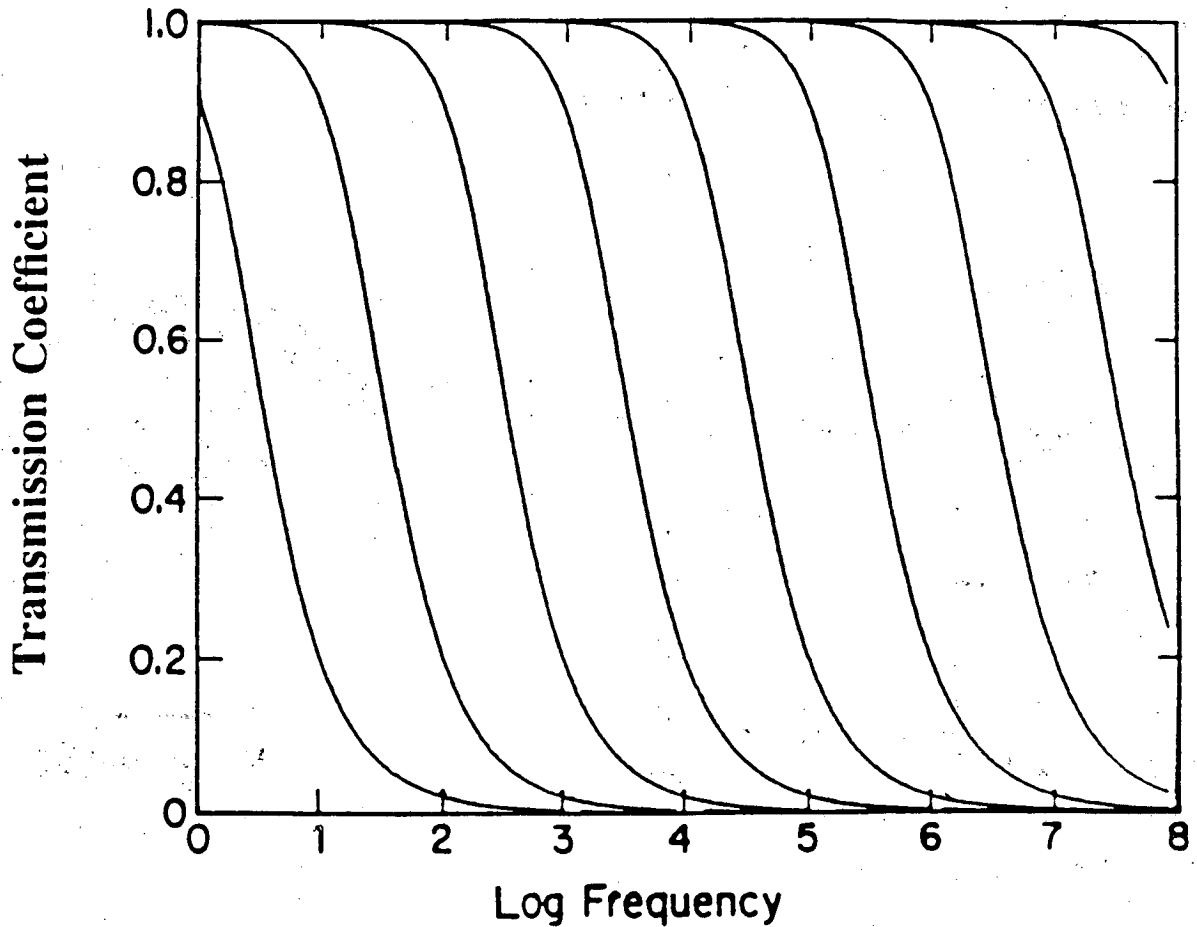
XBL 8410-9996 A

Figure 1.

Transmission coefficient for P-waves as a function of frequency for different fracture stiffnesses. A coefficient of one means that all the seismic energy is transmitted across the fracture. The figure shows that the transmission coefficient increases with increasing stiffness for all frequencies.

P-wave crystal
or
S-wave crystal — Spacer

Steel —

Interface —

Steel —

S-wave crystal
or
P-wave crystal — Spacer

Lead
strips

$2L$ $2R$
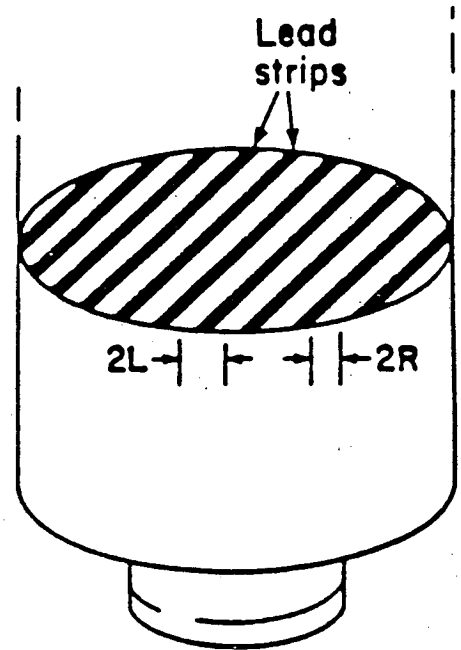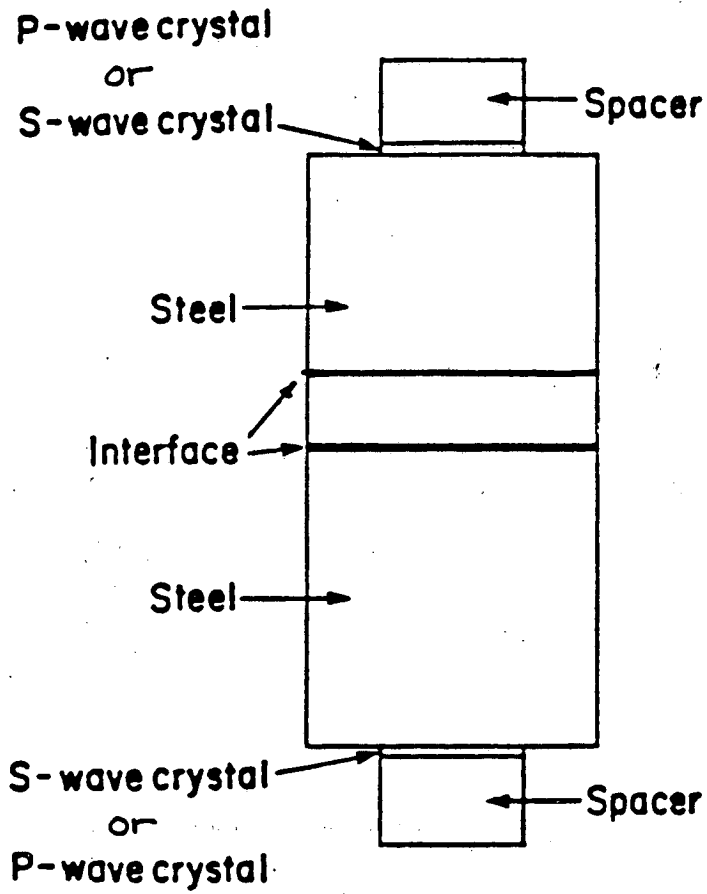
Figure 2.

Experimental set-up for multi-fracture seismic experiments.
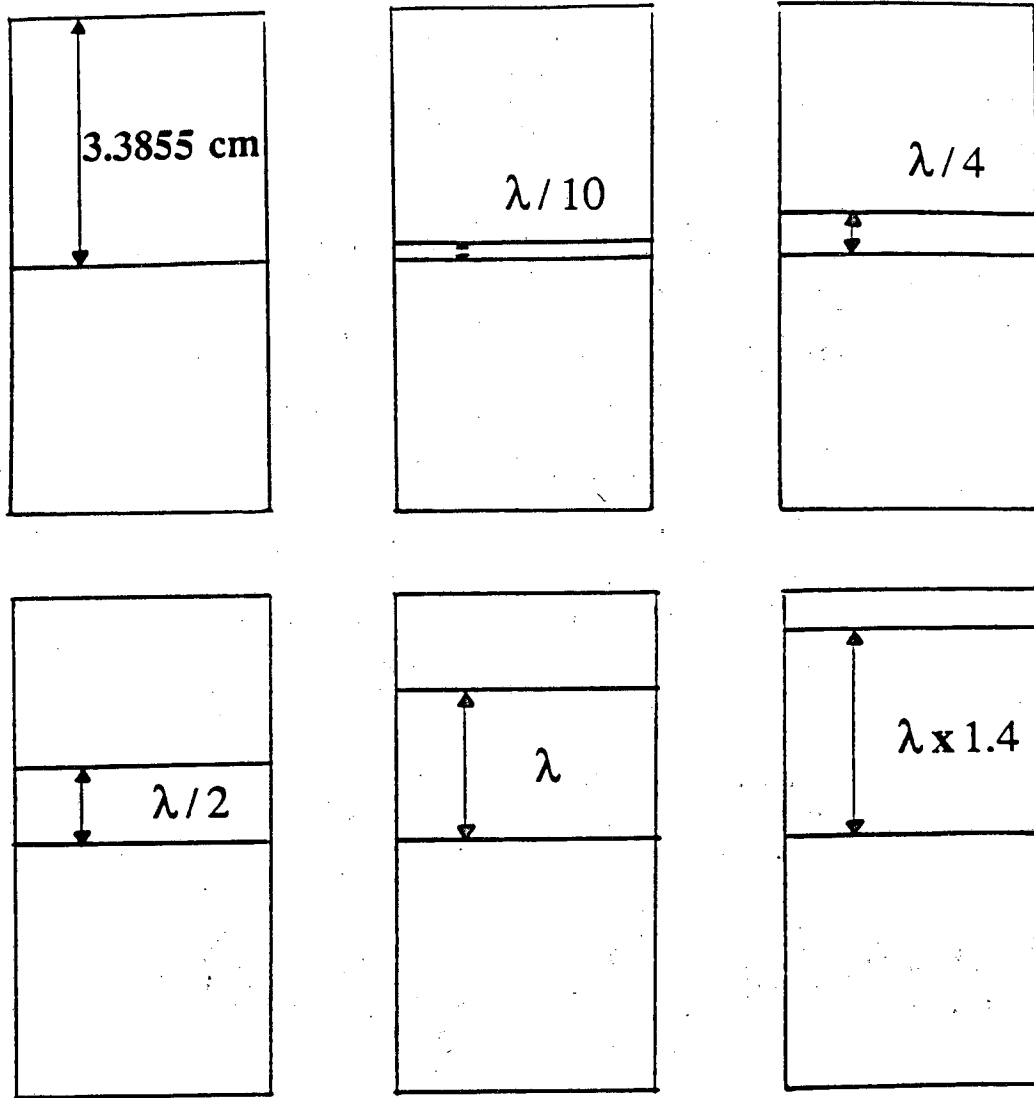
λ = the wavelength of the seismic signal

= 2.365 cm

Figure 3.

Experimental set-up designed to study the relationship between seismic wavelength and the distance between two parallel fractures.
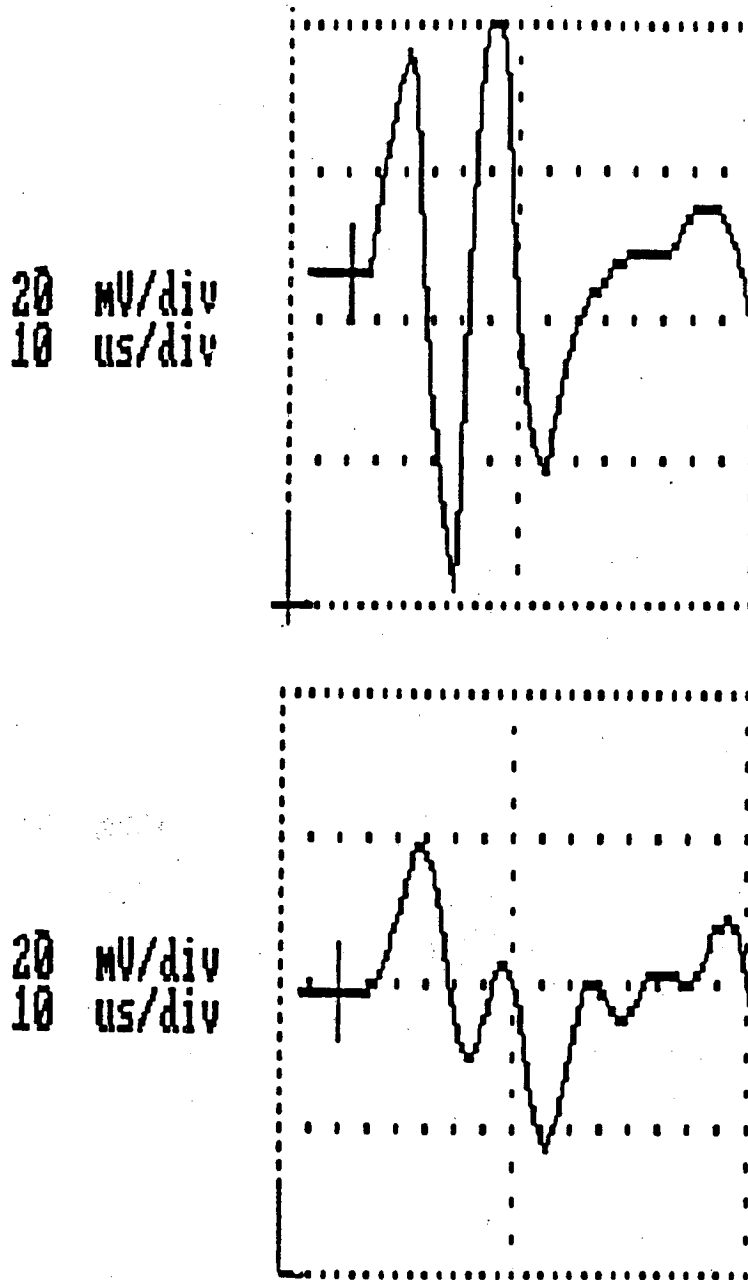
Figure 4.

P-wave signals obtained from solid steel (top figure) and steel containing two fractures (bottom figure). Comparison shows that the fractures cause a reduction in amplitude, change in frequency content, and delay of the received signal.
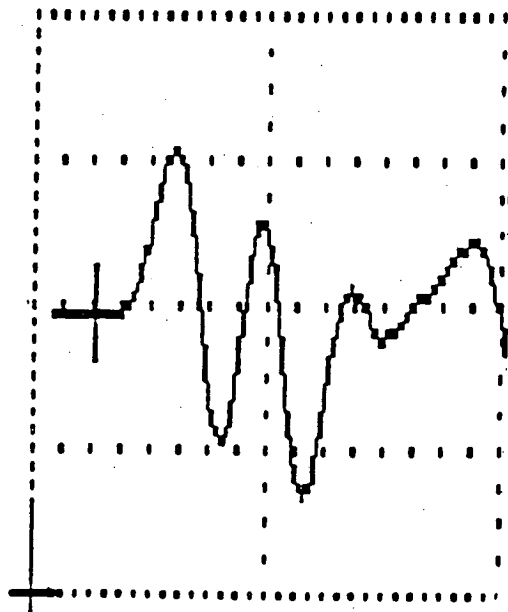
Figure 5.

P-wave signal obtained from steel with two fractures spaced very close together (spacing equal to 1/10 of the wavelength). Comparison with the waveform on the previous page shows an increase in amplitude; when the spacing between fractures becomes small, they begin to look like a single fracture.

50 mV/div
10 us/div

Figure 6.

S-wave signals obtained from steel with two fractures separated by four different spacings. Comparison shows that all have nearly equal amplitudes and frequency content except for the closest spacing (equal to one-tenth of the wavelength).
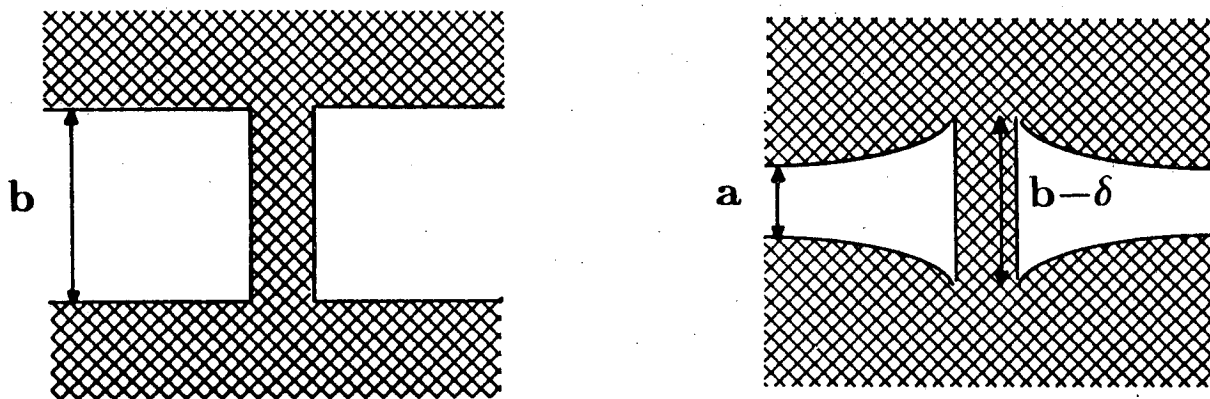
Figure 7.

Cross-section of aperture for a single asperity between parallel plates under zero load (a) and after a load is applied (b).
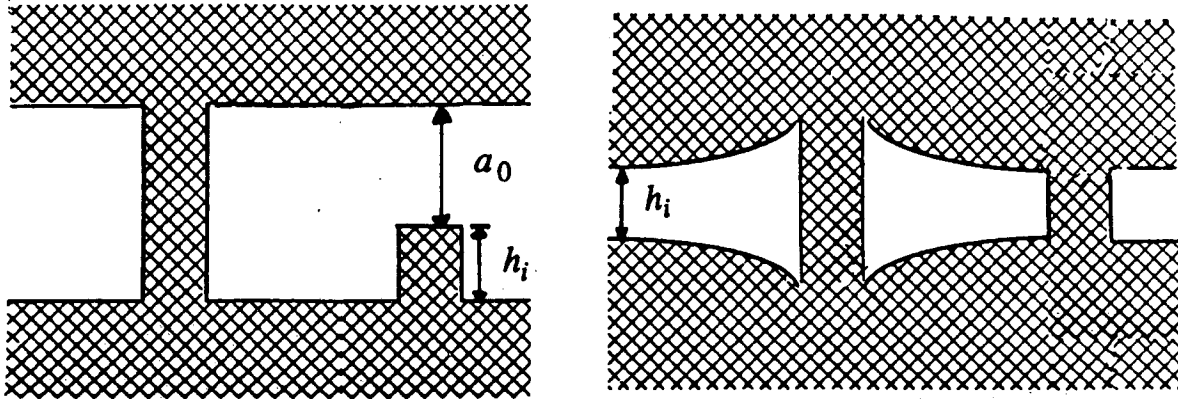
Figure 8a. Two asperities far enough apart so that mechanical interaction is negligible. The short asperity comes into contact when the average displacement across the fracture is greater than or equal to a_0.
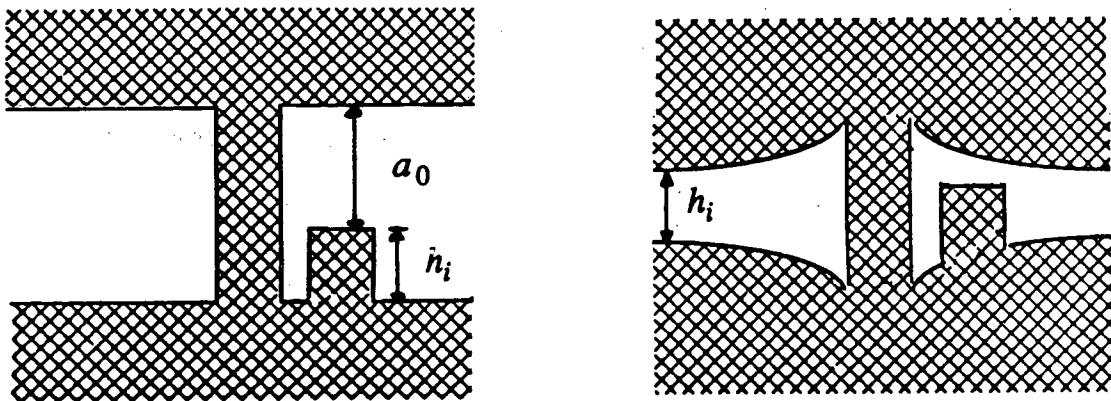
Figure 8b. Two asperities that interact mechanically. The force on the tall asperity causes displacement below the short asperity so that the average displacement across the fracture must be greater than a_0 before the short one will come into contact.
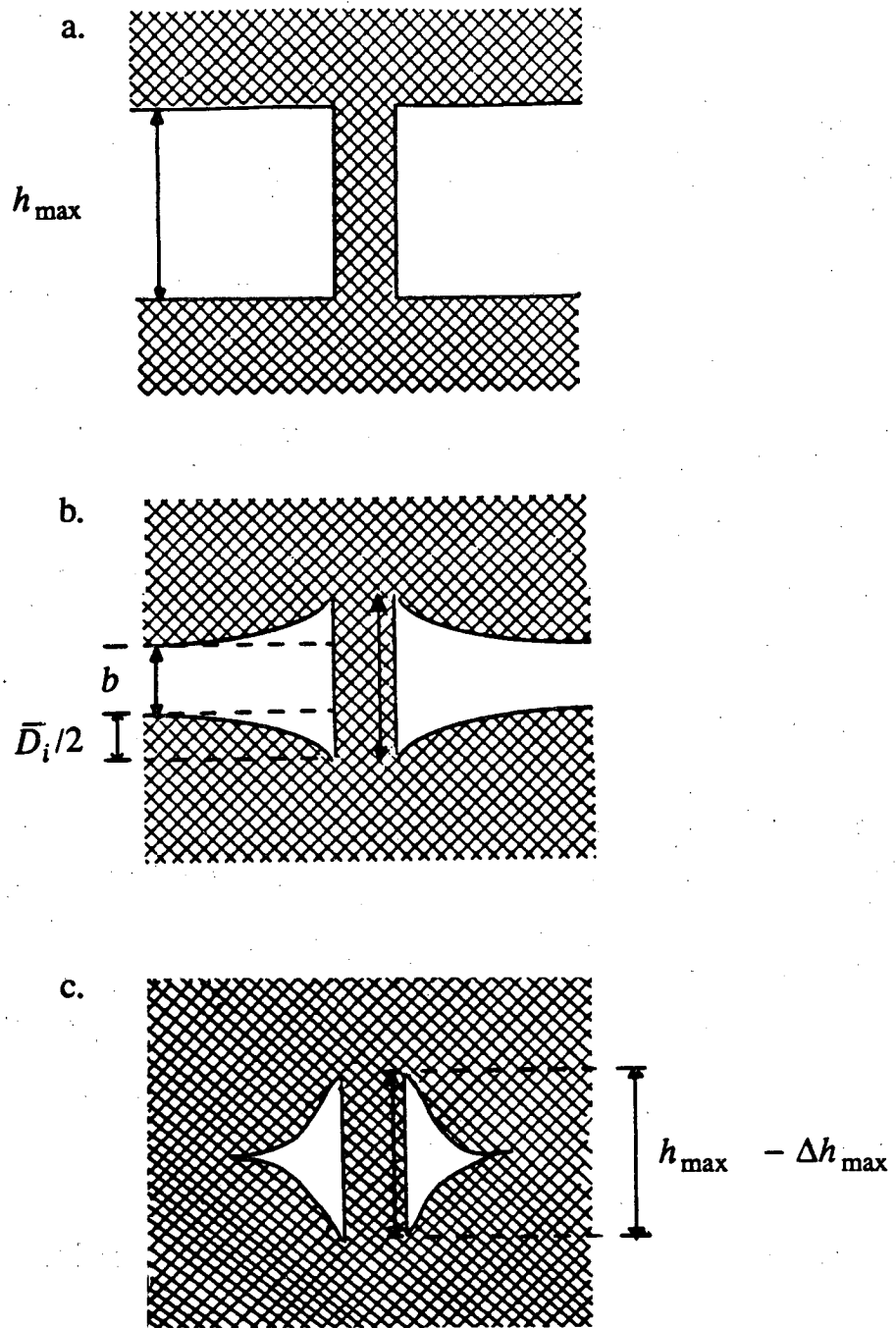
Figure 9. Fracture aperture at an asperity under zero load (a), after a load has been applied (b), and when the half-spaces defining the fracture are in contact (c).
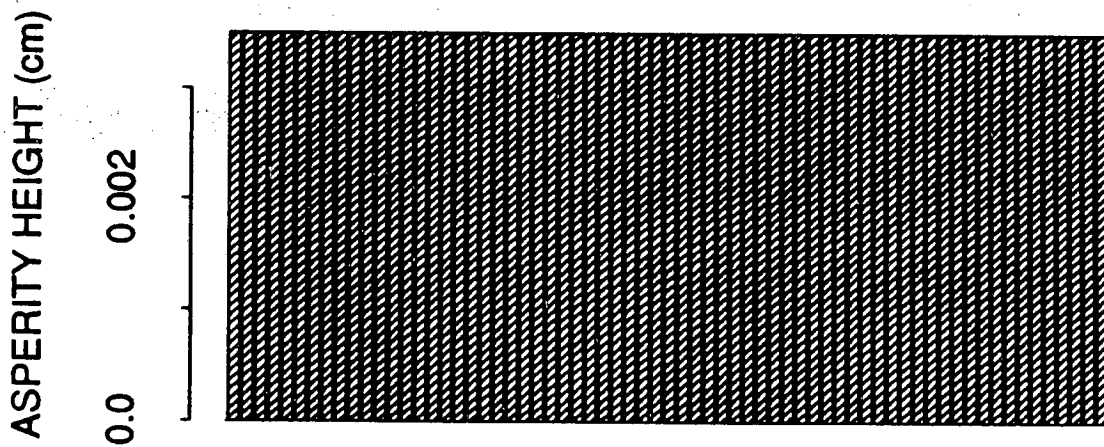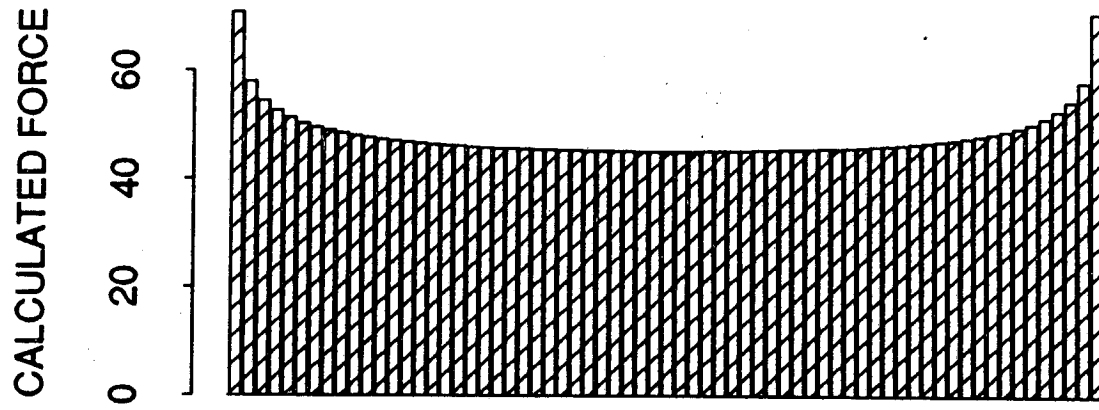
Figure 10. Calculated forces for
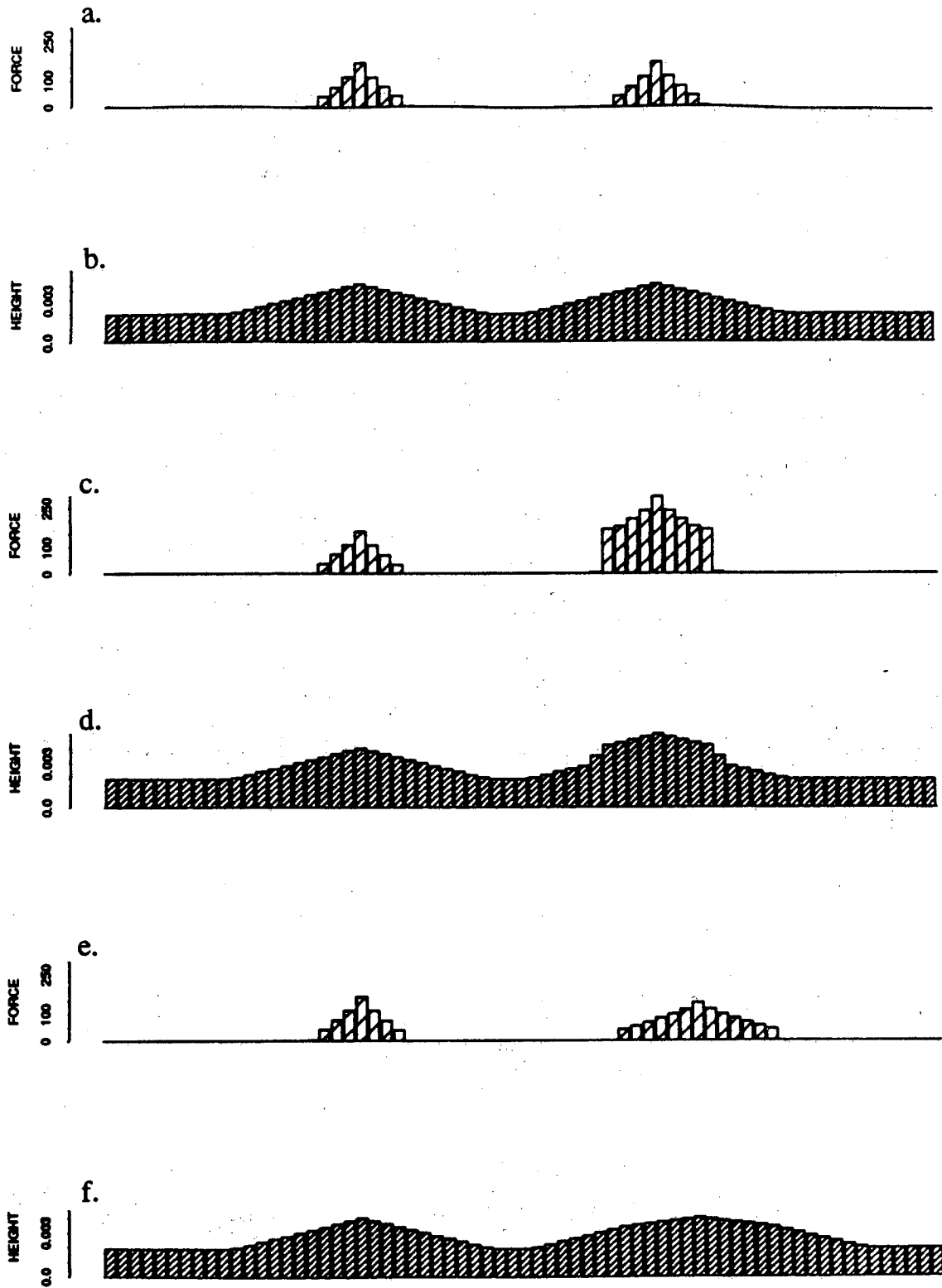a row of 67 equal height asperities.

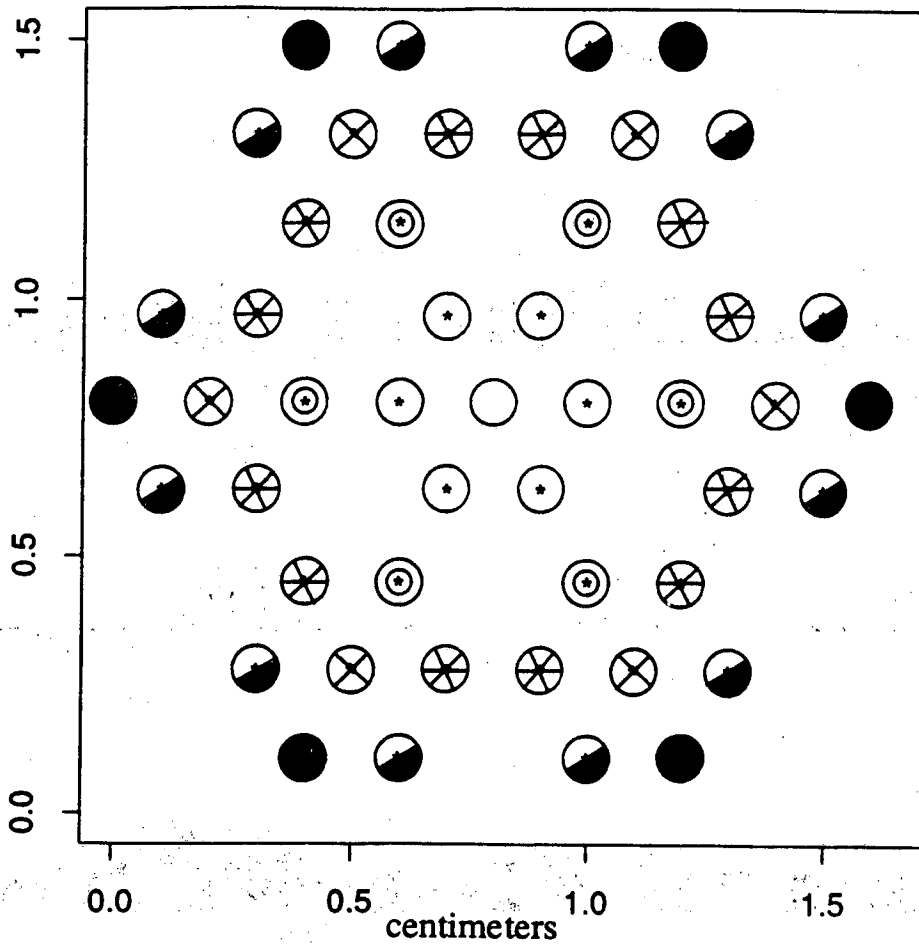**Figure 11.** Calculated forces and asperity height distributions for three different surface profiles.

Figure 12. Locations and calculated forces for a three-dimensional array of equal height asperities.

Tracer Transport in Fractured Rocks

C. F. Tsang, Y. W. Tsang and F. V. Hale

Introduction

Recent interest in the evaluation of contaminant transport in bedrock aquifers and in the performance assessment of a geologic nuclear waste repository has motivated many studies of tracer transport in fractured rocks. Some of these studies have assumed that fractures can be represented by disks with constant apertures. This is what is called the parallel-plate model. The experiments of Abelin et al. (1982) in the Stripa mines in Sweden first brought out the inadequacy of such a model. They showed that the mean parallel-plate aperture deduced from flow permeability data and that inferred from tracer transport time data differ by as much as one order of magnitude. This has been shown to be the result of the variable-aperture nature of the fractures (see e.g. Tsang, 1984).

The variable-aperture nature of a fracture results in a very heterogeneous system. Tracer particles flowing through such a system will follow paths of least resistance. These preferred paths of flow were observed in the experiments of Neretnieks (1985) and Bourke (1987) and others. Motivated by these data, Tsang and Tsang (1987) proposed the variable-aperture channel model for transport through fractured media. The properties of the channel model were further developed by Tsang et al. (1988) and the channeling characteristics of flow through a two-dimensional single fracture were analyzed in detail by Moreno et al. (1988).

The purpose of the present paper is to show how a detailed flow calculation in a two-dimensional variable-aperture single fracture gives rise to flow channeling. Because of the channeling effect, point measurements of tracer transport in the highly heterogeneous single fracture may give results with large fluctuations in value. The use of line,

areal or multi-point measurements provides a way to reduce the spread of the fluctuations and to correlate the mean of the measured values to the basic input parameters. Finally, we show how the tracer transport through a 2D single fracture with strongly variable apertures can be simulated with 1D variable-aperture channels, which are characterized by an aperture probability distribution function with two input parameters.

Channeling in 2D single fractures with strongly varying apertures

In this section we shall demonstrate the channeling characteristics of flow in a 2D single fracture with strongly varying apertures. We use an aperture density distribution for the aperture values over the single fracture. Measurements of aperture values were made by Gentier (1986) and Gale (1988) in laboratory core samples. Based on their results, we assume that these aperture values obey a log normal distribution, which is characterized by two parameters, the (arithmetic) mean aperture value, $\bar{b}$, and standard deviation (in log b), σ. The arithmetric mean is taken here because it is a well-defined quantity related to tracer transport. Figure 1 shows three distributions with the same value of $\bar{b}$ and different values of σ on a linear scale. It is of interest to note that as σ increases, the peak location of the distribution decreases and the half-widths of the distribution in b also decreases. If the distribution were plotted on a log scale, the half-width in log b would indeed increase with σ (Tsang et al. 1988).

Given the aperture distribution, the single fracture with variable aperture is constructed by means of standard geostatistical methods in a procedure described in Moreno et al. (1988). A number of realizations were generated. Here, we have introduced a third parameter, the spatial correlation length λ which is a measure of the distance over which the apertures are correlated. In this study we have assumed the system to be isotropic. Figure 2 shows one such realization, based on a log-normal distribution with $\bar{b} = 50 \, \mu m$ and $\sigma = 0.43$ and $\lambda = 0.1L$, where L is the dimension of the single fracture. The five shadings used in the figure illustrate the varying aperture values in five steps

from b < 22 μm to b> 116 μm.

Now let us apply a pressure difference across the single fracture saturated with water. In Figure 3a let the pressure on the left side be P_1; on the right side P_2, and the top and bottom sides be closed to water flow. If we assume that locally the permeability to fluid flow is proportional to the square of the local apertures, then the resistance to flow between two adjacent mesh elements i and j (Figure 3b) is

$$R_{ij} = 6\mu \frac{\Delta x}{\Delta y} \left[\frac{1}{b_i^3} + \frac{1}{b_j^3} \right],$$ where μ is value of fluid viscosity. Then the fluid flow

through the fracture can be calculated by solving a matrix equation relating the pressures at all the points in the fracture. A similar calculation can also be made if we apply P_1 and P_2 to the top and bottom sides of the fracture with the left and right sides closed to water flow.

Figure 4a shows the flow when the pressure difference is applied on the left and right sides of the fracture and Figure 4b shows the flow when the pressure difference is applied on the top and bottom sides of the fracture. For illustrative purposes we have shown the flow pattern by arbitrarily making the thickness of the lines in the figure to be proportional to the square root of the local flow rates. The flow rates at different locations in the fracture vary greatly, by orders of magnitude. It is apparent that in both the left-right and top-bottom flow patterns preferred flow paths are present, though they are different geometrically for the two flow directions. The exit flow rates in both cases range from 0.001 to 100 units and are shown in Figures 5a and 5b. These preferred flow paths are what we called channels, along which the apertures are variable. Thus, these channels are NOT fixed large-flow tubes embedded in the fracture plane, but are preferred flow paths, in the sense of stream-lines or stream-tubes in the hydraulic potential theory, due to the strong variation of the aperture and hence, permeability value.

The channeling effects described here occur in addition to the physical or structural large-permeability channels in the fractured medium, such as those observed near the

intersection of orthogonal fractures (Abelin et al. 1988).

Now, as can be seen in Figures 4a and 4b, for the same fracture, flow channels observed for applied left-right and up-down pressure differences are quite different geometrically. What, then, characterizes these channels? To study this, we calculate tracer transport through the fracture using the particle tracking method (see e.g. Smith and Schwartz, 1980 and Moreno et al. 1988). A sufficiently large number of particles, in our case ten thousand particles, are introduced on the high pressure side of the fracture and are allowed to travel through the system with the probability of entering a particular flow section in the fracture proportional to the local flow rate. Also, when a particle comes to an intersection with two or three outgoing flow sections, a Monte Carlo method is used to assign the particle to one of the flow directions with probabilities weighted by their respective flow rates. As each of the particles travels through the fracture, the apertures it goes through are recorded. These build up the statistics of the aperture values of the channels. The results are shown as aperture density distribution functions in Figure 6. The dashed line gives the probability density distribution of apertures over the entire 2D plane of the fracture. The two solid lines give the aperture density distribution seen by the particles in the left-right and top-bottom flow directions respectively.

The tracer particles travel through large apertures and try to avoid small apertures of the 2D fracture aperture distribution. However, they cannot avoid the small apertures altogether and thus there is some finite probability of flow through apertures one or two orders of magnitudes smaller than the large apertures most particles travel through. Now, the aperture density distribution functions for left-right and for top-down tracer transport are found to be very similar. This is not obvious a priori, because the channels in the two cases represent quite different flow paths (Figures 4a and 4b). Thus we arrive at the interesting result that channels of tracer transport in the fracture system are characterized by the same aperture density distribution. We shall show how this information can be used in a later section.

The conclusion of the above study is that to understand tracer transport in such a highly heterogeneous system, we can consider transport channels which are characterized by an aperture probability distribution function, rather than specific (deterministic) flow paths.

Tracer breakthrough curves and the case for line (areal) or multi-point measurements

Using the particle tracking method, we can also calculate the tracer breakthrough curves. The time each particle takes to arrive at the low-pressure side of the single fracture is calculated by adding up the time it takes to traverse each step in the fracture (Moreno et al. 1988). The composite of the arrival times for all the particles forms the tracer breakthrough curves shown in Figure 7, which shows the percentage of particle arrivals versus time normalized by the mean arrival time of all the particles. In a tracer test, the vertical axis would be proportional to exit concentration. In this figure, seven curves are shown, representing three realizations of 2D fractures for $\lambda/L = 0.1$ and four for $\lambda/L = 0.4$. Thus this figure displays the sensitivity of the tracer breakthrough curves to two values of spatial correlation length, λ, and the different realizations that are statistically generated from the same input parameters, $\bar{b}$ and σ.

Figure 7 presents the dispersion of tracer particles through the fracture due to the large aperture variations. This dispersion acts in addition to the molecular diffusion and Taylor dispersion, which are set equal to zero in our calculation, and also in addition to dispersion due to matrix diffusion, surface sorption/desorption and other processes. The dispersion shown in this figure has two sources, one major and one minor. The minor source is tortuosity, which is the fact that the tracer particles travel by paths of different lengths. In our case, as in usual porous medium flow, the tortuosity effect results in path lengths that differ from the average by a factor approximately between 1 and 2. The major source causing the dispersion in these results is the strongly varying flow rates in

the flow channels, due to aperture constrictions along the particle flow paths. Such aperture constrictions cause flow rates to differ by orders of magnitude from each other.

It is of interest to note that all seven curves in Figure 7 fall within a small band. This shows that the results are not sensitive to the two different values of λ/L and to the different realizations used. We believe that this is due to the fact that we have considered tracer input and output along a line with a length equal to several spatial correlation lengths, thus averaging over strong local concentration variations of tracer emergence. Such large variations are to be expected based on the channeling character of tracer transport through the fracture system.

To illustrate the discussion we performed calculations for a number of realizations in which the same fluid flow field over the 2D fracture is used, but tracer particles are released only within a section length $s < L$ at a few high-flow locations along the high pressure side and collected at a few high-flow positions on the low pressure side. See Figure 8, for example. The collection length is assumed to be also s. Calculations were made for s/L = 0.1, 0.33 and 0.5.

Figure 9 shows tracer breakthrough curves for s/L = 0.1 for one of the realizations with $\lambda/L = 0.1$. Here tracers are released at two alternative locations, at A and B and collected at three alternative locations D, E and F (Figure 8). These locations are chosen because of their relatively large local flow rates. At each exit section, concentration, C, was calculated by dividing the accumulative exit particle number by the local flow rate. The maximum input concentration, C_0, is defined as the total number of tracer particles used in the calculation divided by the flow rate in the input section. The plot in Figure 9 is C/C_0 versus time of arrival, t, at the exit sections. Note that C/C_0 does not reach a value of 1 because of mixing of water from the tracer-injection section with the remainder of water inflow from high pressure side.

Several comments on the calculations need to be made. First, the exit flow rates at the three exit sections are quite different. They are given by Q = 26, 53, 37 units,

respectively. Second, the initial arrival times of the six possible tracer paths do not correlate with the linear distances between the tracer-injection section and the collection section. For example, the earliest arrival time corresponds to the case with linear transport distance of 1.04 L (tracer from B to E), and this is about half of the arrival time for a case with a slightly shorter linear transport distance of 1.005 L (tracer from B to F). Such non-correlation between initial arrival times and linear transport distances has often been observed in the field. A recent example may be found in the data from the Fanay-Augeres field tracer experiment (Cacas et al. 1988).

A measure for the dispersion displayed in Figure 9 may be defined as $(t_{0.9} - t_{0.1})$ / $t_{0.5}$ where t_x is the time of arrival when the concentration reaches a fraction x of the maximum concentration value reached at large times. This empirical definition of dispersion has the advantage that it is independent of a model for the system. For the particular case of the porous medium model, this definition has been shown to relate to the dispersivity through the Peclet number (Neretnieks, 1983).

Let us take the cases shown in Figure 9, and calculate the value of the dispersion measure as defined above for each case. The results obtained are spread out over a factor of 3 from each other (see Figure 10 for s = 0.1 L). However, if we carry out the same exercise with the tracer collection section length increased from s = 0.1 to 0.33 and to 0.50, the spread of the dispersion measure is greatly reduced. This is shown in Figure 10. Recall that in this case the spatial correlation length is $\lambda/L = 0.1$.

The above calculations suggest that line measurements with line section lengths corresponding to a few correlation lengths may yield more stable values for the dispersion measure, which may then be studied for its dependence on the basic parameters $\bar{b}$ and σ.

Interpretation of 2D transport in terms of a Channel Model

In an earlier section we showed that the transport of tracer particles through a 2D fracture of strongly varying apertures takes place in variable-aperture channels (in the sense of stream-tubes in the potential theory), which are characterized by an aperture probability distribution function with parameters $\bar{b}$ and σ.

In this section we shall demonstrate how a group of one-dimensional channels with apertures obeying the aperture probability distribution function can reproduce the detailed two-dimensional results. In Figure 6, we show that the apertures seen by tracer particles as they travel under a pressure difference through the 2D fracture obey an aperture distribution function shown by the solid line. Let us start with this aperture distribution function and construct 1D variable-aperture channels statistically (Tsang and Tsang, 1987; Tsang et al. 1988). A system of 40 1D channels were generated and they are interpreted as 40 possible flow paths taken by the tracer particles traveling through the 2D fracture. The choice of 40 as the number of 1D channels is somewhat arbitrary, though it should be large enough to produce a smooth tracer breakthrough curve on the exit side of the fracture. A pressure difference is applied across these 1D channels, each of which will carry a different flow rate with a different travel time for the tracer particles. The tracer breakthrough curve is obtained by accounting for arriving particles from this system of 1D channels. 40 realizations of this system of 40 1D channels were generated and for each, the tracer breakthrough curve was calculated. The results are shown in Figure 11, where the mean of the 40 breakthrough curves for the 40 realizations is shown as the long-dash broken curve, with the limit of the spread of the 40 curves indicated by a horizontal bar. The solid curve in the figure is the result of the detailed 2D tracer transport calculations (Figure 7) with the horizontal bar indicating the limit of the spread of calculated values for eight realizations.

We also took the same initial aperture density distribution and constructed a system of constant-aperture channels and computed the breakthrough curves. These are

channels, each of which have a constant aperture, but with values different from each other. (This can be interpreted as the so-called perfectly stratified reservoir model). The results are shown as the short-dashed broken curve in Figure 11. Finally, if the entire fracture is a parallel plate with only one constant aperture, then the result would be a step with concentration 0 for $t/t_m < 1$ and 100% for $t/t_m \geq 1$, implying a piston flow with zero dispersion. The results for the tracer breakthrough through such a parallel plate representation of a single fracture are shown as the dot and dash curve in the figure. The better fit of the 1D Channel Model to the detailed 2D results is apparent in this figure.

Figure 11 is plotted with time on the horizontal axis normalized to the mean residence time t_m in order to compare the dispersion predicted from the different models. The actual values of mean residence time from the different models are presented in Table 1. The second column gives the expected values obtained by dividing total fracture volumes by the calculated total flow rates in two dimensions. The third column gives the mean particle residence times from the breakthrough curves derived from particle tracking in two dimensions. These agree within a few percent of the values in column 2. The fourth column gives the mean residence times from the breakthrough curves derived from the one-dimensional variable-aperture channel model. We note that the mean residence times are within a factor of two as those derived from the actual two-dimensional transport. The last column gives the mean residence times obtained from the breakthrough curves derived from a system of constant aperture channels. The mean residence times in this last column are typically two to three orders of magnitude smaller than those predicted from both the two-dimensional and one-dimensional variable-aperture channel calculations. This is easy to understand since in the constant-aperture channel representation, the larger the aperture, the shorter the residence time, therefore the average is heavily weighted by the residence times of the largest constant aperture channels.

The qualitative agreement between the results from one-dimensional variable-aperture channel model and the two-dimensional calculations shown in both Figure 11 and Table 1 is good. This implies that as far as tracer transport is concerned, break-through curves for a 2D fracture with variable apertures can be obtained by a model of 1D variable-aperture channels, which are characterized by an aperture probability distribution function, with just two parameters, b and σ.

Summary and Conclusions

Tracer transport through fractured rocks should no longer be envisioned as transport through a system of interconnecting parallel-plate fractures. The strongly varying apertures of these fractures result in preferred paths of fluid and tracer flow in the fractures. These have been observed in field and laboratory experiments, and are referred to as channels. Thus channels defined this way are not rigidly set pathways for tracer transport, but are the preferred flow paths in the sense of stream-tubes in the potential theory. These channels are present in addition to physical or structural channels along lines of high permeability, such as those occurring at the fracture intersections.

It is shown in this paper that such variable-aperture channels can be characterized by an aperture probability distribution function with parameters b and σ, and not by the exact deterministic geometric locations. We demonstrated that the 2D tracer transport in a fracture can be calculated by a model of a system of 1D channels characterized by this distribution function only. In general, transport through multiple fractures may also be calculated by a model of a system of 1D channels characterized by an aperture distribution function, which is built up of apertures from all the fractures.

Due to the channeling character of tracer transport in fractured rock, random point measurements of tracer breakthrough curves may give results with a wide spread in value due to statistical fluctuations. The present paper suggests that such wide spread can probably be greatly reduced by making line/areal (or multiple) measurements covering a

few spatial correlation lengths. We believe much work remains to be done along this line both by theoretical studies and by numerical experiments.

Acknowledgements

References

Abelin, H., Bergersson, Gidlund, J., Moreno, L., Neretnieks, I., Widen, H., and Andersson, J., Results of some large scale in situ tracer experiments in a drift at the Stripa Mine, Proceedings of International Conference on Fluid Flow in Fractured Rocks, Atlanta, Georgia, May 16-18, 1988.

Abelin, H., Gidlund, J. and Neretnieks, I., Migration in a single fissure. *Scientific Basis for Nuclear Waste Management* V, p. 529, 1982. North Holland Elsevier Science Publishers, New York.

Bourke, P. J., Channeling of flow through fractures in rock, Proceedings of GEOVAL-87, International Symposium, Stockholm, Sweden, April 7-9, 1987.

Cacas, M. C., Ledoux, E., and de Marsily G., Calibration and validation of a three-dimensional stochastic network model on a large scale experiment with flow measurements and tracer tests performed in the uranium mine of Fanay-Augeres, Proceedings of International Conference on Fluid Flow in Fractured Rocks, Atlanta, Georgia, May 16-18, 1988.

Gale, J.E., Characterizing the geometry of fracture systems for flow and transport studies in fractured rock masses, Proceedings of International Conference on Fluid Flow in Fractured Rocks, Atlanta, Georgia, May 15-18, 1988.

Gentier, S., Morphologie et comportement hydromecanique d'une fracture naturelle dans un granite sous contrainte normale, Doctoral Thesis, U. d'Orleans, France, 1986.

Moreno, L., Tsang, Y. W., Tsang, C. F., Hale, F. V., and Neretnieks, I., Flow and tracer transport in a single fracture: A stochastic model and its relation to some field observations, LBL-25049, accepted for publication in *Water Resources Research,* 1988.

Neretnieks, I., A note on fracture flow dispersion mechanisms in the ground, *Water Resources Research,* 19 (2), 364-370, 1983.

Neretnieks, I., Transport in fractured rocks, Proceedings, Memoires of the 17th International Congress of International Association of Hydrologists, Vol. XVII, 301-318, International Association of Hydrologists, Tucson, Arizona, 1985.

Smith, L. and Schwartz, F. W., Mass transport, 1: A stochastic analysis of macroscopic dispersion, *Water Resources Research,* 16 (2), pp. 303-313, 1980.

Tsang, Y.W., The effect of tortuosity of fluid flow through a single fracture, *Water Resources Research,* 20 (9), pp. 1209-1215, 1984.

Tsang, Y. W., and Tsang, C. F., Channel model of flow through fractured media, *Water Resources Research,* 23 (3), 467-479, 1987.

Tsang, Y. W., Tsang, C. F., Neretnieks, I., and Moreno, L., Flow and tracer transport in fractured media — A variable-aperture channel model and its properties, LBL-25048, accepted for publication in *Water Resources Research,* 1988.

Table 1   Mean residence times for a number of runs or realizations, calculated from
           (a) 2D fracture volume divided by total calculated flow rate, (b) mean par-
           ticle travel time from 2D calculation, (c) mean travel time from a system
           of 1D variable-aperture channels, and (d) mean travel time from a system
           of constant-aperture channels.

| Run	Mean Residence Time (arbitrary units)			
	Fracture Volume / 2-D Flow Rate	2-D Particle Tracking	Variable-Aperture 1-D Channels	Constant-Aperture 1-D Channels
511	0.59	0.59	0.82	0.004
512	1.46	1.49	1.64	0.012
513	0.35	0.34	0.39	0.007
514	0.33	0.33	0.41	0.006
541	0.07	0.07	0.06	0.0005
542	2.29	2.30	3.10	0.007
543	0.86	0.85	1.15	0.0047
544	0.30	0.30	0.35	0.003

- 94 -
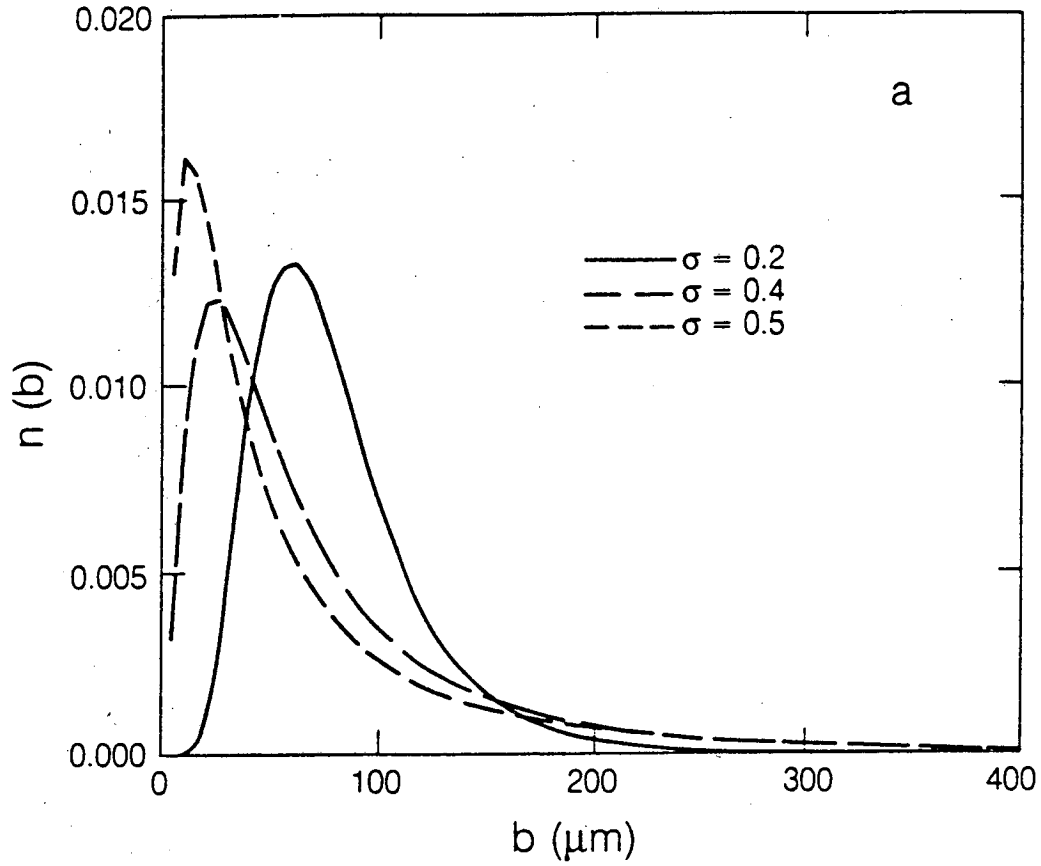
XBL 879-10373

Figure 1   Lognormal distributions with $\bar{b}$ = 80 μm and σ = 0.2, 0.4 and 0.5, plotted on a linear scale.
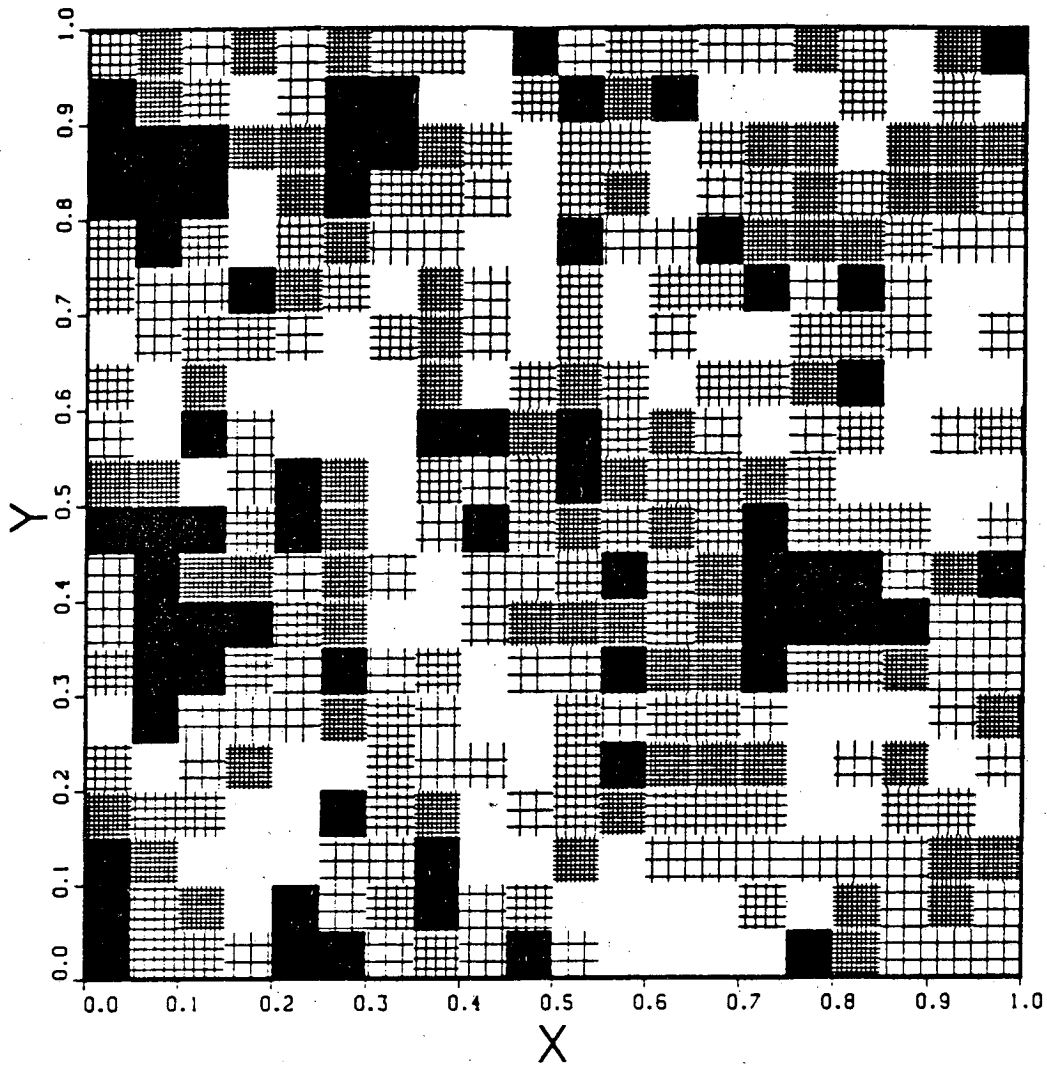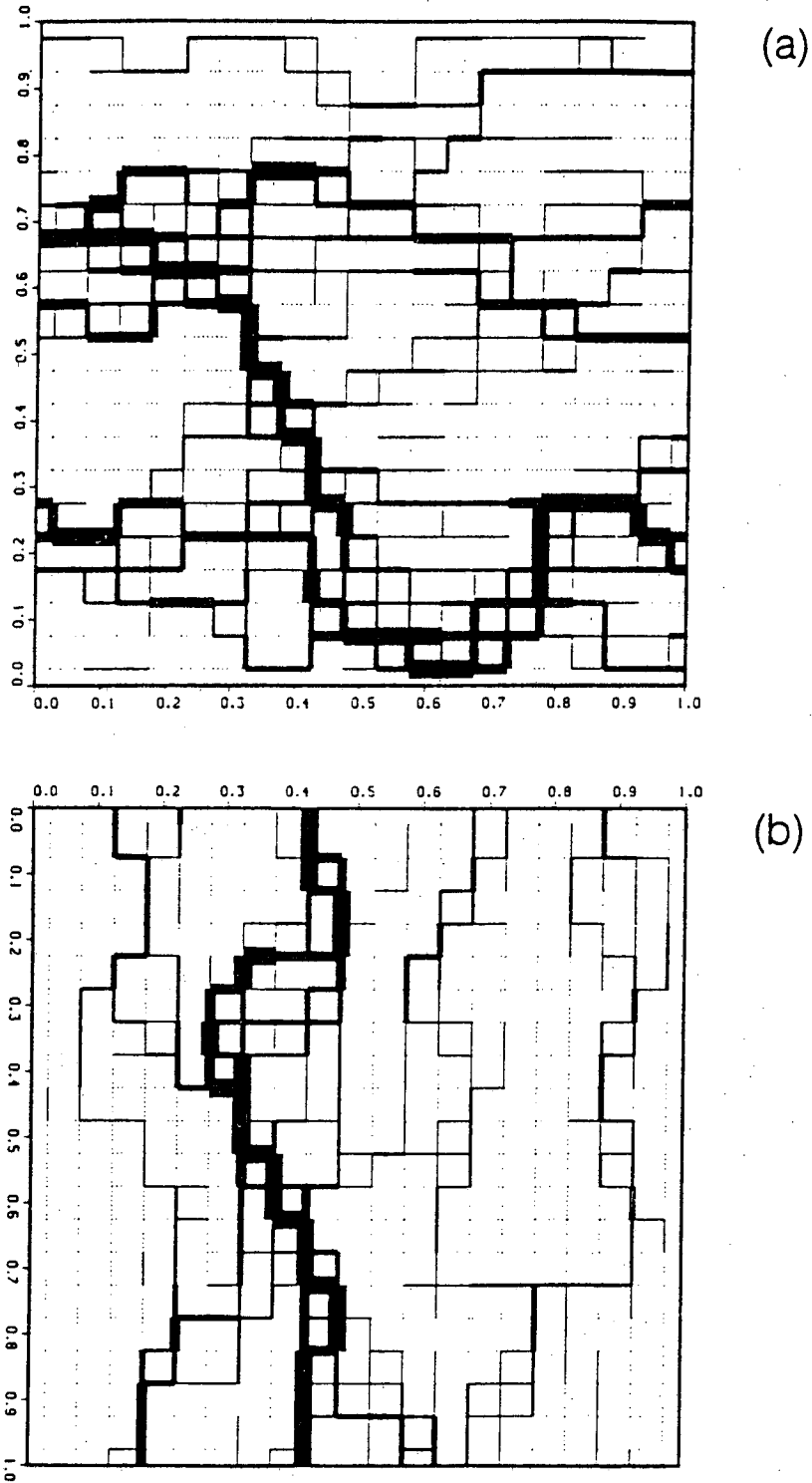
XBL 887-10344

Figure 2   Statistically generated apertures with a spatial correlation length λ of 0.1L in the plane of a single fracture of linear dimension L. The shadings are given in five levels from small apertures (dark) to large ones (white). The dividing values correspond to the logarithm of apertures given by 1.33, 1.59, 1.81, 2.07, with apertures in μm.

$$R_{ij} = 6\mu \, \frac{\Delta x}{\Delta y} \left[\frac{1}{b_i^3} + \frac{1}{b_j^3} \right]$$
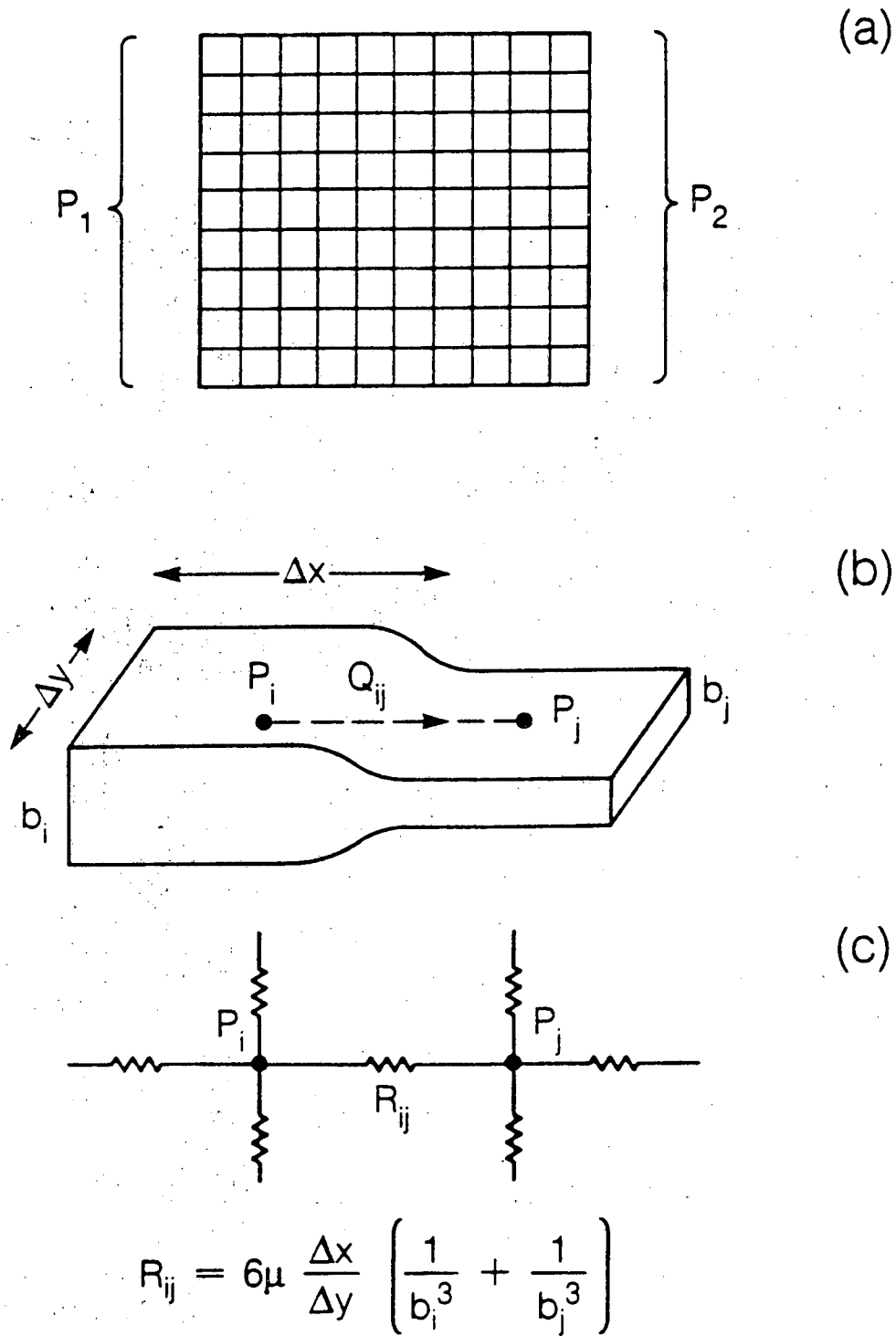
XBL 873-10019

Figure 3   (a) Schematic diagram for flow through a single fracture with different aperture values assigned to areas bounded by grid lines.
(b) Schematic diagram for two adjacent elements of different apertures, b_i and b_j and the fluid flow Q_{ij}, between them.
(c) Resistance to fluid, R_{ij}, in an electric analog, in terms of apertures, dimensions of the elements and fluid viscosity μ.
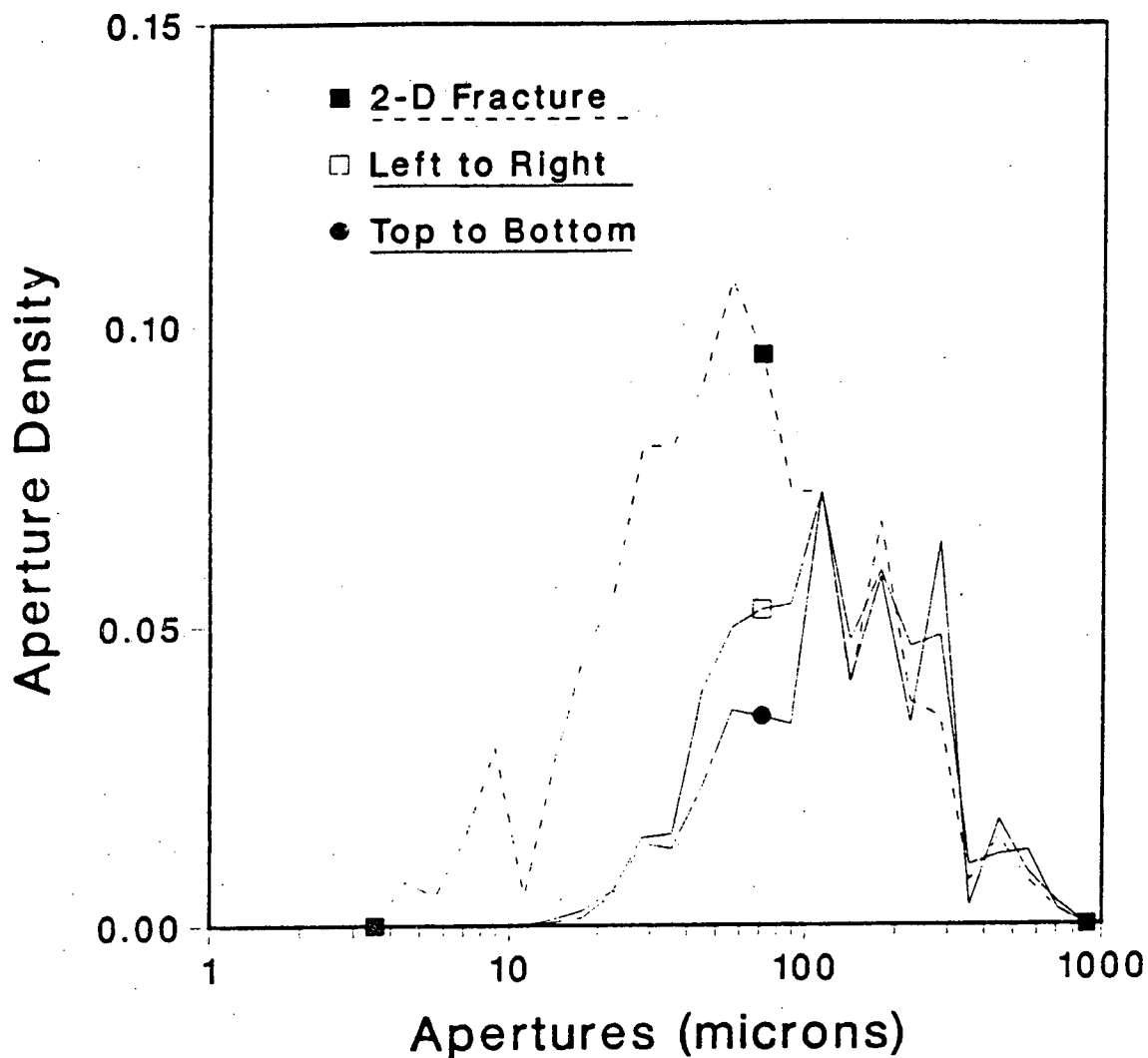
XBL 887-10345

Figure 4   (a) Fluid flow rates for the fracture with aperture variations as shown in
figure 2. The thickness of the lines is proportional to the square root of
the flowrates. Pressure difference is applied from left to right. (b) Same
as (a), but with pressure difference applied from top to bottom.

Left to Right (a)

Top to Bottom (b)
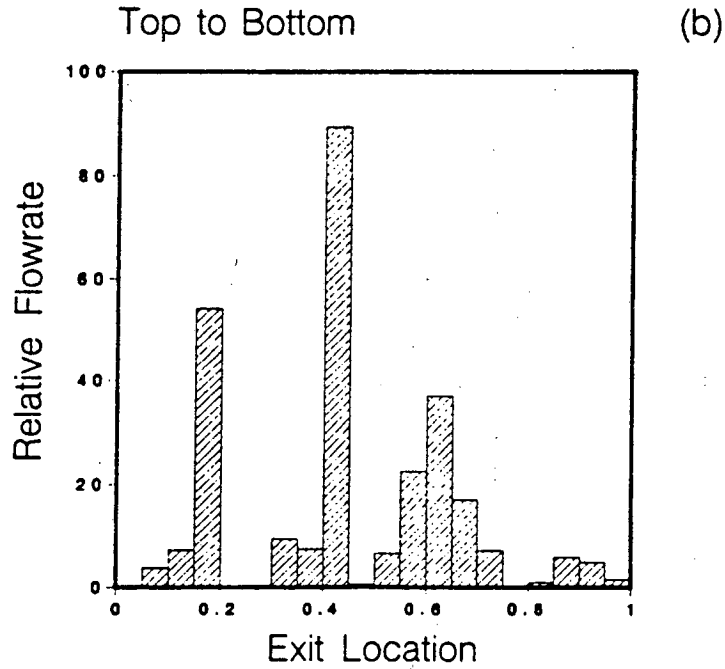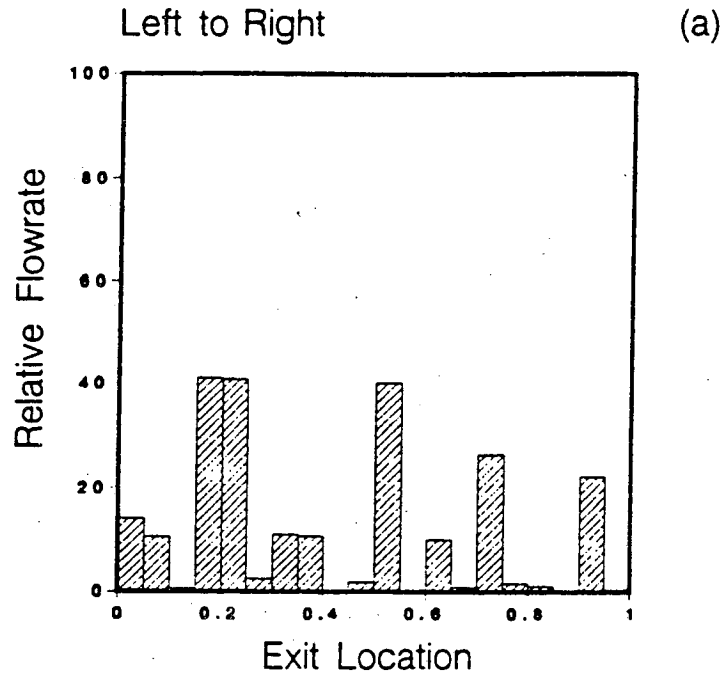
XBL 887-10346

Figure 5   Histograms of flow rates along the exit line corresponding to Figures 4a and 4b respectively.

Figure 6   The aperture probability density distribution for (a) apertures over the entire 2D fracture plane corresponding to Figure 2; (b) apertures along particle flowpaths with left-right pressure difference; and (c) apertures along particle flowpaths with top-bottom pressure difference.
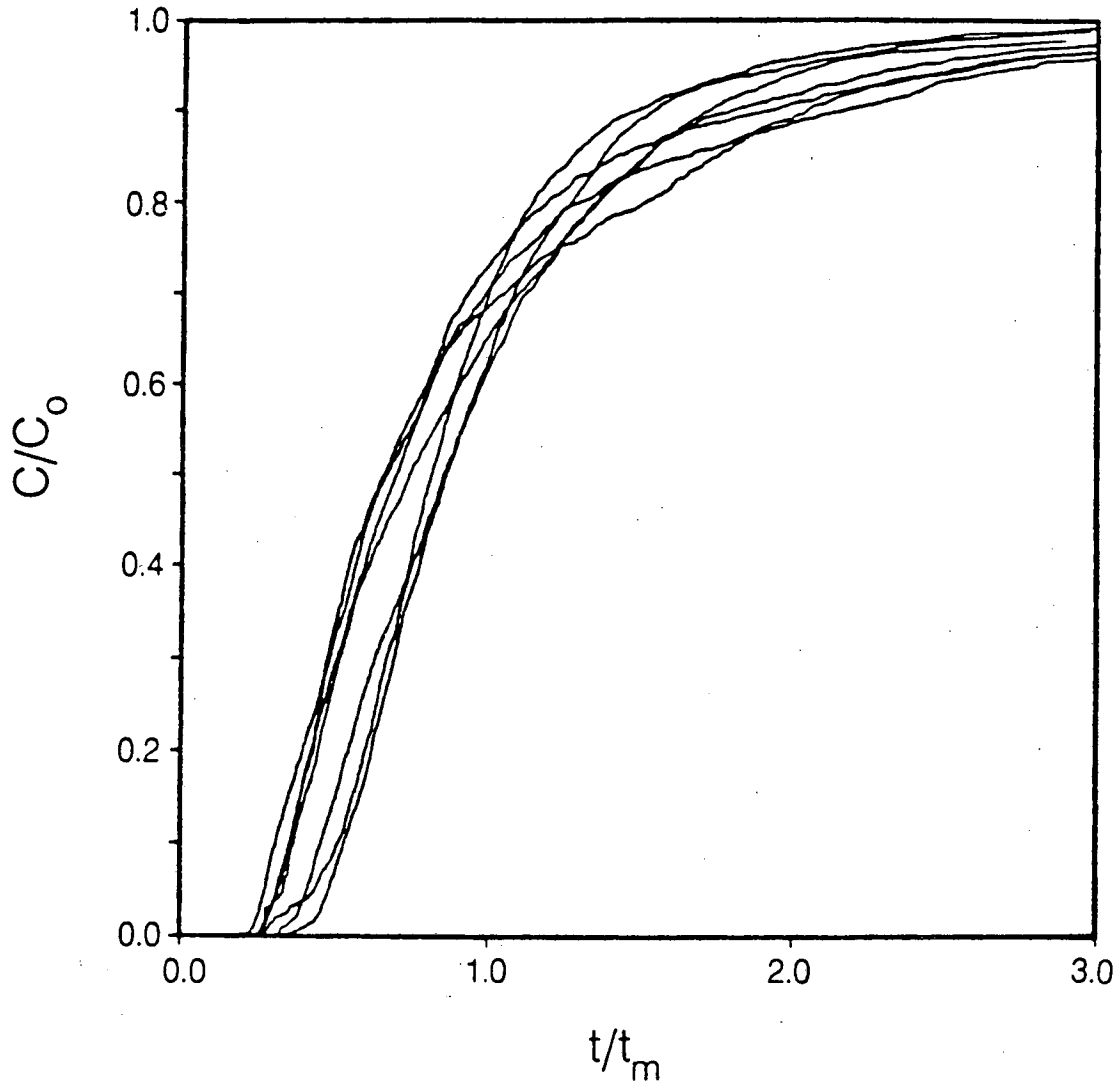
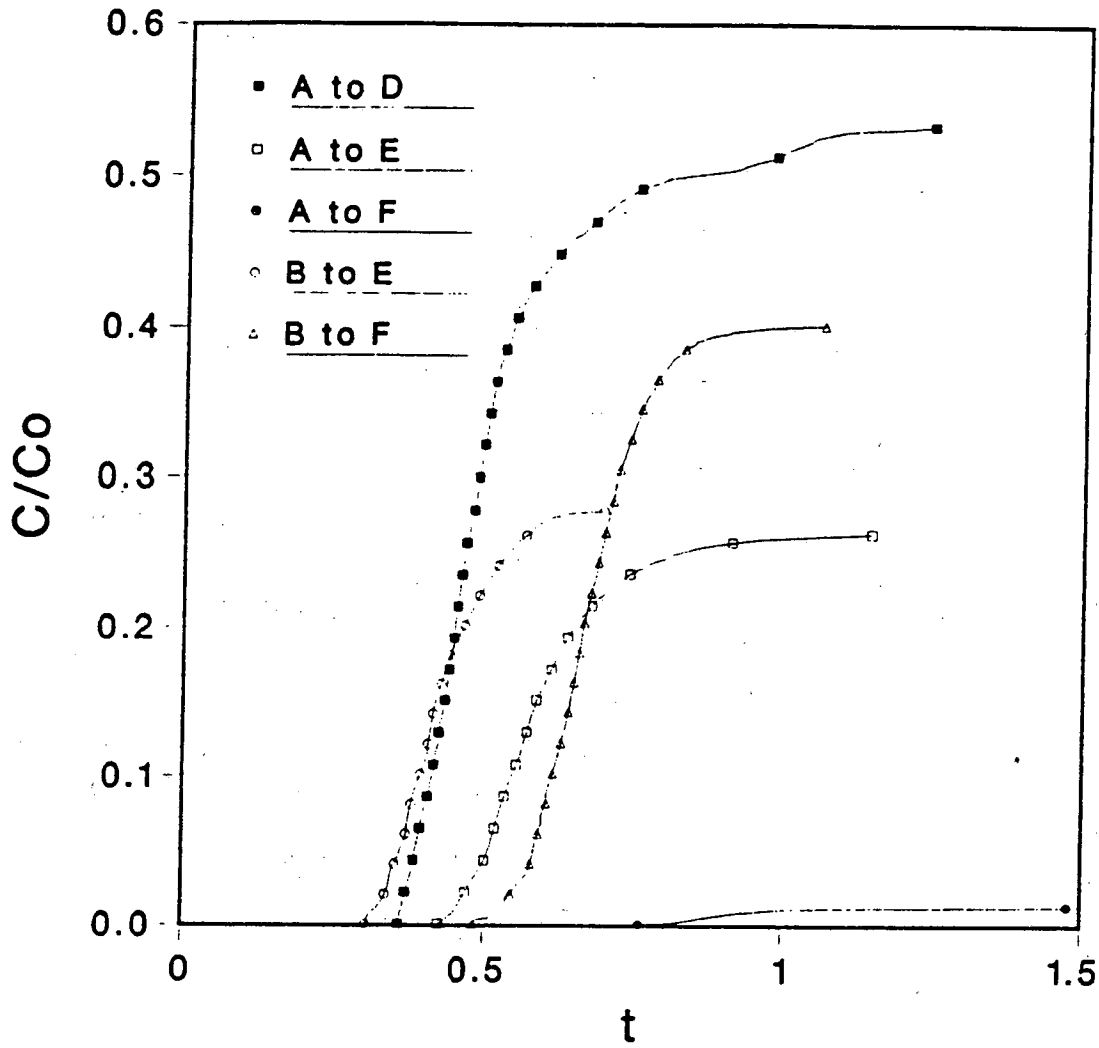XBL 887-10349

Figure 7   Tracer breakthrough curves from particle tracking with time normalized to the mean residence time, t_m, of all the particles. Seven realizations of the generated fracture aperture distributions are used, including the case shown in Figure 2. Among the seven, four has $\lambda = 0.1L$ and three has $\lambda = 0.4L$. All curves fall within a narrow band of each other.
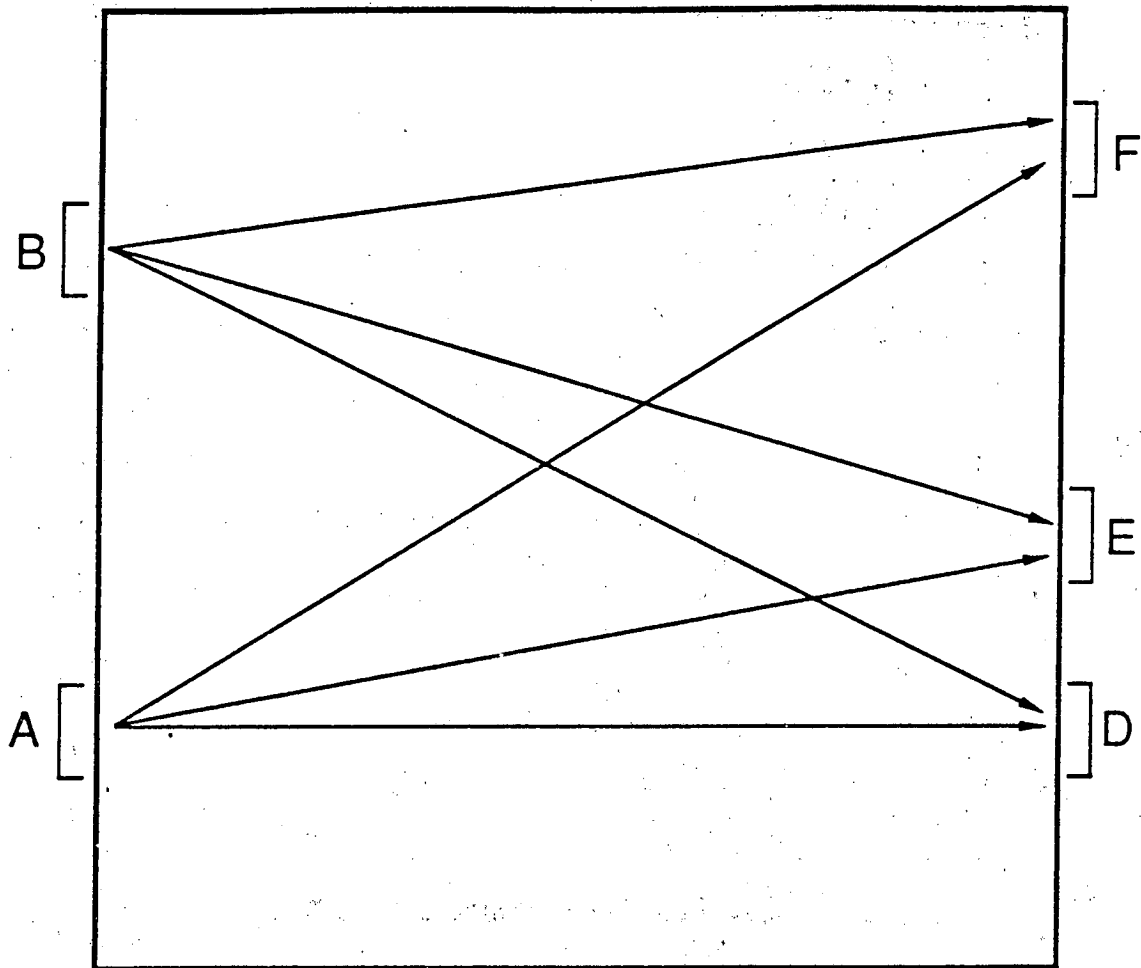
XBL 887-10330

Figure 8   Schematic diagram illustrating "point" measurements of tracer transport. Based on one of the realizations of a fracture with variable apertures with an applied left-right pressure difference, tracers are deposited at A and B and collected at D, E, and F. Points A, B, D, E and F are chosen at locations of large entrance or exit flow rates and each is associated with a section length of 0.1L.

XBL 887-10348

Figure 9   Tracer breakthrough curves for cases shown in Figure 8, with the section length for tracer entrance or exit equal to 0.1L.
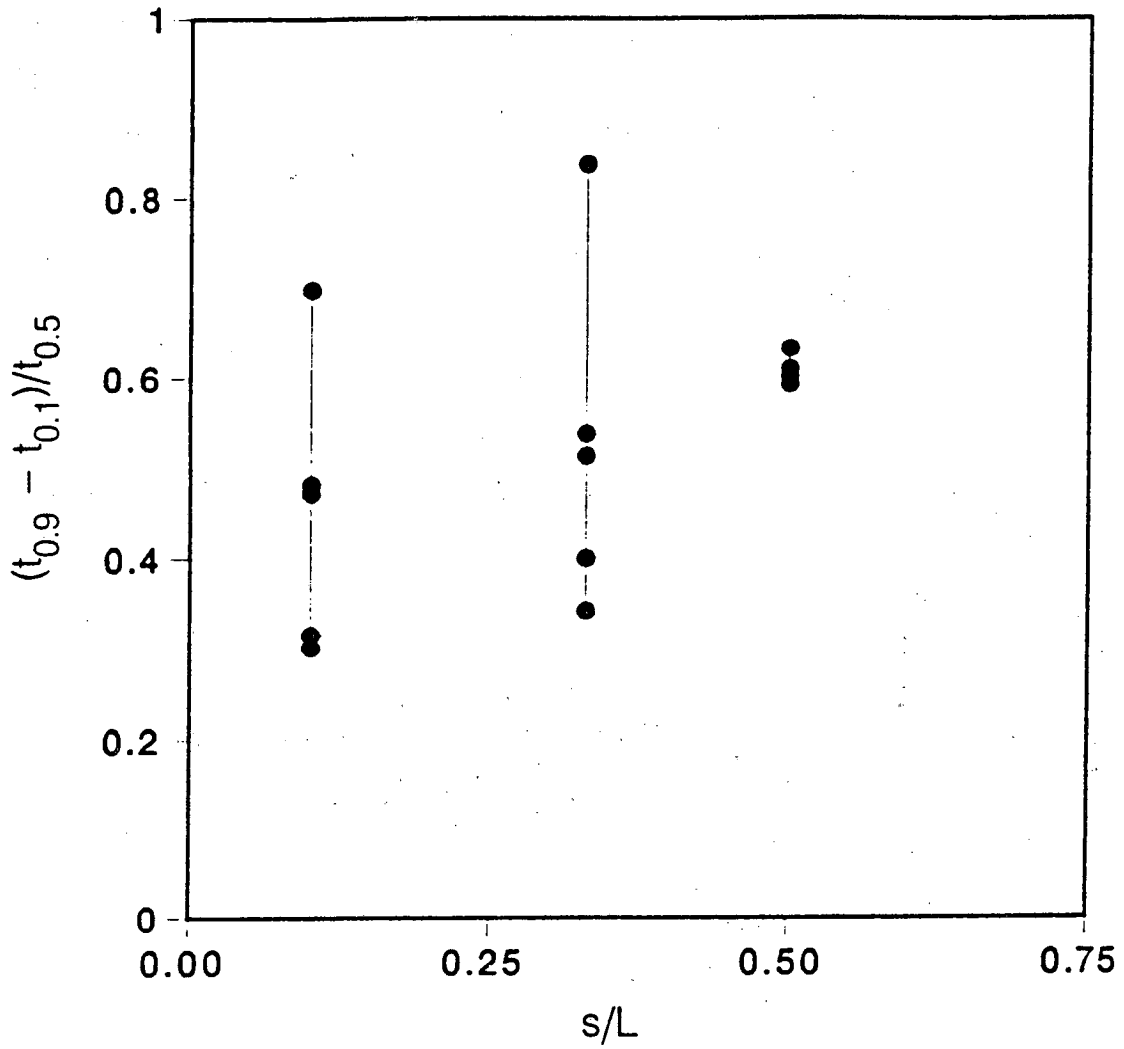
XBL 887-10350

Figure 10   The tracer dispersion measure, $(t_{0.9} - t_{0.1}) / t_{0.5}$, as a function of the section length for tracer entrance or exit.
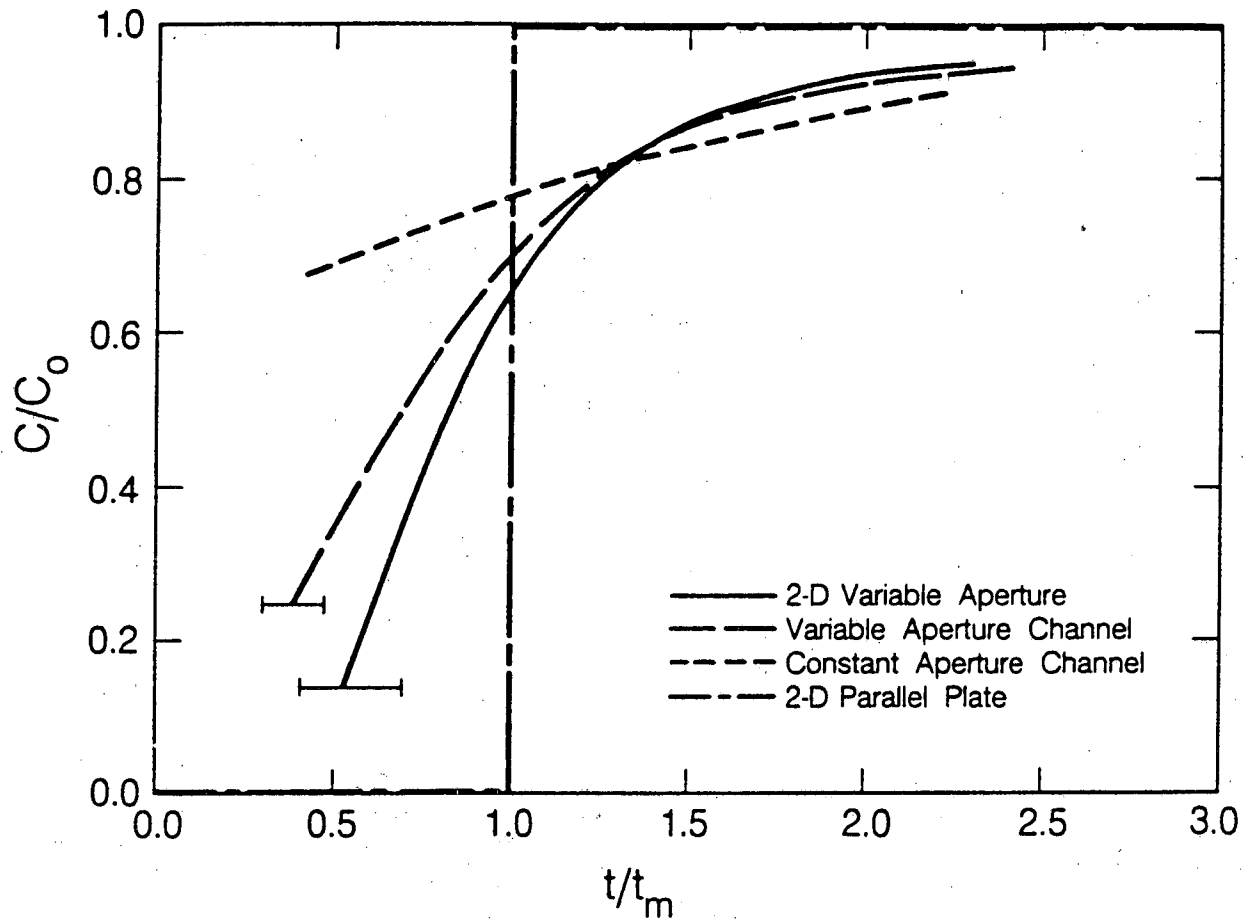
XBL 879-10383

Figure 11   Tracer breakthrough curves from (a) 2D calculation, (b) 1D variable-aperture channel calculation, (c) constant-aperture channel calculation, and (d) parallel-plate fracture calculation. Horizontal bars give the limits of values from seven realizations each for cases (a) and (b).

Hydrologic Characterization of Faults and Other

Potentially Conductive Features

Iraj Javandel and Chao Shan

Introduction

The capability of locating and characterizing near-vertical faults and other potentially high conducting geologic features in the region close to a high-level-waste repository site is one of the most important tasks in the site characterization of underground waste isolation projects. Existence of such features in the vicinity of the repository site could provide a pathway with short travel time from the disturbed zone to the accessible environment (or the water table in case of Nevada site).

The faults may cut through various geologic formations both in saturated and unsaturated zones. Depending on the properties of local geologic materials, the amount of relative displacement of layers, and the state of stress, a fault could provide a conductive pathway or be practically sealed. In terms of their hydrologic response on field pumping tests faults may be classified as follows: (1) tight faults, (2) constant head faults, and (3) non-constant head leaky faults (Witherspoon et al. 1967).

Tight faults are those that cut through the aquifers and for all practical purposes hydraulically disconnect one part of the aquifer from the rest of it and from other water bearing formations above and below.

Constant head faults are those that connect the aquifer to a large constant head water body and the path along the fault between the aquifer and the water body has practically infinite permeability.

Mathematically tight and constant head faults may be represented by no flow and constant head boundary conditions, respectively. Several other types of geologic configurations may also be responsible for such no flow or constant head boundaries in a pumping aquifer, as discussed by Ferris (1949).

Adapting method of images used in 19th century heat and electicity studies, Ferris (1949) and Jacob (1950) proposed a method for calculating values of drawdown in a pumping aquifer that is intersected by tight or constant head faults. Furthermore, Ferris (1949) presented a method for finding the location of such boundaries by monitoring drawdowns due to a constant discharging well in at least two observation wells.

In real life, however, there are some discontinuities in rock masses that have finite but higher conductivities than the surrounding rock matrix. Unlike tight or constant head faults that represent two ends of the permeability scale, i.e. zero and infinity, these discontinuities may present potential flow paths with relatively large but finite transmissivity.

The goal of this work is to develop hydrologic tests and analysis methods to locate and characterize faults and potentially conducting features close to a candidate repository site. This report presents an analytic solution for calculating drawdowns in a pumping aquifer that has been intersected by a finite transmissivity fault or other similar permeable geologic features. Based on this solution, a method is presented that enables one to locate such linear features and estimate their hydraulic properties.

Theory

Let us consider an extensive 2-D homogeneous isotropic aquifer that has been intersected by a fault of finite conductivity (Fig. 1). A fully penetrating well located at a distance " a " from the fault is being pumped at a constant rate of Q. The fault divides the aquifer into two regions. The part of the aquifer on the pumping side is designated by region I and the other side by region II. If drawdown at the point (x,y)

in the aquifer and time t is represented by $s_i(x,y,t)$, i=1,2, then mathematically the problem can be formulated by the following governing differential equations and boundary conditions.

$$\frac{\partial s_1}{\partial t} = \alpha \left\{ \frac{\partial^2 s_1}{\partial x^2} + \frac{\partial^2 s_1}{\partial y^2} \right\} + \frac{\alpha Q}{KH} \delta(x-a) \tag{1}$$

$$\frac{\partial s_2}{\partial t} = \alpha \left\{ \frac{\partial^2 s_2}{\partial x^2} + \frac{\partial^2 s_2}{\partial y^2} \right\} \tag{2}$$

$$s_1(x,y,0) = s_2(x,y,0) = 0 \tag{3}$$

$$s_1(\infty,y,t) = 0 \tag{4}$$

$$s_2(-\infty,y,t) = 0 \tag{5}$$

$$s_1(x,\pm\infty,t) = s_2(x,\pm\infty,t) = 0 \tag{6}$$

$$s_1(0,y,t) = s_2(0,y,t) \tag{7}$$

$$K H \frac{\partial s_1}{\partial x} = K H \frac{\partial s_2}{\partial x} + K' s_2 \qquad \text{at } x = 0 \tag{8}$$

where $\delta(x)$ is Dirac delta function, α and K are diffusivity and hydraulic conductivity of the aquifer respectively and Kprim is a measure of fault's conductivity. Note that the condition at the fault, expressed by (8), indicates that influx into region I is the sum of flux from region II and flux from the fault which is proportional to the drawdown in the aquifer along the fault. It is important to note that drawdown in the aquifer along the fault is a function of both time and position. Equation (8) implies that (1) storativity of the fault is negligible and (2) the fault is connected to a constant source above or below the aquifer.

Using the Laplace and Fourier transform consecutively, a solution to the above mathematical model has been derived as given below.

$$s_1 = -\frac{Q}{4\pi KH}Ei\left\{-\frac{(x-a)^2+y^2}{4\alpha t}\right\} - \frac{Qc\sqrt{\alpha}\,\exp[c(x+a)]}{4\sqrt{\pi}KH}\int_0^t g_1(\tau)d\tau \qquad (9)$$

$$s_2 = -\frac{Q}{4\pi KH}Ei\left\{-\frac{(x-a)^2+y^2}{4\alpha t}\right\} - \frac{Qc\sqrt{\alpha}\,\exp[c(a-x)]}{4\sqrt{\pi}KH}\int_0^t g_2(\tau)d\tau \qquad (10)$$

where

$$g_1(\tau) = \frac{\exp[c^2\alpha\tau-\frac{y^2}{4\alpha\tau}]}{\sqrt{\tau}}erfc\left\{\frac{x+a}{2\sqrt{\alpha\tau}}+c\sqrt{\alpha\tau}\right\} \qquad (11)$$

$$g_2(\tau) = \frac{\exp[c^2\alpha\tau-\frac{y^2}{4\alpha\tau}]}{\sqrt{\tau}}erfc\left\{\frac{a-x}{2\sqrt{\alpha\tau}}+c\sqrt{\alpha\tau}\right\} \qquad (12)$$

and

$$c = \frac{K'}{2KH} \qquad (13)$$

Recalling that s_1 and s_2 refer to drawdowns in region I and II where values of x are positive and negative, respectively, a unified solution for the whole aquifer is given by:

$$s = -\frac{Q}{4\pi KH}Ei\left\{-\frac{(x-a)^2+y^2}{4\alpha t}\right\} - \frac{Qc\sqrt{\alpha}\,\exp[c(a+|x|)]}{4\sqrt{\pi}KH}\int_0^t g(\tau)d\tau \qquad (14)$$

where

$$g(\tau) = \frac{\exp[c^2\alpha\tau-\frac{y^2}{4\alpha\tau}]}{\sqrt{\tau}}\,erfc\left\{\frac{a+|x|}{2\sqrt{\alpha\tau}}+c\sqrt{\alpha\tau}\right\} \qquad (15)$$

The right hand side of (14) consists of two parts. Part one, the exponential integral, stands for the drawdown due to a pumping well in an infinite aquifer (Theis solution), and part two represents the buildup due to the leakage from the fault. Note that part two vanishes when conductivity of the fault , K' , goes to zero.

Fault recharge rate

The overall recharge rate from the fault into the aquifer may be obtained by integrating flux along the y-axis from $-\infty$ to $+\infty$. The result of the above integration gives the following expression for the total recharge rate from the fault.

$$Q_f(t) = Q \left\{ erfc[\frac{a}{2\sqrt{\alpha t}}] - exp[ca + c^2\alpha t] \; erfc[\frac{a}{2\sqrt{\alpha t}} + c\sqrt{\alpha t}] \right\} \qquad (16)$$

It can be shown that: (1) Q_f vanishes when conductivity of the fault, K', and as a result c goes to zero, and (2) when $c \neq 0$, recharge rate from the fault, Q_f, approaches the pumping rate at large times.

Discussion and results

Introducing the following dimensionless parameters

$$s_D = \frac{4\pi KHs}{Q} \qquad t_D = \frac{\alpha t}{r^2} \qquad a_D = \frac{a}{r} \qquad c_D = c \cdot r$$

where r is the distance between the pumping and the observation wells, one can prepare families of type curves presenting dimensionless drawdowns versus dimensionless time for various running parameters. Figure 2 presents a sample of these type curves on a log-log paper, and Figure 3 shows the results on a semilogarithmic paper.

One may note that the shape of these curves are very similar to the type curves for the leaky aquifers (r/B solutions). The question may then be raised that how could one differentiate these two different effects from the results of the pumping tests.

The drawdown pattern observed in two monitoring wells located at the same distance from the pumping well in a leaky aquifer are identical. This is because the value of r/B for both wells are the same. However, drawdowns in the same two monitoring wells under the influence of a leaky fault are easily differentiable and that is because monitoring wells are located at different distances from the fault. Therefore, a proper design of the pumping test is the key for the correct interpretation of the data.

Figure 4 illustrates the variation of the fault recharge rate with time. It shows the change of dimensionless recharge rate, Q_f/Q, as a function of dimensionless time for four values of c_D. As discussed above, one may note that the fault recharge rate tends to increase with time, and if the pumping continues for relatively large periods of time, most of the water extracted from the aquifer is essentially supplied by the fault. Obviously at any given time the percentage of the extracred water coming from the fault is a function of c_D, that in turn is a function of conductivity of the fault and its distance from the pumping and observation wells.

Using the above results a method has been developed to estimate the conductivity of the leaky fault. Studies have been carried out to identify the sensitivity of the results to different parameters and the limitation of the proposed technique. Details of these studies will appear in a more comprehensive report.

References

Ferris, J. G., Ground Water, in Hydrology, by C. O. Wisler and E. F. Brater, John Wiley and Sons, New York, pp. 198-272, 1949.

Jacob, C. E., Flow of ground water, in Engineering Hydraulics, edited by H. Rouse, John Wiley and Sons, New York, pp. 321-386, 1950.

Witherspoon, P. A., I. Javandel, S. P. Neuman, and R. A. Freeze, Interpretation of Aquifer Gas Storage Conditions from Water Pumping Tests, American Gas Assoc., 273 p., 1967.
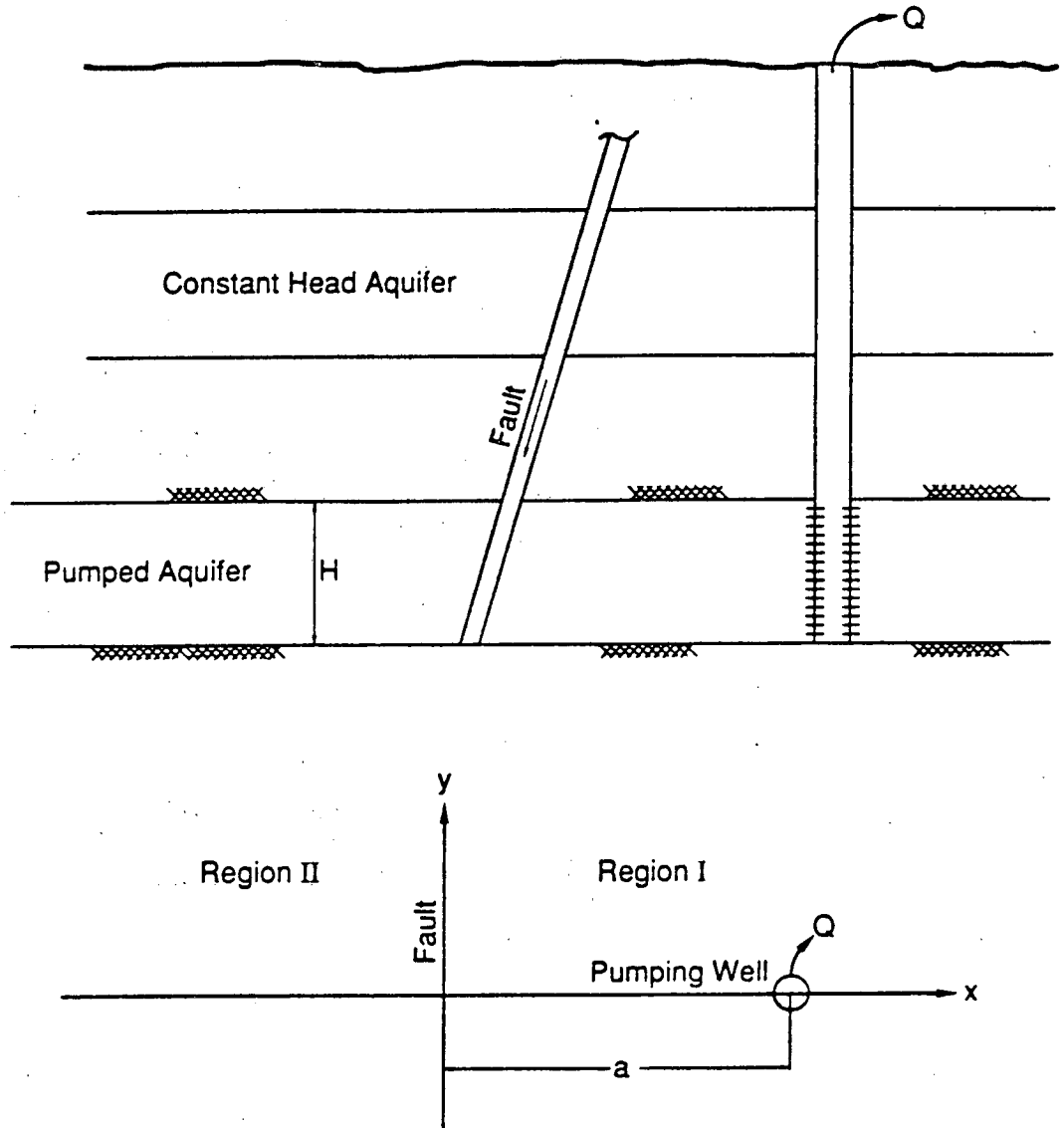
Figure 1.   A schematic section and plan of the aquifer intersected by a leaky fault.
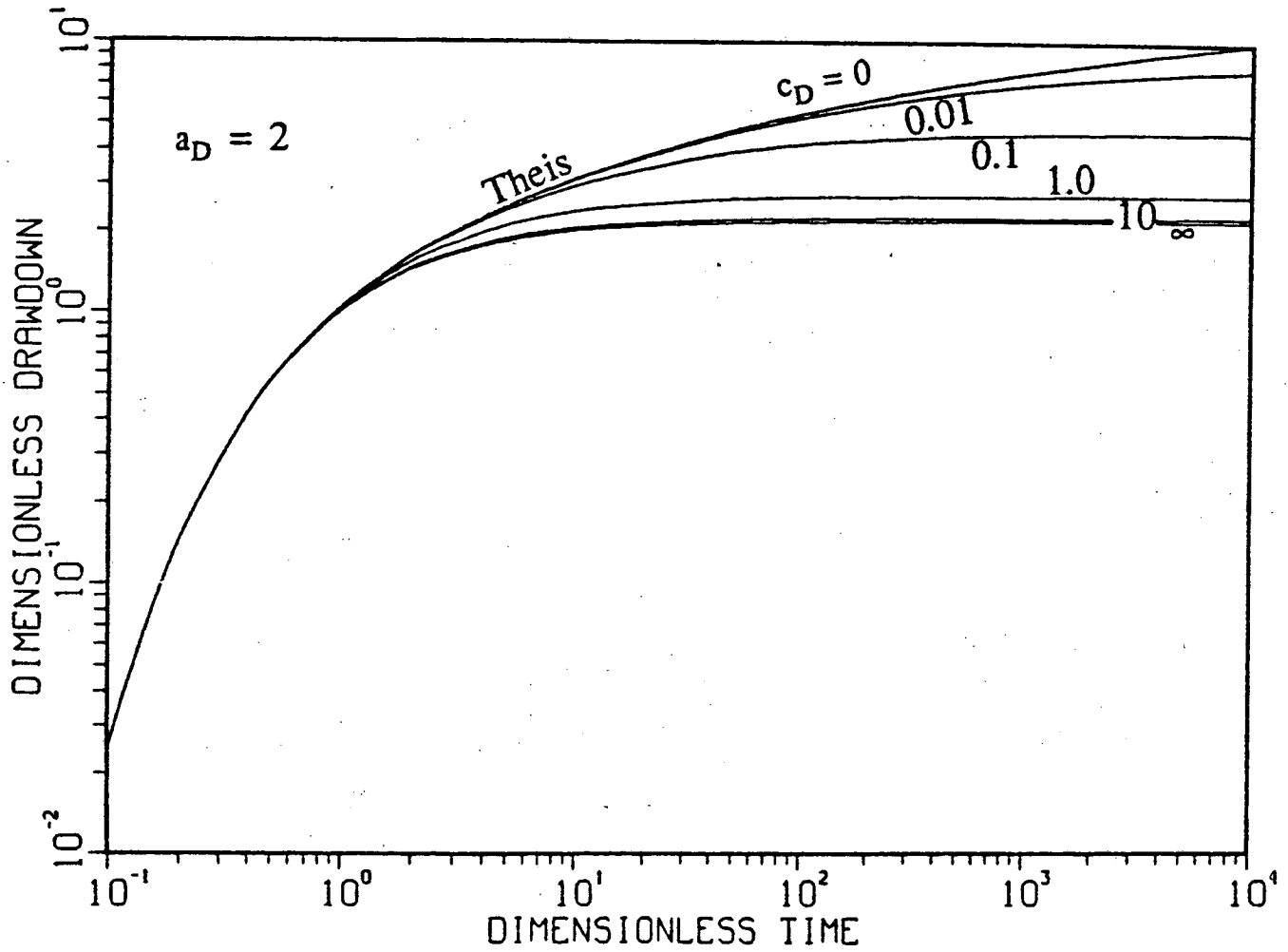
XBL 8811-10519

XBL 8811-10520

Figure 2.   Log-log plots of dimensionless drawdown versus dimensionless time for $a_D = 2$ and c_D ranging from 0 to ∞.
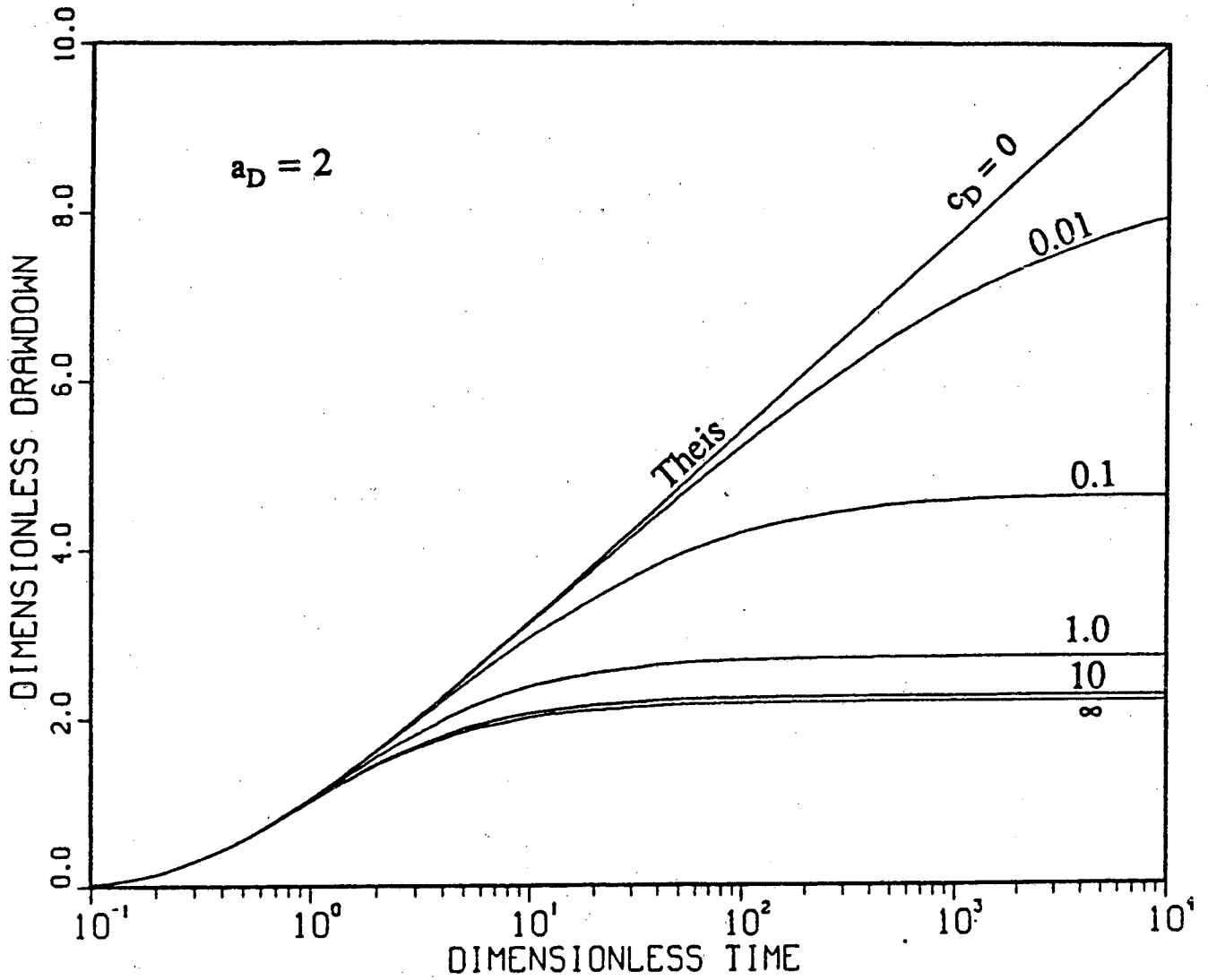
Figure 3. Semilog plots of dimensionless drawdown versus dimensionless time for $a_D = 2$ and c_D ranging from 0 to ∞.
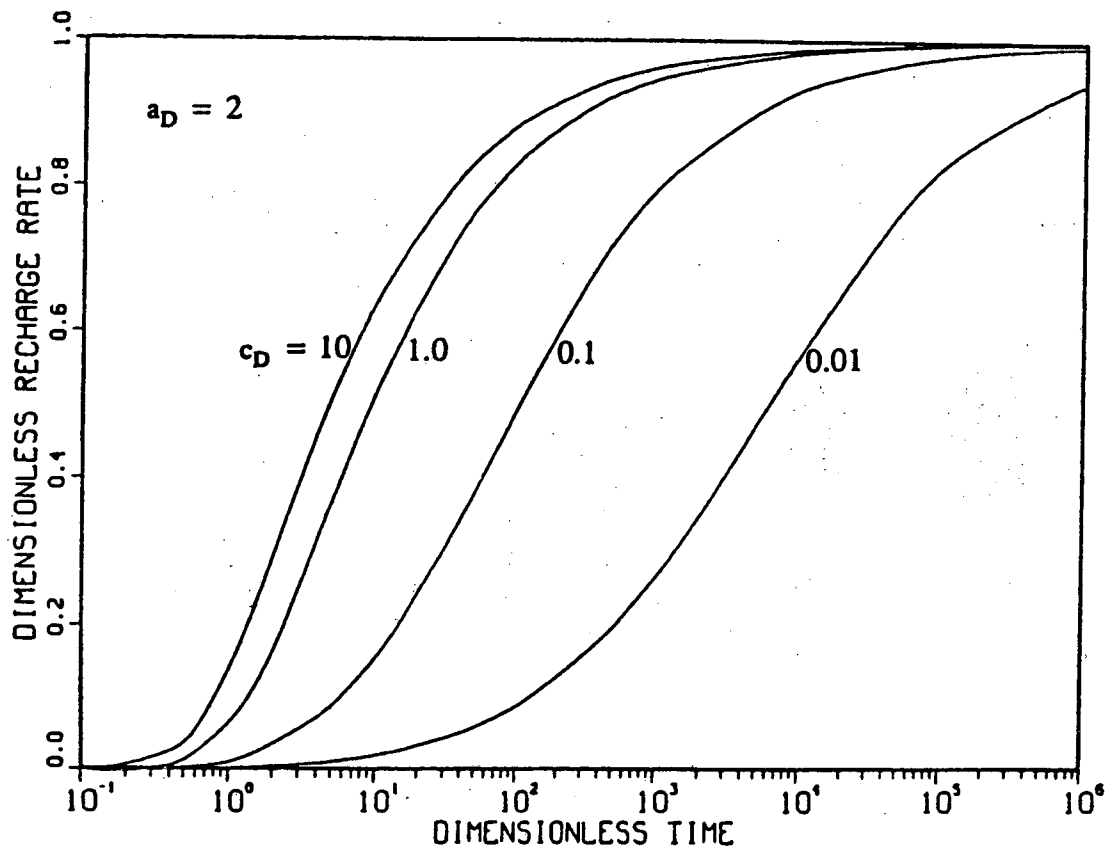
XBL 8811-10521

XBL 8811-10522

Figure 4. Semilog plots of dimensionless recharge rate versus dimensionless time for $a_D = 2$ and c_D ranging from 0.01 to 10.

Mass Transport with Chemical Reactions
in a Varying Thermal Field

C. L. Carnahan

Summary

Coupling of precipitation/dissolution reactions to diffusive mass transport via porosity changes has been implemented in the computer program THCC, a simulator of reactive chemical transport. The coupling is accomplished without increasing the set of primary unknowns. Porosity is included explicitly in the transport equations and is tracked by accounting for changes of volumes of precipitates. The coupling prevents the volume of a precipitated solid from exceeding available pore volume. Results of calculations are presented for two examples, each done with and without variable porosity.

Introduction

The work described here is part of a task to theoretically and numerically analyze effects of varying thermal fields on transport of radionuclides and groundwater components in partially saturated fracture filling materials in the near field at Yucca Mountain, and to numerically estimate the sensitivity of the effects to magnitudes of controlling parameters. Variable thermal fields imposed on previously stable or metastable fracture filling materials can induce dissolution of existing materials, transport of dissolved chemical species, and precipitation of new solid phases. Dissolution and precipitation of solids can alter the sorptive properties of fracture fillings. Redistribution of materials within fractures by chemical reactions and transport can produce changes of physical properties such as porosity, mass diffusivity, and relative permeability. Changes of these parameters can affect transport of both radionuclides and major components of subsurface fluids.

Computer programs (e.g., Grove and Wood, 1979; Miller and Benson, 1983; Walsh et al., 1984; Bryant et al., 1986; Carnahan, 1987a) that couple chemical reactions to mass transport processes have not, in general, accounted for the effects of precipitation/dissolution reactions on the transport processes. In particular, changes in the sizes of pores or apertures of fractures can alter the effective mass diffusivities and permeabilities of porous or fractured materials (Witherspoon et al., 1980; Coudrain-Ribstein, 1983), and these alterations can affect the subsequent movement of dissolved chemicals. Neglect of these effects not only might produce inaccurate computational results (Pearson, 1985), but might also lead to physically unrealizable consequences such as the calculated volume of a precipitate exceeding available pore space.

During FY 1988, research was directed toward study of changes of mass diffusivity caused by changes of porosity of fracture fillings and interactions of these changes with transport of reactive chemical species. The reactive chemical transport simulator THCC (Carnahan, 1987b, 1988a; Jacobsen and Carnahan, 1988a,b) has been modified to study effects on mass transport of precipitation/dissolution reactions.

The Computer Program THCC and Its Modifications

The THCC program simulates transport of reactive chemical species by advection and hydrodynamic dispersion or by mass diffusion in one-dimensional or cylindrically symmetric geometry. In THCC, chemical reactions are assumed to be in a state of local equilibrium. The reactions simulated are complexation, oxidation-reduction, and ionization of water in the aqueous phase, reversible precipitation of solid phases, and ion exchange. The THCC program has the capability to simulate systems with temporally and spatially variable fields of temperature and to simulate radioactive decay of selected reactants.

The program was modified by incorporating the variable porosity explicitly in the transport equations solved by the program. The primary unknowns solved for by the THCC program are the aqueous-phase concentrations of a set of "basis" species and the

"concentrations" (mole/dm^3 of porous matrix) of reversibly formed solid phases. This set of unknowns is not increased by the addition of variable porosity. Instead, the porosity (a function of space and time) is treated as a secondary unknown and is calculated from values of the primary unknown set of solid concentrations. A detailed description of the treatment of variable porosity has been given by Carnahan (1988b).

Example Calculations

The examples involve (1) precipitation along a gradient of temperature and (2) isothermal precipitation of a solid by reaction between two diffusing ions.

Transport of Silica along a Temperature Gradient.   This example simulates diffusion of silicic acid into a domain whernlet at $x = 0$. The temperature field is steady in time. Quartz prec

the reaction

$$SiO_2(\text{quartz}) + 2H_2O = Si(OH)_4^0(\text{aq}),$$
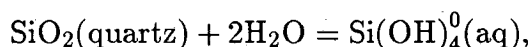
for which the equilibrium constant, K, is given as a function of absolute temperature, T, by (Rimstidt and Barnes, 1980)

$$\log K = 1.881 - \frac{1560.}{T} - 2.028 \times 10^{-3}T.$$

The temperature gradient is -20 °C/m, and the temperature at the boundary $x = 0$ is 150 °C. The outer boundary is located at $x = 5$ m. Initial porosity in the domain $x \geq 0$ was 0.05, and initial concentrations of silicic acid and quartz were zero. At $x = 0$ the incoming flux of silicic acid is 10^{-4} mole/m^{2}s.

Because quartz exhibits prograde solubility, it precipitates along the decreasing temperature profile within the domain $x \geq 0$. However, significant changes of porosity occur only at the boundary $x = 0$. Figure 1 shows the accumulation of quartz at this boundary

at times up to 10^9 s for simulations with variable porosity and constant porosity. In the case of constant porosity the non-physical result that the volume of precipitated quartz exceeds available pore space is obtained at about 0.45×10^9 s, when the solid concentration exceeds 2.2 moles/dm^3 of matrix. On the other hand, in the case of variable porosity the concentration of solid increases gradually with time and does not exceed the critical concentration. This is a result of a decreasing influx of silicic acid at the boundary caused by the decreasing porosity there. Also, the concentration of precipitated solid at the adjacent node is smaller in the variable porosity case than in the constant porosity case for all times, a consequence of reduced effective diffusivity at the boundary.

Figure 2 shows the porosity at the boundary $x = 0$ as a function of time for the variable porosity case. The decline of porosity appears to be exponential in time, approaching the asymptotic value of zero.

Precipitation of Gypsum at Constant Temperature.   This example simulates diffusion of Ca^{2+}(aq) and SO_4^{2-}(aq) into a domain where the two ions react and gypsum precipitates according to the reaction

$$CaSO_4 \cdot 2H_2O(c) = Ca^{2+}(aq) + SO_4^{2-}(aq) + 2H_2O,$$
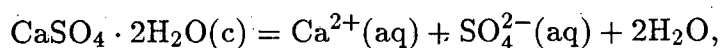
for which $\log K = -4.50$ at 25 °C (Phillips et al., 1988). Initial porosity in the domain $x \geq 0$ was 0.05, and initial concentrations of Ca^{2+}(aq), SO_4^{2-}(aq), and gypsum were zero. At $x = 0$ the incoming fluxes of Ca^{2+}(aq) and SO_4^{2-}(aq) are 10^{-3} mole/m^{2}s.

Under the isothermal condition imposed in this example, gypsum precipitates only at the boundary $x = 0$ in both constant porosity and variable porosity cases. Significant changes of porosity occur at this location in the variable porosity case. Figure 3 shows the accumulation of gypsum at this location at times up to 10^7 s for the two cases. The results are qualitatively similar to the results of the previous example. In the case of constant porosity the volume of precipitated gypsum exceeds available pore space at times greater

than about 0.14×10^7 s. In this example, the critical concentration of solid is 0.67 mole/dm^3 of matrix. In the variable porosity case the solid concentration rises asymptotically toward the critical value, again as a result of decreasing influxes of reactants at the boundary caused by decreasing porosity there.

Figure 4 shows the porosity at the boundary $x = 0$ as a function of time for the variable porosity case. As in the previous example, the porosity declines steadily and approaches zero asymptotically.

Discussion

The ability to account for variations of porosity and mass diffusivity associated with precipitation/dissolution of reactive solids provides a previously absent coupling in the direction from chemical reactions to mass transport. The method used here does not allow the non-physical exceedance of available pore volume by precipitated solids.

It is important to note that in systems of the type considered here variations of porosity and mass diffusivity *do not affect fluid-phase concentrations of reactants in equilibrium with a reactive solid*; only the rate of accumulation of the solid is affected. In the present examples the profiles of fluid-phase concentrations of reactants were identical in the cases with and without porosity variations *whenever the reactive solid was present*. This is a necessary consequence of the assumption of chemical equilibrium in the precipitation/dissolution process. However, in simulations involving dissolution of a previously precipitated solid and transport of the dissolution products, the limitation imposed by available porosity on quantities of precipitate may have to be considered.

Acknowledgment

Literature Cited

Bryant, S. L., Schechter, R. S., and Lake, L. W., 1986. Interactions of precipitation-dissolution waves and ion exchange in flow through permeable media. *AIChE Journal* *32*, 751–764.

Carnahan, C. L., 1987a. Simulation of chemically reactive solute transport under conditions of changing temperature. In Tsang, C.-F., ed., *Coupled Processes Associated with Nuclear Waste Repositories*, Academic Press: Orlando FL; Chapter 19.

Carnahan, C. L., 1987b. Simulation of uranium transport with variable temperature and oxidation potential: the computer program THCC. In Bates, J. K., and Seefeldt, W. B., eds., *Scientific Basis for Nuclear Waste Management X*, Materials Research Society: Pittsburgh, PA; pp. 713–721.

Carnahan, C. L., 1988a. Simulation of effects of redox and precipitation on diffusion of uranium solution species in backfill. In Apted, M. J., and Westerman, R. E., eds., *Scientific Basis for Nuclear Waste Management XI*, Materials Research Society: Pittsburgh PA; pp. 293–302.

Carnahan, C. L., 1988b. Coupling of precipitation/dissolution reactions to mass diffusion. Paper presented at Symposium on Chemical Modeling in Aqueous Systems II, 196th Annual Meeting of American Chemical Society, Division of Geochemistry, Los Angeles, CA, September 25–30; Lawrence Berkeley Laboratory Report LBL-26183.

Coudrain-Ribstein, A., 1983. Docteur-Ingenieur Thesis, l'Ecole Nationale Supérieure de Mines de Paris, 1983.

Grove, D. B. and Wood, W. W., 1979. Prediction and field verification of subsurface-water quality changes during artificial recharge, Lubbock, Texas. *Ground Water 17*, 250–257.

Jacobsen, J. S., and Carnahan, C. L., 1988a. Numerical simulation of alteration of sodium bentonite by diffusion of ionic groundwater components. In Apted, M. J., and Westerman, R. E., eds., *Scientific Basis for Nuclear Waste Management XI*, Materials Research Society: Pittsburgh PA.

Jacobsen, J. S., and Carnahan, C. L., 1988b. Numerical simulation of cesium and strontium migration through sodium bentonite altered by cation exchange with groundwater components. Paper presented at Twelfth International Symposium on the Scientific Basis for Nuclear Waste Management, Berlin, FRG, October 10–13, 1988.

Miller, C. W., and Benson, L. V., 1983. Simulation of solute transport in a chemically reactive heterogeneous system: model development and application. *Water Resour. Res. 19*, 381–391.

Pearson, F. J., Jr., 1985. Research needs for coupling geochemical and flow models for nuclear waste isolation. In *Proc. Workshop on Fundamental Geochemistry Needs for Nuclear Waste Isolation*, US DOE CONF8406134; pp. 173–182.

Phillips, S. L., Hale, F. V., Silvester, L. F., and Siegel, M. D., 1988. *Thermodynamic Tables for Nuclear Waste Isolation*, NUREG/CR-4864, U. S. Nuclear Regulatory Commission: Washington, DC.

Rimstidt, J. D., and Barnes, H. L., 1980. The kinetics of silica-water reactions. *Geochim. Cosmochim. Acta 44*, 1683–1699.

Walsh, M. P., Bryant, S. L., Schechter, R. S., and Lake, L. W., 1984. Precipitation and dissolution of solids attending flow through porous media. *AIChE Journal 30*, 317–328.

Witherspoon, P. A., Wang, P. S. Y., Jwai, K., and Gale, J. E., 1980. Validity of cubic law for fluid flow in a deformable rock fracture. *Water Resour. Res. 16*, 1016–1024.
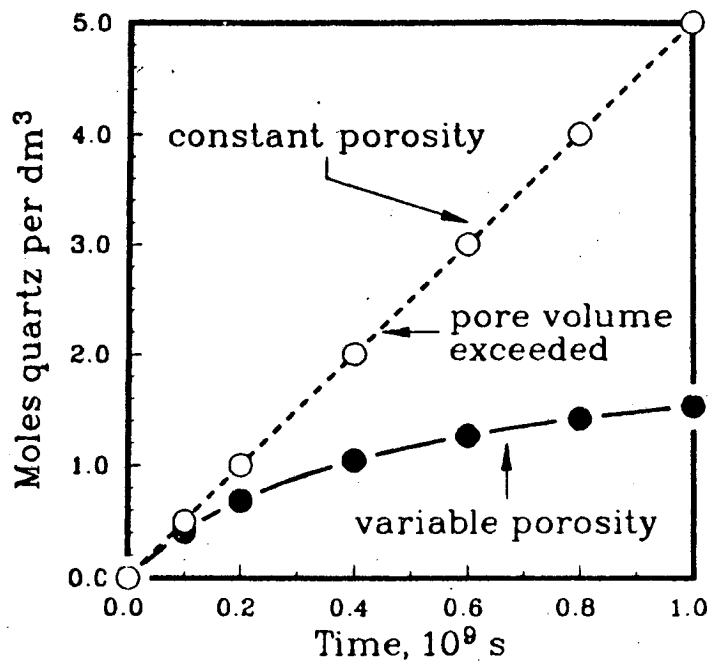
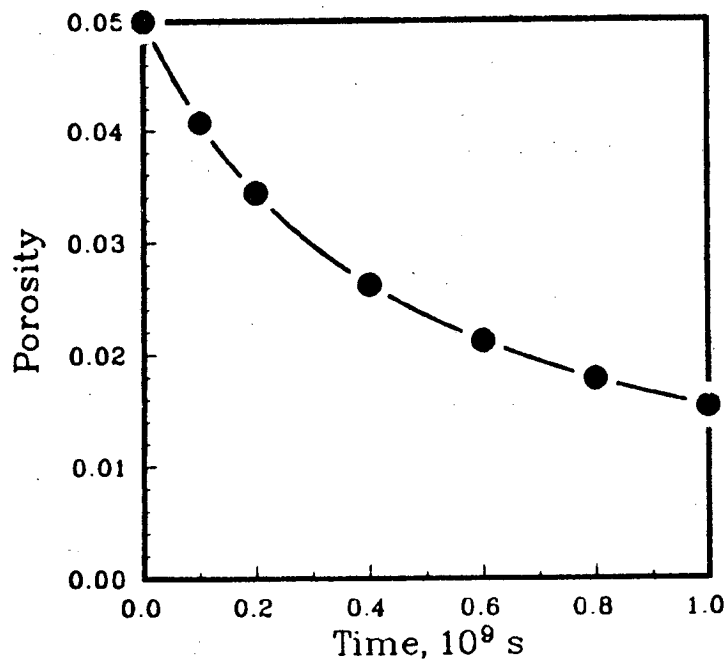Figure 1. Quartz precipitated at boundary $x = 0$.

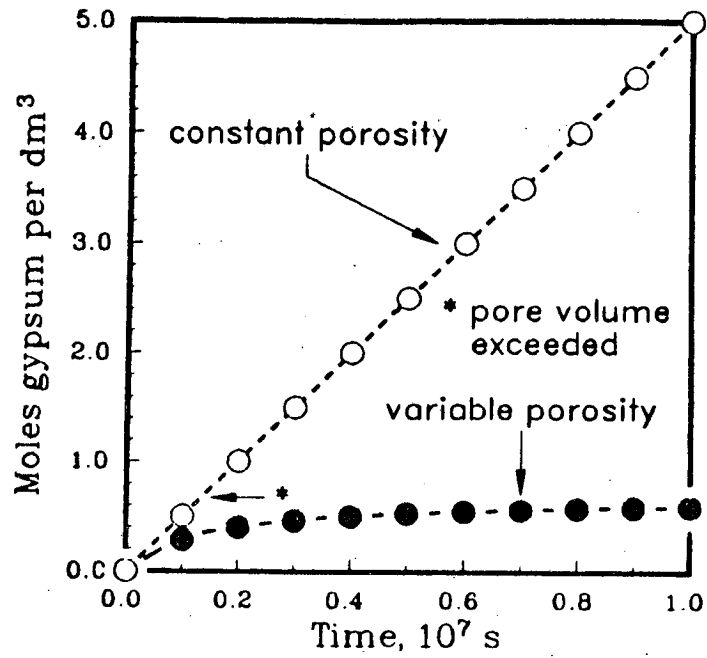Figure 2. Porosity at boundary $x = 0$ for quartz precipitation.

Figure 3. Gypsum precipitated at boundary $x = 0$.
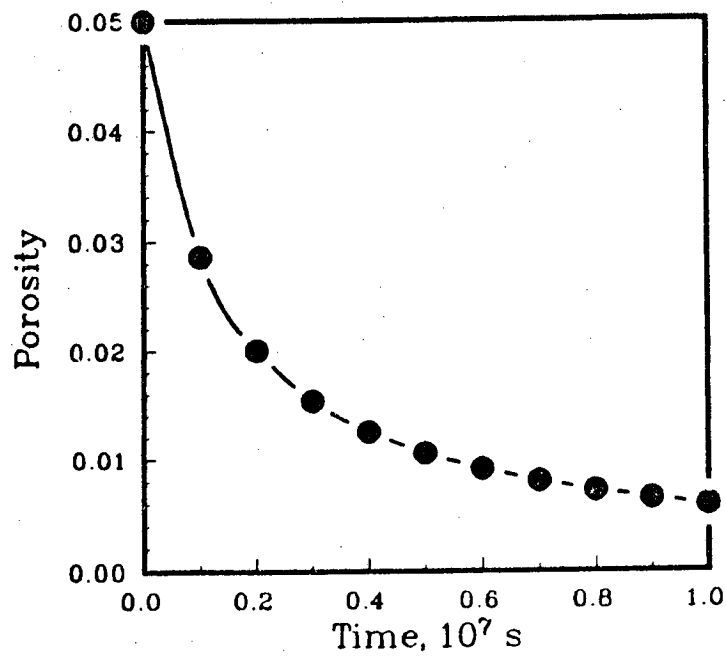
Figure 4. Porosity at boundary $x = 0$ for gypsum precipitation.

Investigation of Seismic Imaging for Fracture Characterization

E. L. Majer, T.V. McEvilly and K. H. Lee

Earth Sciences Division
Lawrence Berkeley Laboratory
University of California
Berkeley, California 94720

Introduction

One of the most crucial needs in the design and implementation of an underground waste isolation facility is a reliable method for the detection and characterization of fractures in zones away from boreholes or subsurface workings. The fracture network will largely determine the hydrological and geomechanical response of the host rock under thermal loading. Within underground workings we are able to examine fractures directly, however, a major problem exists in trying to extrapolate this characterization to unexposed regions. Geophysical methods represent our approach to these problems. If fractures represent anomalies in the elastic properties of the rocks, then the seismic techniques may be useful in detecting and characterizing fracture properties. For years seismologists have known that fractures have an effect on the propagation of seismic waves. The problem has been in quantifying the effect so that useful parameters can be obtained. In the case of nuclear waste isolation, and in particular Yucca Mountain, the parameters of interest are not only the presence of fractures, but such features as length, width, orientation, density, spacing, aperture, and the degree to which the fractures are connected, and the manner of the connections. Given finite time and economic resources it is unreasonable to assume that the seismic methods can yield all the information that is necessary to infer the above properties of fractures at all scales, in fact it may be unreasonable to assume that all the geophysical methods combined can yield all the parameters necessary. However, at scales on the order of

tens of meters on a repository wide scale, and scales on the order of meters for inter-tunnel regions, seismic methods may be very useful for fracture characterization.

The techniques of Vertical Seismic Profiling (VSP) and crosshole imaging may be applicable in characterizing fractured media. Through tomographic analysis of VSP data, it may be possible to map the elastic properties indicative of fracture content and structure. Such methods use travel times, amplitudes, and particle motions of the P-, SV-, and SH-waves to estimate fracture orientation, density, and distribution. Resulting properties can then be used to construct hydrologic or geomechanical models of fracture networks to study the behavior of the rock mass. The VSP method is being evaluated as a tool for fracture definition in repository siting and performance evaluation. This research is aimed at aiding the development of techniques to determine the seismic response of fractured media, and will evaluate VSP and crosshole tomography as a tool for mapping the relevant properties throughout the repository volume. If successful the technique will provide a method to help characterize the overall hydrologic and geomechanical properties of the repository.

Work to date

Two years of research has been carried out to date. The initial focus of this research in the first year was the development of a model to predict how seismic waves travel through a fracture network. Whereas several numerical techniques are available for predicting fluid flow through fracture networks, the corresponding computational tools for determining how a seismic wave is affected as it is transmitted through a network of randomly located and oriented finite fractures was not available at the onset of this study. The development of such a seismic modeling tool has been a high priority for this project.

The first attempt was to modify our present one-dimensional and two-dimensional ray tracing and synthetic seismogram models that relied upon conventional welded boundary theory to admit 'stiff' fracture surfaces with arbitrary orientation. The goal was to incorporate the boundary conditions that admit slip along an interface into a ray

tracing program so that very thin features such as fractures could be modeled. It is necessary to include the displacement discontinuity boundary conditions in the solution for the propagation of the seismic wavelet. The constitutive equations for this model come from the study of single fractures which is ongoing at LBL. The approach finally taken was to modify a code that is used for hydrologic modeling of fractured media. This code, Fracture Mesh Generator (FMG) generates any desired fracture distribution (density and sizes), and calculates the relative position of each fracture. The new program FMGRAY was used to obtain the center position of each fracture and to calculate the ray tracing coordinates. A second program was also developed, SYNHYD1. This code is the Cerveny synthetic seismogram generator, i.e., SYNTPL with the fracture information included. This has also been modified to include the stiffness effect of fractures on the seismic waves in addition to the geometry information.

Using this modeling capability we can now vary fracture geometry, density and orientation in a medium and measure the seismic response. Because we used FMG to generate our fractures, we can compare the seismic response to the hydrologic response. An example of the application of this program is shown in Figure 1. Although any degree of complexity can be achieved, this model does not have the capability to model the diffractions or scattering associated with the fracture sets. Although this approach is very promising for forward modeling of fractured media, there is one drawback. One must have an idea of the relationship between stiffness, or the amount of slip along an interface, and the physical property of the fracture. Studies that address this issue are presently being carried out on the laboratory scale within the scope of this project by Myer and Cook in this project and on limited field scales by LBL in other projects.

In addition to the approach outlined above, we also believe that fractures strongly affect the anisotropy one measures in the velocity and amplitude of the seismic waves. For this reason we set out to obtain state of the art capabilities in seismic wave anisotropy. Two programs were obtained, Beam87 and ANRAY. The programs were developed by V. Cerveny, D. Gajewski and I. Psencik. V. Cerveny spent several months at LBL bringing up these programs at LBL. Beam87 is a 2-D Gaussian beam

ray tracer while ANRAY is a 3-D fully anisotropic modeling code that allows one to specify 21 elastic constants and a vertically varying velocity model. The programs were not initially written for crosshole and VSP applications. The work during the last year has been to improve these programs and modify them so that VSP and crosshole applications can be modeled. It was also necessary to allow amplitude calculations to be output for ANRAY so that full wave form information could be obtained. During the last several months we have been working with Dirk Gajewski to achieve this. An example of the results are shown in Figures 2a to 2d. In 2a and 2b are shown isotropic models of the ray paths through Yucca Mountain for the P- and S-wave. The velocity models were obtained from G-4 and G-1 sonic logs, the S-wave models were of course not obtained from the sonic logs but estimated using a Possions ratio of 0.25.

In addition to this modeling work using these programs work is underway to combine the FMGRAY and ANRAY approach.

It has been known that elastic waves are affected, in varying degrees, by such simple linear features as bedding interfaces, faults, and fractures. numerical solutions for the scattering by these objects have been limited to those of approximate nature due to the complexity involved with the exact solutions. A fracture response, for example, have been obtained using either essentially the Born approximation at low frequencies, or the ray tracing technique at high frequency limits. The Kirchhoff integral approximation also belongs to the high frequency regime. As the wave propagates through a fracture or a zone of fracture it not only loses its energy resulting in the decrease in amplitude, but experiences the apparent slowing down of velocity. Approximate solutions mentioned above often do not contain precise scattering informations necessary for the correct interpretation. It is therefore proposed that we develop better numerical solutions, which in turn will be used to further enhance our ability to interpret field data.

As a first step we have assumed an elastically inhomogeneous object characterized by λ_1, μ_1, ρ_1 enclosed by a closed surface S in a uniform whole space of λ_0, μ_0, ρ_0. It has been shown that the displacement, u, can be obtained from the

Helmholtz-type surface integral

$$u(x) = u^i(x) + \int_S \left\{ u(x') \cdot n' \cdot \Sigma^0(x/x') - t(x') \cdot G^0(x/x') \right\} ds' \qquad (1)$$

outside the object, and

$$u(x) = - \int_S \left\{ u(x') \cdot n' \cdot \Sigma^1(x/x') - t(x') \cdot G^1(x/x') \right\} ds' \qquad (2)$$

inside the object. Here G is the Green's displacement dyadic and Σ is a third rank Green's stress tensor. The term t(x) is the surface traction on S. These two equations can be made into a system of coupled Fredholm integral equation of the second kind if the field point x is allowed to approach the surface S. At any point on the surface there are six unknowns; three components each from u and t. When either t or u is known on S, such as in the case of a traction free void (t = 0) or a rigid inclusion (u = 0), the integral equation Equation (1) is reduced to one in which only one unknown vector remains to be solved. The other special case of interest involves an object whose thickness in one direction becomes infinitestimally thin. Assuming continuous traction across the crack, Equation (1) is further reduced to

$$u(x) = u^i(x) + \int_{S/2} \Delta u(x') \cdot n' \cdot \Sigma^0(x/x') \, ds' \qquad (3)$$

where $\Delta u(x')$ is defined as the jump in u(x') across the crack surface S. Notice that if there is no crack (perfectly welded interface h), Δu would be zero, and $u(x) = u^i(x)$ would result.

Experimental results and theoretical thin layer analysis show that the discontinuity in the displacement vector is related, independently from the frequency used, to the local traction through the stiffness, k, of the crack

$$\Delta u = \frac{t}{k} \qquad (4)$$

Substituting this relationship to Equation (3), and operating on both sides by the surface traction operator

$$L = 2\mu \frac{\partial}{\partial n} + \lambda n\nabla\cdot + \mu n\times\nabla\times$$

we finally get

$$t(x) = t^i(x) + \int_{S/2} \frac{t(x')}{k(x')} \cdot n' \cdot L \left\{ \Sigma^0(x/x') \right\} ds' \tag{5}$$

This is an integral equation for the traction on S, where the stiffness k(x) can be a function of x. The kernel is generally singular and it is critically important that appropriate physical concepts need to be introduced to properly evaluate the integral over the surface. Once the traction is numerically obtained on S, we can compute displacement field u everywhere using Equation (3) with Δu replaced by $\frac{t}{k}$.

It is now left to insert this approach into the ANRAY code. After doing this we will have a realistic modeling approach to fracture modeling.

Recommendations and Future Work

If successful, the VSP method could prove to be a valuable method in siting and evaluating future repository sites, and including anisotropy into the matrix properties. In terms of the Yucca Mountain project is crucial at this point to obtain 3-component data from sites similar in character to Yucca Mountain if not at Yucca Mountain. It still must be determined if the VSP/Tomographic techniques will be of use in a partially saturated rock with the characteristics of the Yucca Mountain tuff. If possible S-wave velocities from core at Yucca Mountain would also be helpful. At this point it seems that seismic methods using surface to borehole and borehole to borehole techniques will be very useful, however only field data will tell for sure.

If the seismic modeling indicates that seismic response is sensitive to the geometric parameters which control saturated flow, it will be necessary to determine how unsaturated flow is controlled by these parameters. Also, we do not expect the geophysics to tell us the location of every fracture. Rather, in each pixel we will have some average property. The use of fracture models which incorporate geostatisical simulation is also based on average pixel properties.

The key to this effort is to interpret the data in light of the experimental and theoretical work that LBL and others have been doing on the effect of fracture stiffness and infilling material on the velocity, amplitude, and polarization of seismic waves. This is an extension of the shear-wave splitting that many have observed in fractured media. Its attractiveness is that it offers a quantitative solution to fracture spacing and orientation. If this approach works out as well as we expect it to, it will be invaluable for defining fracture content and density, especially for fracture sets that do not intersect the borehole. It will also point the way as to how to design and implement future studies from other boreholes and the underground workings.
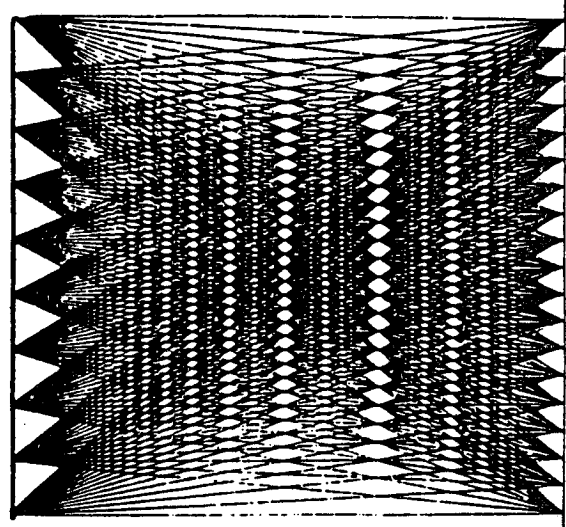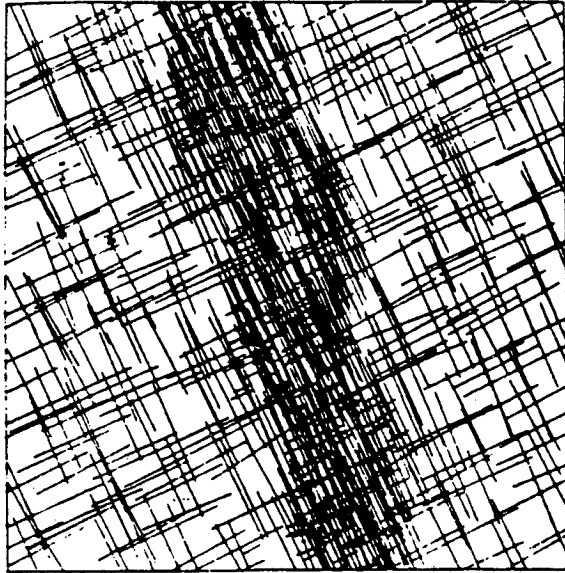
LD study, NS plane, l=1000, dens = 1e-6

iu' 1983

flow region   xm
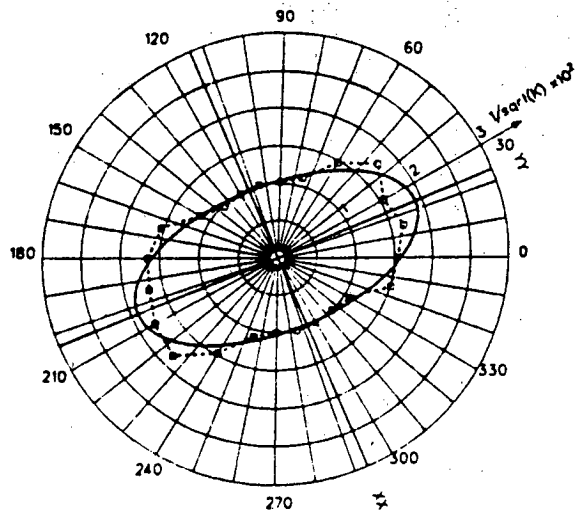
PERMEABILITY ELLIPSE

(nmse =   0 0201)
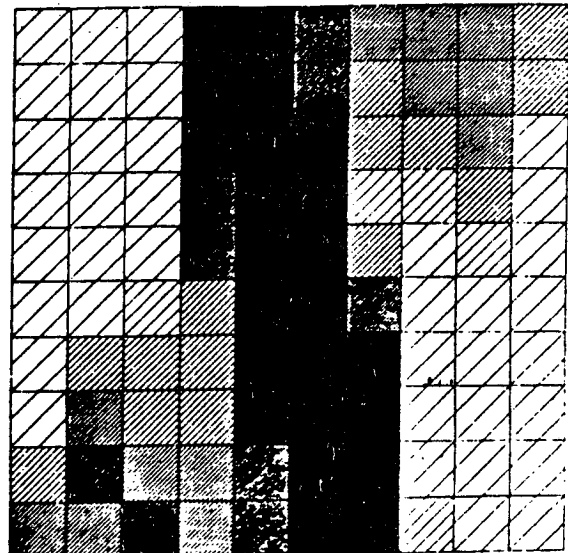
Figure 1.   An example of the Program FMG Ray and a comparison of the result of
seismic imaging (tomogram) to hydrologic modeling of the fracture zone.
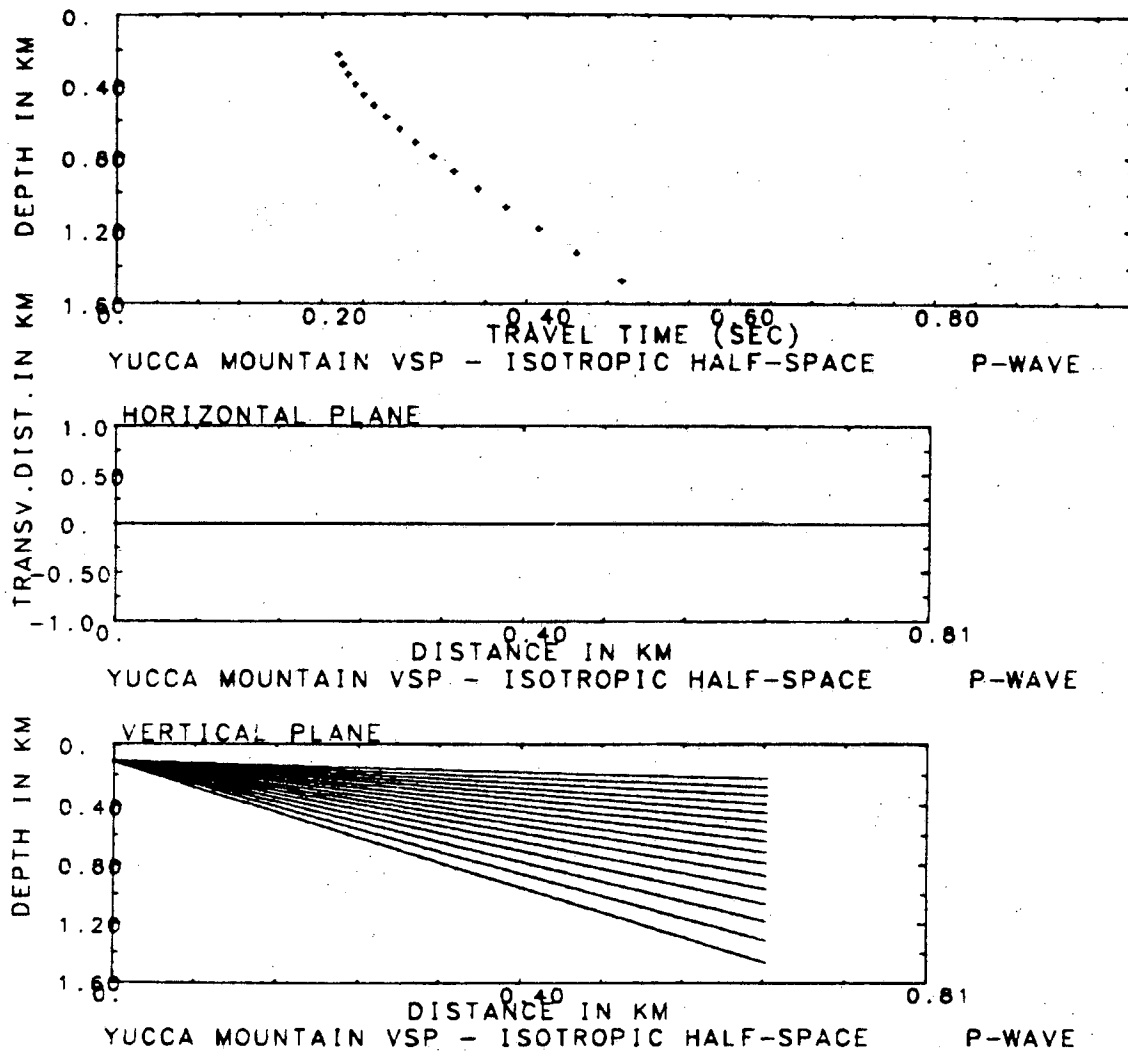
Figure 2a. Beginning P-wave model for a representative section through Yucca Mountain.
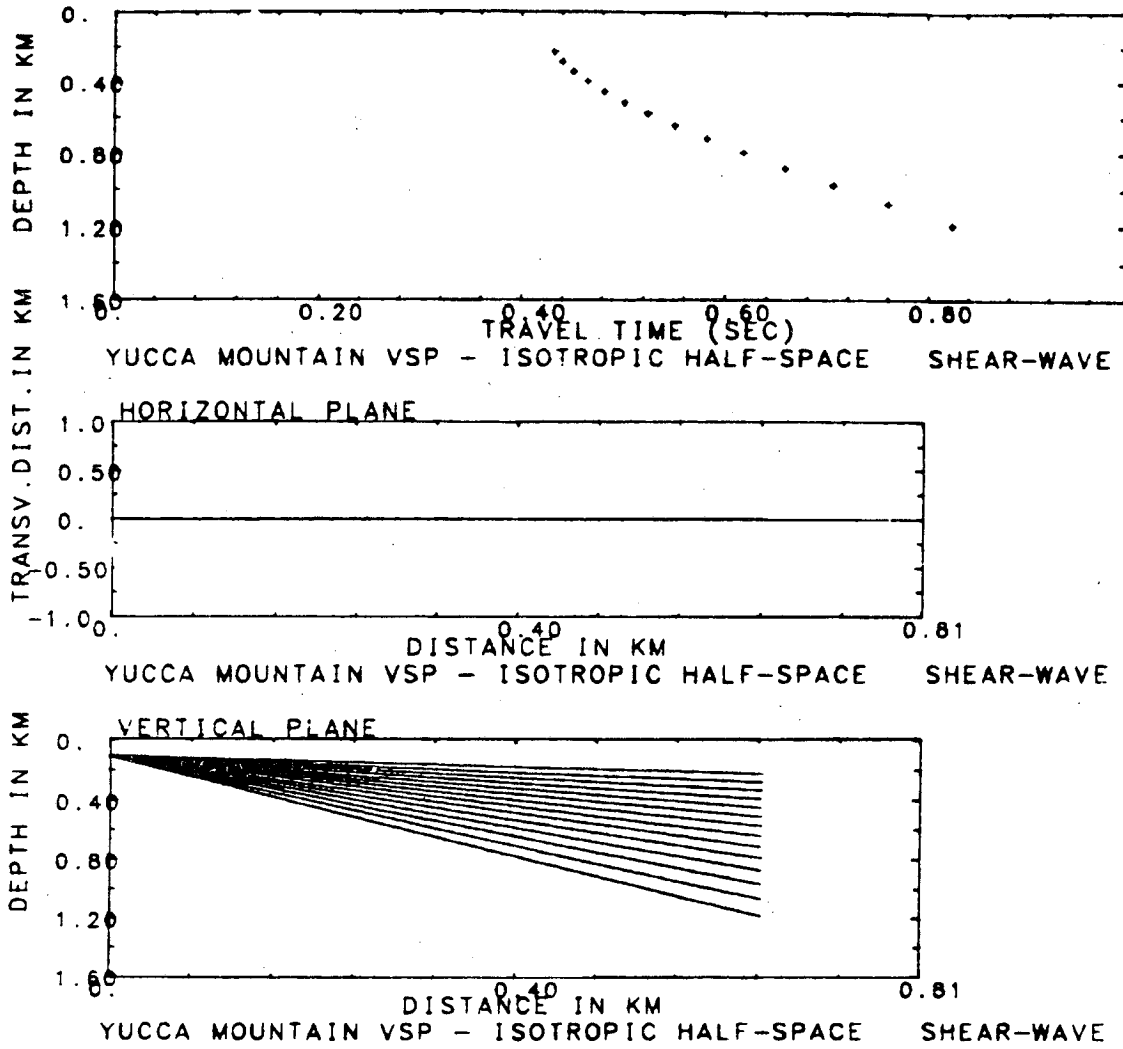
Figure 2b. Beginning S-wave model for a representative section through Yucca Mountain.

DEPTH IN KM

TRAVEL TIME (SEC)

YUCCA MNTN VSP – 4 LAYER ANISOTROPIC – qS2 SHEAR-WAVE

HORIZONTAL PLANE

TRANSV.DIST.IN KM

DISTANCE IN KM

YUCCA MNTN VSP – 4 LAYER ANISOTROPIC – qS2 SHEAR-WAVE

VERTICAL PLANE

DEPTH IN KM

DISTANCE IN KM

YUCCA MNTN VSP – 4 LAYER ANISOTROPIC – qS2 SHEAR-WAVE
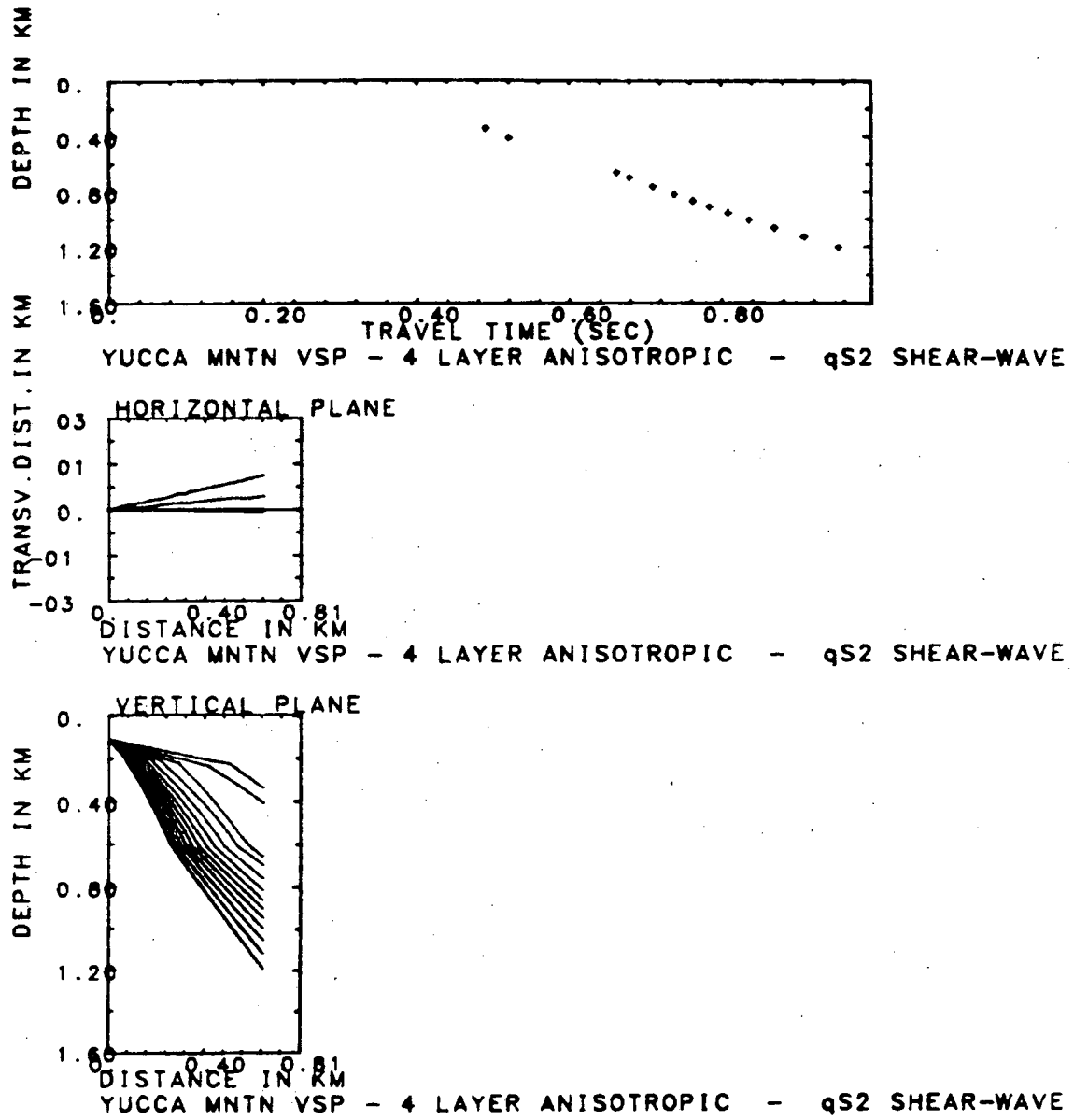
Figure 2c. The effect of introducing a 10% anisotropy in the P-wave model.

YUCCA MNTN VSP — 4 LAYER ANISOTROPIC — qS1 SHEAR-WAVE

HORIZONTAL PLANE

YUCCA MNTN VSP — 4 LAYER ANISOTROPIC — qS1 SHEAR-WAVE

VERTICAL PLANE

YUCCA MNTN VSP — 4 LAYER ANISOTROPIC — qS1 SHEAR-WAVE
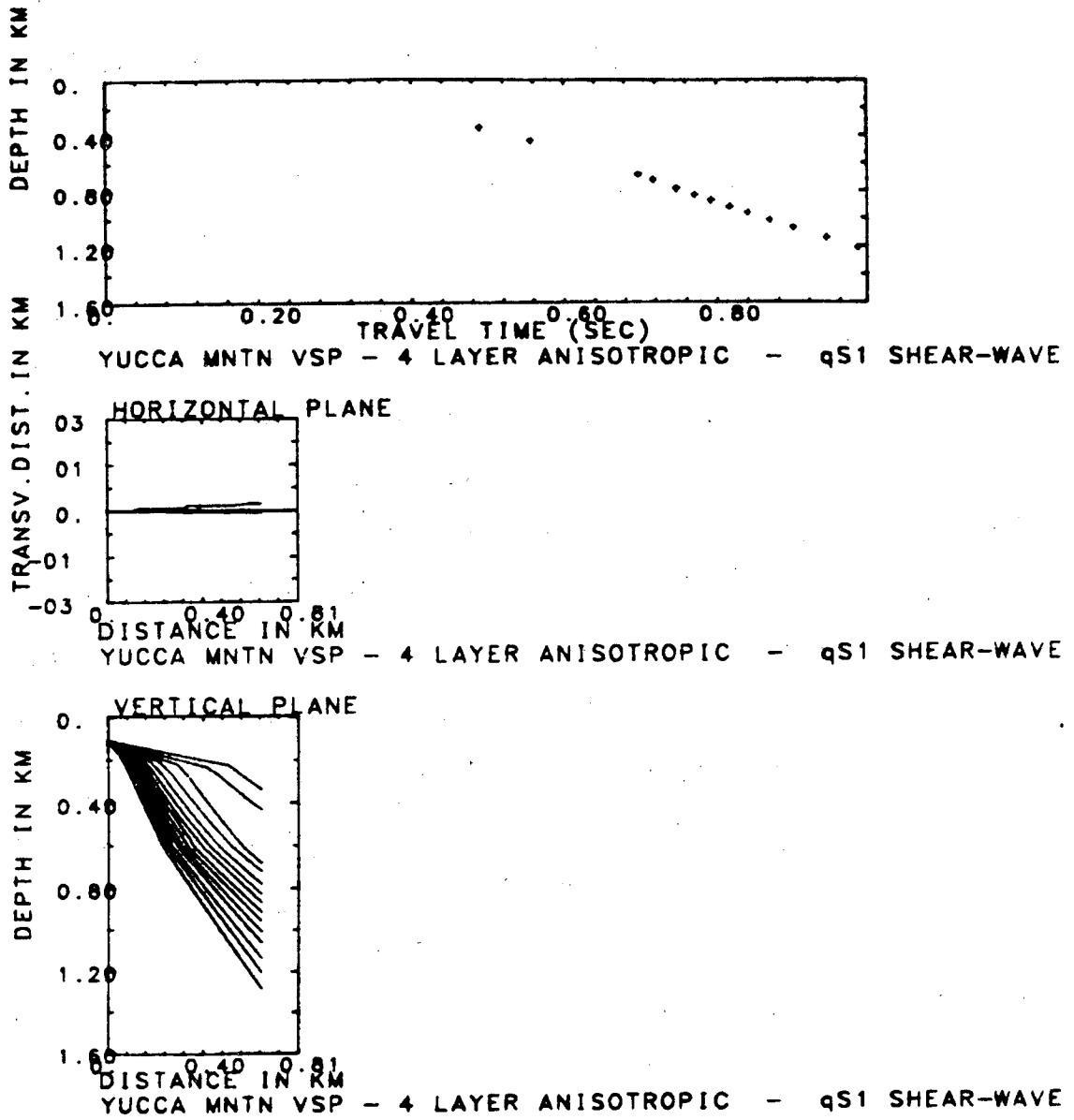
Figure 2d. The effect of introducing a 10% anistropy in the S-wave model.

A Mechanical Model for Normal and Detachment Faulting
in the Basin and Range: Applications to Yucca Mountain, Nevada

John M. Kemeny and Neville G. W. Cook

Introduction

The Basin and Range province occupies the whole of Nevada and parts of Oregon, Idaho, Wyoming, Utah, California, and Arizona. The Basin and Range is an extensional regime, cut by widely spaced (20 - 30 km) and relatively steeply dipping normal faults that penetrate down to the brittle-ductile transition at a depth of 10 - 15 km (e.g., Smith and Bruhn, 1984). It is well known that these normal faults are responsible for large earthquakes in the Basin and Range, such as the magnitude 7.5 earthquake at Hebgen Lake, Montana on August 18, 1959 (Nolan, 1964; Doser, 1985), and the magnitude 7.3 earthquake at Borah Peak, Idaho on October 28, 1983 (Doser and Smith, 1985; Stein and Barrientos, 1985). The Basin and Range is also cut in places by shallow, low dipping (less than 30°), detachment faults. These faults have in some circumstances undergone translational displacements in excess of tens of kilometers (Davis and Lister, 1988), yet because of the lack of normal faulting earthquakes on fault planes dipping at less than 30°, it must be assumed that deformation along detachment faults in the Basin and Range occurs aseismically (England and Jackson, 1987). There are a number of brittle structural features associated with the shallow detachment faults, such as steeply dipping normal faults above the detachment faults that terminate at the detachment surface, and listric normal faults that merge into the detachment surface. Whether these structural features deform seismically or aseismically is not well understood at the present time.

Yucca Mountain, located in southwestern Nevada, is a possible site for the underground storage of nuclear waste. Yucca Mountain is cut by a series of steeply dipping normal faults. The most important of these are the Solitario Canyon and Bow

Ridge faults on the western and eastern flanks of Yucca Mountain, respectively, and the Ghost Dance fault, which goes directly through the proposed repository site. In addition to these normal faults, there is evidence in the region southwest of Yucca Mountain to support the existence of a shallow detachment fault at a depth between two and four km below Yucca Mountain (Scott, 1986). Thus the steeply dipping normal faults that cut Yucca Mountain may terminate at or merge with this shallow detachment fault, or the normal faults may pass through the detachment fault and extend to much greater depths.

It is important to understand the consequences of fault motion on normal and detachment faults in the region surrounding Yucca Mountain. In addition to ground shaking and fault offsets, the stress regime in the ground can be significantly altered due to motion along these faults. Two kinds of stress changes can occur due to fault motion in the Basin and Range: 1) a redistribution of stress away from areas that have slipped towards unslipped areas (average stress in the region remains unchanged), and 2) a regional change in stress (average stress in the region changes). Regional stress changes occur due to the fact that the driving force for motion along faults in the Basin and Range is from viscous motion below the brittle-ductile transition (e.g., Hamilton, 1987). For short-time events such as seismicity, this viscous coupling responds like a fixed displacement boundary condition. Since the far field displacements are fixed, the energy used up by the earthquake causes the far field stress to drop. After the earthquake, the far field stresses slowly rebuild due to the continuing viscous motion at depth, resulting in another earthquake at a future time when the stresses have built up to their previous level, and completing the earthquake cycle.

These changes in stress in the ground can induce pore pressure changes and groundwater flow. The local stress changes induce flow from regions of high pore pressure towards regions of low pore pressure, as analyzed by Rice and Cleary (1976), Li et al. (1987), Detournay and Cheng (1988), and others. The regional stress changes could, by being large scale, cause regional changes in pore pressure. In an extensional

regime such as the Basin and Range, a drop in tectonic stress due to faulting results in an increase in compressive stress in the ground. One effect of this increase in compression is to reduce the pore volume of the rock, which increases pore pressure and could induce regional water level changes. An increase in compression can also squeeze fluids out of cracks and fault zones, and towards the ground surface, as analyzed by Sibson (1981, 1982). This has important implications at Yucca Mountain, since at the present time the water table is below the proposed level for the repository. An indication that regional stress changes can occur is the fact that following the Hebgen Lake, Montana magnitude 7.5 earthquake in 1959, changes in water levels in wells were detected as far away as Hawaii and Puerto Rico (Da Costa, 1964).

In this paper a simple model for the mechanics of normal and detachment faulting in the Basin and Range is presented. In this model, the propagation of slip along a single, planar, normal fault is explicitly considered. The propagation of slip can initiate either from an aseismically deforming detachment fault, or from aseismic slip below the brittle-ductile transition. These calculations are based on quasi-static fracture mechanics, and are extensions of work conducted on strike-slip faulting by Kemeny (1989a). An important element of this model is that we consider slip under realistic boundary conditions for the Basin and Range. In particular, as driving forces for slip along faults, we consider the combined effects of gravity and far field displacements imposed by viscous coupling below the brittle-ductile transition.

The model calculates both aseismic and seismic deformation due to the propagation of slip along the normal fault, and the moment and energy release associated with seismic motion. Most importantly, our analysis gives regional stress changes associated with seismic and aseismic deformation, and from these stress changes, bounds on possible water level changes can be estimated. A more rigorous analysis that could be conducted in the future involves coupling the elastic deformations, pore pressure changes, and flow,

as analyzed for other geologic situations by Rice and Cleary (1976), Li et al. (1987), Detournay and Cheng (1988), and others.

Mechanical Model for Normal and Detachment Faulting

Consider the simple model for faulting in the Basin and Range as shown in Figure 1. The model consists of a two dimensional (plane strain) linear elastic plate of width b and thickness t containing a single edge crack of initial length l_o at an angle β from horizontal. The top surface of the model represents the ground surface. The bottom surface of the model represents either the lower limit of brittle behavior (brittle-ductile transition), or a detachment fault surface (assumed horizontal). In both cases the movement along the bottom surface of the model is assumed to occur aseismically. The normal fault is represented by the angle crack, and a slip event along the normal fault is modelled as the propagation of the crack from its initial position towards the top of the plate. Modelling the propagation of slip along a pre-existing fault plane as the in-plane propagation of a crack has been considered previously for the case of strike slip faulting by Kemeny (1989b), and others. Since the edge crack is at the lower surface of the model, this model assumes that rupture nucleates deep in the ground and ruptures upward, which agrees with observations in the Basin and Range (e.g., Sibson, 1982).

Tectonic extension is modelled by considering an imposed extensional displacement, D, at a distance d from the normal fault. For simplicity, we assume that the applied displacements are uniform with depth, which agrees with several models for strain accumulation in the Basin and Range (England and Jackson, 1987; Lin and Parmentier, 1988). Because the plate is assumed to be elastic, there is a linear relationship between the far field applied displacement and the far field stress, σ, which depends on the stiffness of the ground in between the applied displacements.

The other important driving force in the model is gravity. We assume the vertical stress due to gravity as that due to the weight of the overburden material. Thus the

vertical stress due to gravity will increase linearly with depth, given by $\sigma_v = \rho g h$, where ρ is the ground density, g is the gravitational acceleration, and h is the depth below the ground surface. Gravity also imparts a horizontal stress, due to an elastic effect from the vertical stress, and also due to non-elastic deformation such as compaction and slip along joints and faults. Based on Zoback and Zoback (1980) and others, the horizontal stress in the direction perpendicular to normal faulting in the Basin and Range is the minimum principal stress, which is a result of the regional extension in that direction. For our purposes, we are interested in the value of the horizontal stress if the tectonic extension were turned off (since we model the tectonic extension separately). Under the assumption of vertical loading with lateral constraint, the horizontal stress due to gravity alone would be $v/(1-v)$ times the vertical stress at any depth, where v is Poisson's ratio (Jaeger and Cook, 1979). More realistic assumptions about ground deformation give a horizontal stress closer to 1 times the vertical stress at any depth (e.g., McGarr, 1988). For the Basin and Range, a good approximation for the component of horizontal stress perpendicular to normal faulting due to gravity alone may be the value of the horizontal stress in the direction of the normal faults, which is still less than the vertical stress (Zoback and Zoback, 1980). We have left the horizontal stress as a variable, as a constant F times the vertical stress at any given depth. For the Basin and Range, it is expected that F will range from 0.6 to 1.0.

Aseismic and seismic deformation along the normal fault occur by the propagation of the crack towards the free surface. We make the assumption that the crack will grow in the plane of the fault, which is consistent with the macroscopic response for the propagation of slip along a pre-existing fault plane. It does ignore, on a smaller scale, the extensile features that can form near a deforming slip surface. In this scenario, slip is driven solely by the mode II stress intensity factor, K_{II}, and this will result in a slip event that is 'pure double couple'. Also, it is assumed that the crack remains closed throughout the faulting process (the mode I stress intensity factor, K_I, remains negative) and is

subject to frictional constraints. Thus we assume that the crack face is under a non-uniform frictional stress τ^f, where at any point along the crack surface $\tau^f = \mu_f \sigma_n$, where μ_f is the linear coefficient of friction and σ_n is the normal stress at that point.

We have estimated a closed form solution for K_{II} for the model with an arbitrary angle β, based on the stress intensity factor solution for an edge crack in a finite plate (Tada et al., 1973). Our solution includes the effects of tectonic extension, gravity, and friction, and is given by:

$$K_{II} = \left[\sigma + \rho g b\, (1.12 - 0.68 \frac{l\sin\beta}{b})(1 - F) \right. $$

$$\left. + \sigma_n\, \mu_f \right] \sin\beta\cos\beta\, \sqrt{\pi l}\ \ Y_{II}(\frac{l\sin\beta}{b}) \qquad (1)$$

where

$$\sigma_n = \left[\sigma - \rho g b\, (1.12 - 0.68 \frac{l\sin\beta}{b})\, (\frac{1}{\tan^2\beta} + F) \right] \sin^2\beta$$

and

$$Y_{II}(x) = \frac{1.12 - 0.56x + 0.085x^2 + 0.180x^3}{\sqrt{1-x}}$$

Here we use the sign convention that tension is positive. Initially, for small σ, K_{II} may be negative, and this indicates that the crack faces are locked due to frictional forces. As σ is increased, the frictional forces decrease and the driving forces along the crack increase, resulting in slip along the crack faces for $K_{II} > 0$ (thus equation 1 is valid only for $K_{II} \geq 0$). Also, if $\sigma_n > 0$, this indicates that the crack faces are under tension and the assumption that the crack surfaces are closed and under frictional forces is no longer valid.

Following rate-independent linear elastic fracture mechanics (e.g., Lawn and Wilshaw, 1975), it is assumed that the crack will grow when the energy release rate, G, becomes

equal to some critical value referred to as G_c. G_c represents the energy required for the breakdown processes at the crack tip and is a material property, while G is related to the stress intensity factors and is a function of crack geometry and the applied stresses and strains. Under pure mode II loading, G is related to K_{II} by (plane strain):

$$G = \frac{K_{II}^2 (1 - v^2)}{E}$$ (2)

where E is Young's modulus and v is Poisson's ratio. G_c is one of the most important parameters in the model. G_c is found to be very scale dependent, and also varies with normal stress (Wong, 1982, 1986; Kemeny and Cook, 1987). We estimate a value for G_c for normal faulting in the Basin and Range by modelling known earthquakes and comparing the measured source parameters with calculated ones.

Together, equations (1) and (2) control the stress at the onset of crack growth, and the change in stress as the crack continues to propagate towards the ground surface. Since the stresses due to gravity remain constant as the crack propagates, the only stress that changes is the far field tectonic stress, σ. The value of σ at which cracking will occur for a crack of length l, referred to as σ^*, is calculated from equations (1) and (2) under the restriction that $G = G_c$, and gives:

$$\sigma^* = \frac{\sqrt{\frac{G_c E}{(1 - v^2)\pi l}} \frac{1}{\sin\beta\cos\beta Y_{II}} - \rho g b(1.12 - 0.68\frac{l\sin\beta}{b})\left[1 - F - \mu_f(\cos^2\beta + F\sin^2\beta)\right]}{1 + \mu_f\sin^2\beta}$$ (3)

Note that it is assumed in equation (3) that G_c is a material constant independent of stress state.

In addition to a change in stress, a change in crack length is associated with a change in the double couple component of the seismic moment, M_o. For the two dimensional crack representing the normal fault in this model, the seismic moment is defined as:

$$M_o = 2\,l\,\mu\,\delta\,t \qquad (4)$$

where δ is the average relative shear displacement of the crack surfaces, and μ is the elastic shear modulus. δ can be calculated for the model in Figure 1 by integrating the energy release rate, G, over the length of the crack and utilizing equations (1) and (2) (see Kemeny, 1989a, for details). Then, using equation (4), this gives the following closed form solution for M_o:

$$M_o = b^2\pi t(1-v)\cos^2\beta(1 + \sin^2\beta\mu_f)\left[\sigma(1 + \sin^2\beta\mu_f)I_{II}^1(l\sin\beta/b)\right.$$
$$\left. +\rho g b(1 - F - \sin^2\beta\mu_f)(\frac{1}{\tan^2\beta} + F)(1.12I_{II}^1(l\sin\beta/b) - 0.68I_{II}^2(l\sin\beta/b))\right] \quad (5)$$

where

$$I_{II}^1(x) = \left[-0.67\ln(1-u) + 0.906(1-u) - 0.638(1-u)^2 + 0.502(1-u)^3\right.$$
$$\left. -0.226(1-u)^4 + 0.131(1-u)^5 - 0.42(1-u)^6 + 0.0046(1-u)^7\right]_0^x$$

$$I_{II}^2(x) = \left[-0.67\ln(1-u) + 1.576(1-u) - 1.093(1-u)^2 + 0.927(1-u)^3\right.$$
$$\left. -0.603(1-u)^4 + 0.312(1-u)^5 - 0.152(1-u)^6 + 0.041(1-u)^7 - 0.004(1-u)^8\right]_0^x$$

In seismology, a seismic moment is usually associated only with unstable fault movement. However, we note that the moment as defined in equation (5) is a measurable quantity for both seismic and aseismic fault motion.

The final equation that is needed describes the unloading of the surrounding ground due to the propagation of slip along the normal fault. This drop in stress is due to the fact that the far field boundary conditions are imposed displacements rather than stresses. In our analysis, the particular quantity of interest is the drop in far field stress due to a unit increase in moment caused by the propagation of slip, $\partial\sigma/\partial M_o$ (referred to as the unloading factor). A large unloading factor represents 'stiff' ground conditions and often results in stable fault slip (like displacement controlled boundary conditions in laboratory tests). The unloading factor for the model in Figure 1 is calculated following the procedure outlined in the appendix in Kemeny (1989a), and is given by:

$$\frac{\partial\sigma}{\partial M_o} = -\frac{(1+\nu)}{2\,d\,\sin\beta\cos\beta\,b\,t} \tag{6}$$

Equations (1) through (6) are sufficient to model slip along a normal fault in the Basin and Range. In the next section we model a documented earthquake to estimate some of the important parameters such as the shear fracture energy, and the horizontal stress in the absence of tectonic extension. We then use these parameters to look at faulting at Yucca Mountain.

Example of Hebgen Lake Earthquake

Both for the purposes of demonstrating the usefulness of the model, and estimating some of the unknown parameters, the results developed in the previous section are used to model an actual Basin and Range seismic event. A sequence of large earthquakes occurred in the Hebgen Lake, Montana region beginning on August 18, 1959. The largest earthquake in the sequence, with $M_S = 7.5$, represents the largest earthquake to have occurred in the region in historic time (Doser, 1985). This earthquake is also one of the best documented Basin and Range earthquakes (e.g., Nolan, 1964). Inversion of the body

wave amplitudes have revealed a moment tensor for the largest earthquake that is 84-88% double couple (Doser, 1985), which agrees with the pure double couple assumptions in our model. Short period body wave data indicates that the rupture began on a fault dipping approximately 60^0 near the base of the seismogenic zone (approximately 15 km depth), propagating upwards along a fault with a dip of approximately 50^0. Surface fault scarps indicate a fault width of approximately 19.6 km. Based on these results, we have assumed a plate thickness b of 15 km, width t of 19.6 km, and the normal fault with angle β of 60^0. Other parameters that are fairly well constrained are the elastic properties of the ground, $E = 5 \times 10^{10}$ Pa and $\nu = 0.25$, and an average ground density $\rho g = 20,000$ Pa/m. The unloading factor, given by equation (6), depends on the unknown parameter d. For the Hebgen Lake earthquake, we have set $d = 15$ km, which is consistent with the spacing between large normal faults in the Basin and Range. Also, the initial crack length, l_o, has been set to 15% of the plate width.

The three important parameters that are not well constrained are the shear fracture energy, G_c, the coefficient of friction, μ_f, and the constant relating the horizontal in-situ stress perpendicular to the fault, F. We have made several runs with the model varying these three parameters, starting with realistic values determined from other studies. For instance, for the shear fracture energy, G_c, we start with the value of 10^6 Joules/m^2 that is appropriate for strike slip faulting along the San Andreas. For the initial values for the coefficient of friction, μ_f and horizontal stress factor, F, we have chosen $\mu_f = 0.6$, and F = 0.75.

The results of the model with $G_c = 5 \times 10^7$ J/m^2, $\mu_f = 0.6$, and F = 0.6 (and the remaining parameter values as given above) are presented in Figure 2. Figure 2 is a plot of the tectonic stress, σ, vs. the seismic moment, M_0. This figure describes the motion of the normal fault as the tectonic extension increases, giving both the aseismic and seismic deformation, and giving the seismic source parameters for unstable motion of the normal fault. The best way to understand the results in Figure 2 is to imagine going through an

earthquake cycle, starting with only the gravity stresses and zero tectonic extension ($\sigma = 0$), and looking at the effects of increasing σ. Initially, with $\sigma = 0$, the surfaces of the crack are locked due to the high friction from the gravity forces. As σ is increased, the frictional forces are reduced, and the driving force along the crack is increased. The first effect of this is to unlock the crack faces at some value of σ (calculated from equation 1 with $K_{II} = 0$). Figure 2 shows that this occurs at a σ of 41 bars (point A in the figure). This is the initial frictional constraint, but as we will see, the friction changes as the slip event progresses.

Up to this point there has been no moment since the crack faces were locked. Now, for a further increase in σ, there will be a linear increase in M_0, as given by equation (5) and shown in Figure 2. This linear relation between σ and M_0 is due to the fact that the crack is not propagating, and continues until the stress σ is increased to a point where the crack begins to propagate. This point is calculated from equation (3) with $l = l_0$ and is shown as point B in Figure 2. As the crack propagates, the restriction that $G = G_c$ is maintained as the crack propagates results in a non-linear relationship between σ and M_0, as shown by the nonlinear curve following point B (referred to as the nonlinear stress-moment curve). This nonlinear curve is calculated from the simultaneous solution of equations (3) and (5) as the crack length increases from its initial value of l_0 towards the ground surface.

Whether the crack propagates in a stable or unstable manner depends on the relationship between this nonlinear curve and the unloading of the surrounding ground. Because the ground surrounding the crack is elastic, the unloading of the surrounding ground due to an imposed moment along the crack surfaces will be linear, and is given by the linear line from point B as given by equation (6). For the parameter values used to model the Hebgen Lake earthquake, Figure 2 shows that the crack will initially unload faster than the surrounding ground (nonlinear curve is steeper at point B). Thus excess energy is being supplied to the crack by the surrounding ground, resulting in unstable crack growth. In this case, the crack continues to propagate in an unstable manner all the

way to the ground surface, and the stress drops back to a new frictional level of approximately 20 bars. Note that in other instances, depending on the relationship between the nonlinear stress-moment curve and the unloading factor, stable crack growth can be predicted, or initially stable crack growth that becomes unstable at some value of crack length.

Figure 2 gives the predicted source parameters for this unstable event. The predicted stress drop and moment are the changes in stress and moment that occur from the initiation of crack growth until the crack reaches the ground surface (from point B to point C in Figure 2). As shown in Figure 2, the predicted stress drop and moment are 210 bars and 5 x 10^{26} dyne-cm, respectively, which match with the calculated moment of 1 x 10^{27} dyne-cm and an estimated stress drop of 110 bars made by Doser (1985). Note that the moment and stress drop are related in a linear fashion by the unloading factor. Thus, if the unloading factor is known, and for a measured moment, M_0, the stress drop during unstable rupture can be estimated.

The stress drop that the model predicts represents a drop in the far field tectonic extension. This predicted stress drop is not the same as the stress drop calculated from the equation:

$$\Delta\sigma = \frac{8 M_0}{3 \pi t^2 b} \tag{7}$$

which was used in Doser (1985) to estimate the stress drop for the Hebgen Lake earthquake. Equation (7) is actually not a measure of stress drop, but rather an estimate of the stress at which the rupture initiates, which correlates with point A in Figure 2 (calculated using equation 3). The close agreement between the 'stress drop' measured by equation (7), and the actual drop in the far field stress as given by Figure 2, is due to the fact that for a large normal faulting earthquake, the total far field stress is extinguished in

the ground surrounding the normal fault. This is not the case, for instance, in moderate earthquakes along strike slip faults, where the drop in the far field stress may be only a percentage of the total available stress (see Kemeny, 1989a).

The strain energy change from the beginning of crack growth until the crack reaches the ground surface consists of two parts. The strain energy needed for the crack to grow (G_c x new crack surface area) is proportional to the area inside the nonlinear curve and shown in Figure 2. Because the crack growth was unstable, there is excess energy available for seismic release, and this energy is proportional to the difference between the nonlinear curve and the linear unloading slope, also shown in Figure 2. Thus the nonlinear stress-moment curve divides these two parts of the total energy change.

An important element of the mechanics of slip along faults is the relationship between the nonlinear stress-moment curve and the linear unloading factor. For the case of the model for the Hebgen Lake earthquake, the nonlinear stress-moment curve reaches a maximum and turns around back towards the origin, due primarily to interaction of the normal fault with the ground surface. Because of this interaction, it takes much less energy to meet the $G = G_c$ criterion as the crack extends, and more energy is available for seismic release. A similar effect is found for a rupturing asperity, which is important for strike slip and subduction type earthquakes (e.g., Kanamori, 1986).

Faulting at Yucca Mountain

One of the major unknowns at Yucca Mountain is the possibility of a detachment fault occurring at some depth below the surface. Yucca Mountain is cut by a series of steeply dipping normal faults. Whether or not these normal faults terminate at a shallow detachment surface or propagate to great depths is unresolved at the present time . If these normal faults are associated with a shallow detachment surface at a depth of 2 - 4 km, then the possible moment, stress drop, and energy release could be significantly less than if the normal faults extend to depths of 10 km or more and are linked to movement at

these depths. We analyze this quantitatively by using the model in Figure 1, and using a fault width, *b*, of only 3 km. For this analysis, we use the other parameters as determined from the Hebgen Lake model. The results of this are presented in Figure 3.

The results in Figure 3 indicate a moment of about 4×10^{25} dyne-cm and a drop in the far field stress of approximately 200 bars. This represents an earthquake of much smaller magnitude than the Hebgen Lake earthquake, but with a similar stress drop. Thus from the standpoint of water level changes, the effects should be felt over a smaller area, but the changes near the epicentral region should be of similar magnitude. Da Costa (1964) found that for the Hebgen Lake, 1959 earthquake, ground water changes measuring several feet were measured near the epicenter. Thus changes of at least this magnitude should be expected due to unstable fault motion on the normal faults at Yucca Mountain. Further work estimating the water level changes due to the stress drops given by Figure 3 are presently underway. This does not include the effects of squeezing fluids out of cracks and fault zones and towards the ground surface, as analyzed by Sibson (1982), which will also be studied further. Also, further work needs to be conducted on the coupled effects of stress changes, pore pressure changes, and groundwater flow.

References

Da Costa, J. A. 1964. Effect of Hebgen Lake earthquake on water levels in wells in the United States. U.S. Geological Survey Professional Paper 435-O, U.S.G. S., Washington, D.C.

Davis, G. A., and Lister, G. S. 1988. Detachment faulting in continental extension; perspectives from the southwestern U.S. cordillera. Geological Society of America, Special Paper 218, 133-159.

Detournay, E., and Cheng, A. H-D. 1988. Poroelastic response of a borehole in a non-hydrostatic stress field. *Int. J. Rock Mech. Min. Sci. & Geomech. Abstr.* **25**, 171-182.

Doser, D. I. 1985. Source parameters and faulting processes of the 1959 Hebgen Lake, Montana, earthquake sequence. *J. Geophys. Res.* **90**, 4537-4555.

Doser, D. I., and Smith, R. B. 1985. Source parameters of the 28 October 1983 Borah Peak, Idaho, earthquake from body wave analysis. *Bull. Seism. Soc. Am.* **75**, 1041-1051.

England, P. and Jackson, J. 1987. Migration of the seismic-aseismic transition during uniform and nonuniform extension of the continental lithosphere. *Geology* **15**, 291-294.

Hamilton, W. 1987. Crustal extension in the Basin and Range province, southwestern United States. *From* Coward, M. P., Dewey, J. F., and Hancock, P. L. (eds), *Continental Extensional Tectonics*, Geological Society Special Publication No. 28, 155-176.

Jaeger, J. C. and Cook, N. G. W. 1979. *Fundamentals of Rock Mechanics*, Chapman and Hall, London.

Kanamori, H. 1986. Rupture processes in subduction-zone earthquakes, *Ann. Rev. Earth Plan. Sci.*, **14**, 293-322.

Kemeny, J. M. 1989a. The mechanics of asperity failure under realistic boundary conditions. To be published.

Kemeny, J. M. 1989b. The origin of slip weakening along faults in rock. To be published.

Kemeny, J. M. and Cook, N. G. W. 1987. Determination of rock fracture parameters from crack models for failure under compression. 28th U.S. Rock Mechanics Symposium. A.A. Balkema, Rotterdam, 367-374.

Lawn, B. R. and Wilshaw, T. R. 1975. *Fracture of Brittle Solids*. Cambridge University Press, London.

Li, V. C., Seale, S. H., and Cao, T. 1987. Postseismic stress and pore pressure readjustment and aftershock distributions. *Tectonophysics* **144**, 37-54.

Lin, J. and Parmentier, E, M. 1988. Quasistatic propagation of a normal fault: a fracture mechanics model. *J. Struct. Geology* **10**, 249-262.

McGarr, A. 1988. On the state of lithospheric stress in the absence of applied tectonic forces. *J. Geophys. Res.* **93**, 13609-13617.

Nolan, T. B. 1964. The Hebgen Lake, Montana Earthquake of August 17, 1959. U.S. Geological Survey Professional Papers 435A-T, U.S.G. S., Washington, D.C.

Rice, J. R., and Cleary, M. P. 1976. Some basic stress diffusion solutions for fluid-saturated elastic porous media with compressible constituents. *Rev. Geophys. and Space Phys.* **14**, 227-241.

Scott, R. B. 1986. Extensional tectonics at Yucca Mountain, southern Nevada, *Geological Society of America Abstracts with Programs*, **18**, p. 411.

Sibson, R. H. 1981. Fluid flow accompanying faulting: field evidence and models. *From* Simpson, D. W. and Richards, P. G. (eds), *Earthquake Prediction: an International Review*, AGU, Washington, D. C.

Sibson, R. H. 1982. Earthquake rupturing as a mineralizing agent in hydrothermal systems. *Geology* **15**, 701-704.

Smith, R. B., and Bruhn, R. L. 1984. Intraplate extensional tectonics of the eastern Basin-Range: Inferences on structural style from seismic reflection data, regional tectonics, and thermal-mechanical models of brittle-ductile deformation, *J. Geophysical Res.*, **89** 5733-5762.

Stein, R. S., and Barrientos, S. E. 1985. Planar high-angle faulting in the Basin and Range: geodetic analysis of the 1983 Borah Peak, Idaho, earthquake. *J. Geophys. Res.* **90**, 11355-11366.

Tada, H., Paris, P. C., and Irwin, G. R. 1973. *The Stress Analysis of Cracks Handbook*, Del Research Corp., Hellertown.

Wong, T.-f. 1982. Shear fracture energy of Westerly granite from post-failure behavior. *J. Geophys. Res.* **87**, 990-1000.

Wong T.-f. 1986. On the normal stress dependence on the shear fracture energy. In *Earthquake Source Mechanics*, Geophysical Monograph 37, AGU, Washington, D. C.

Zoback, M. L., Anderson, R. E., and Thomson, G. A. 1981. Cainozoic evolution of the state of stress and style of tectonism of the Basin and Range province of the western United States. *Phil. Trans. R. Soc. Lond.* A **300**, 407-434.

Zoback, M. L. and Zoback, M. 1980. State of stress in the conterminous United States. *J. Geophys. Res.* **85**, 6113-6156.
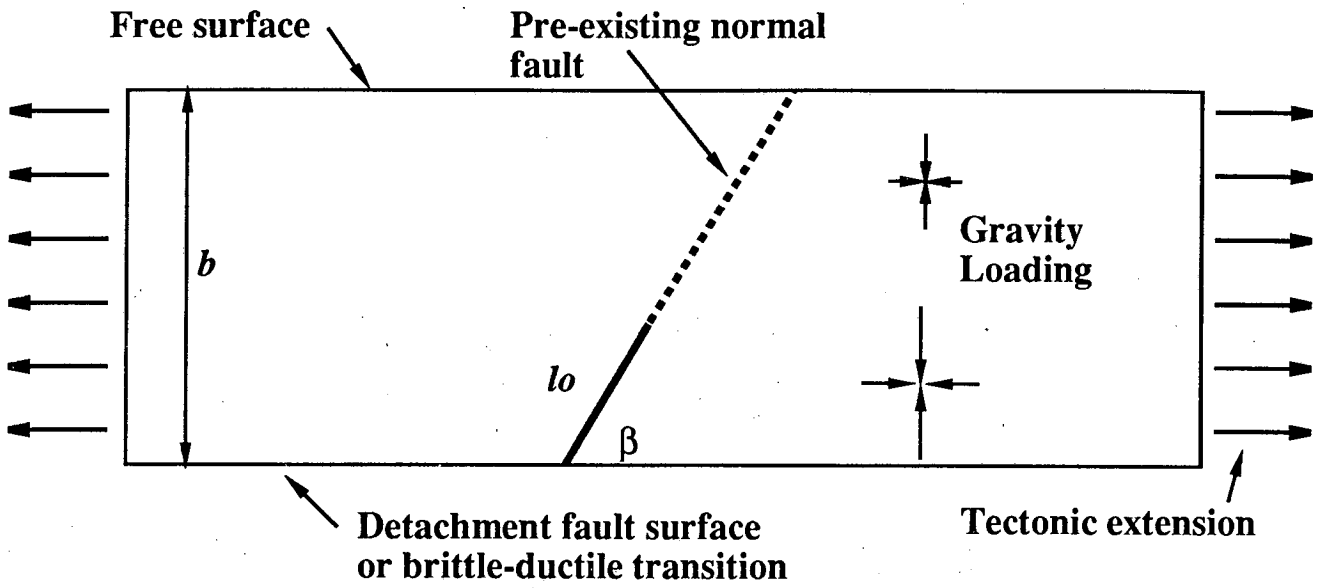
Figure 1. Mechanical model for normal faulting in the Basin and Range. The normal fault is represented by the angle crack, and a slip event along the normal fault is modelled as the propagation of the crack from its initial position towards the top of the plate.
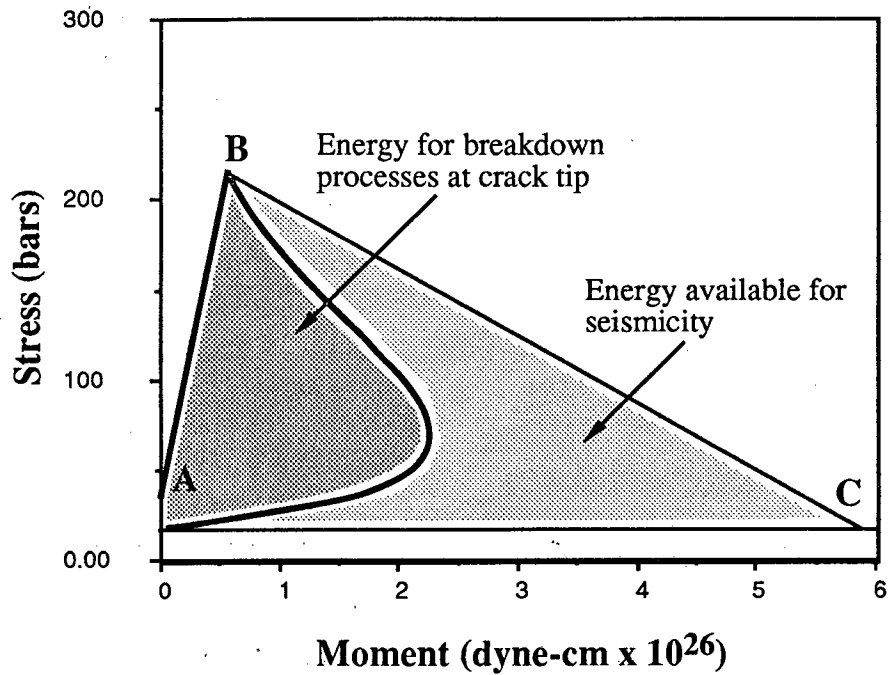
Figure 2. Analysis of the Hebgen Lake, 1959, earthquake using the model in Figure 1 (parameter values given in text). Slip between the crack surfaces initiates at point A, and crack propagation starts at point B. Unstable rupture (point B to point C) results in a moment of about 5 x 10²⁶ dyne-cm and a stress drop of about 200 bars.
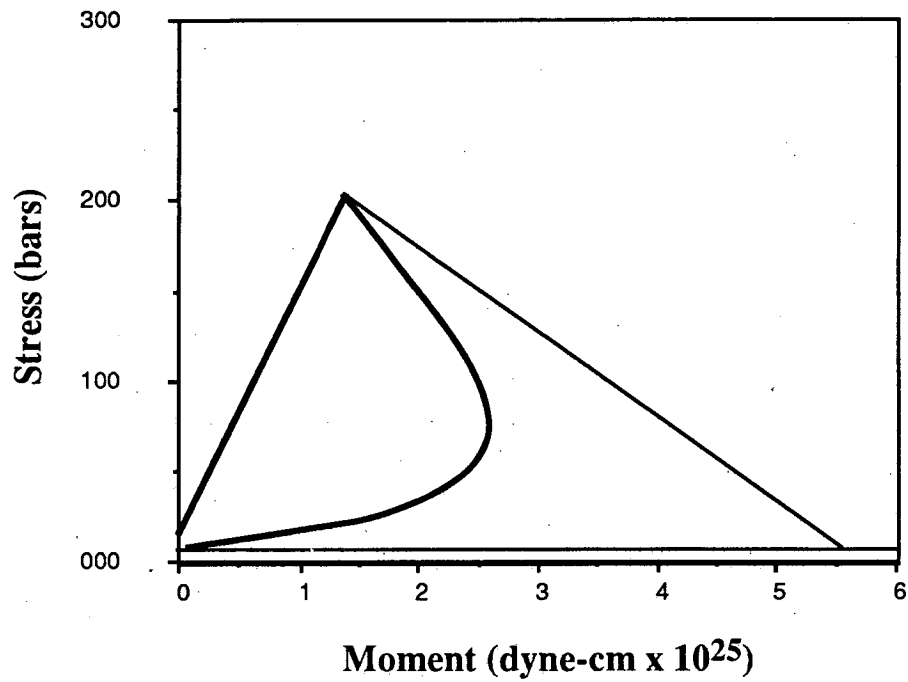
Figure 3. Analysis of faulting at Yucca Mountain using the parameter values from the Hebgen Lake model, except that a detachment fault is placed at a depth of 3 km. Unstable rupture results in a moment of about 4×10^{25} dyne-cm and a stress drop of about 200 bars.

GRP Project Publications List - Alphabetical

Asch, T., and Morrison, H. F., "Mapping and monitoring electrical resistivity with surface and subsurface electrode arrays," Geophysics, Vol. 54, No. 2, Feb. 1989.

Carnahan, C. L., "Coupling of precipitation/dissolution reactions to mass diffusion", report LBL-26183, Chemical Modeling in Aqueous Systems II Symposium, 196th National Meeting of American Chemical Society, Division of Geochemistry, Los Angeles, CA, Sept. 25-30, 1988.

Daley, T. M., McEvilly, T. V., and Majer, E. L., "Multiply-polarized shear-wave VSPs from the Cajon Pass drillhole," report LBL-25289, submitted to Geophysical Research Letters, 1988.

Ewy, R. T., Cook, N. G. W., and Myer, L. R., "Hollow cylinder tests for studying fracture around underground openings," report LBL-25308, 29th U.S. Symposium on Rock Mechanics, University of Minnesota, 1988.

Ewy, R. T., Kemeny, J., Zheng, Z., and Cook, N. G. W., "Generation and analysis of stable excavation shapes under high rock stresses," report LBL-22747, Proceedings of 6th International Congress on Rock Mechanics, Montreal, Canada, Vol. II, pp. 875-881, 1987.

Flueh, E. R., Mooney, W. D., Fuis, G. S., and Ambos, E. L., "Crustal structure of the Chugach Mountains, Southern Alaska: A study of pegleg multiples from a low velocity zone," report LBL-24699, submitted to Journal of Geophysical Research, 1988.

Flueh, E. R., and Okaya, D. A. "Near-vertical and intermediate offset seismic reflection data from west of the Whipple Mountains, SE California," report LBL-24641, submitted to Journal of Geophysical Research, 1988.

Hopkins, D. L., Cook, N. G. W., and Myer, L. R., "Fracture stiffness and aperture as a function of applied stress and contact geometry," report LBL-25312, 28th U.S. Symposium on Rock Mechanics, Tucson, AZ, June 29-July 1, 1987.

Kemeny, J., and Cook, N. G. W., "Frictional stability of heterogeneous surfaces in contact," report LBL-25313, Proceedings of the 27th U.S. Rock Mechanics Symposium, Tuscaloosa, AL, 1986.

Kemeny, J., and Cook, N. G. W., "Crack models for the failure of rocks in compression," report LBL-25311, Proceedings 2nd International Conference Constitutive Laws for Engineering Materials, C.S. Desai et al., editors, Elsevier Science Publ. Co., Inc., NY, pp. 879-887, 1987.

Kemeny, J., and Cook, N. G. W., "The origin of slip weakening along faults in rocks," report LBL-25306, submitted to Mechanics of Materials.

Kemeny, J., and Cook, N. G. W., "Constraints on moment, stress drop and strain energy release due to slip weakening," report LBL-25306, in preparation.

Meike, A., "Specimen cage modification for TEM in-situ shearing, report LBL-24145, Proceedings Materials Research Society, Fall Meeting, 1988.

Moreno, L., Tsang, Y. W., Tsang, C. F., Hale, F. V., and Neretnieks, I., "Flow and tracer transport in a single fracture: A stochastic model and its relation to some field observations," report LBL-25049, Water Resources Research, Vol. 24, No. 12, pp. 2033-2048, 1988.

Muralidhar, K., and Long, J. C. S., "A scheme for calculating flow in fractures using numerical grid generation in three-dimensional domains of complex shapes," report LBL-24453, September 1987.

Pyrak-Nolte, L. J., and Cook, N. G. W., "Fluid percolation through single fractures," Geophysical Research Letters, Vol. 15, No. 11, pp. 1247-1250, 1988.

Pyrak-Nolte, L. J., Cook, N. G. W., and Myer, L. R., "Seismic visibility of fractures," report LBL-25310, Proceedings of 28th U. S. Symposium on Rock Mechanics, Tucson, AZ, pp. 47-51, 1987.

Pyrak-Nolte, L. J., Myer, L. R., and Cook, N. G. W., "Transmission of seismic waves across single fractures," report LBL-26616, to be submitted to JGR.

Pyrak-Nolte, L. J., Myer, L. R., Cook, N. G. W., and Witherspoon, P. A., "Hydraulic and mechanical properties of natural fractures in low permeability rock," report LBL-22718, Proceedings of 6th International Congress on Rock Mechanics, Montreal, Canada, Vol. 1, pp. 225-232, 1987.

Tsang, C. F., "Tracer transport and model validation," Invited Paper, American Nuclear Society Annual Meeting, San Diego, California, June 13-16, 1988.

Tsang, C. F., Tsang, Y. W., and Hale, F. V., "Tracer transport in fractured rocks," report LBL-25657, Invited Paper, Proceedings of International Conference on Flow in Fractured Rocks, Atlanta, Georgia, May 16-18, 1988.

Tsang, Y. W. and Hale F. V., "A study of the application of mercury porosimetry method to a single fracture," report LBL-25489, Proceedings of International Conference on Flow in Fractured Rocks, Atlanta, Georgia, May 16-18, 1988.

Tsang, Y. W., and Tsang, C. F., "Channel model of flow through fractured media," report LBL-21310, Water Resources Research, Vol. 23, No. 3, pp. 467-479, 1987.

Tsang, Y. W., Tsang, C. F., Hale, F. V., Moreno, L., and Neretnieks, I., "Channeling characteristics of flow and solute transport through a rough-surfaced fracture," report LBL-23195, June 1987.

Tsang, Y. W., Tsang, C. F., Neretnieks, I., and Moreno, L., "Flow and tracer transport in fractured media--A variable-aperture channel model and its properties," report LBL-25048, Water Resources Research, Vol. 24, No. 12, pp. 2049-2060, 1988.

Wollenberg, H. A., and Flexser, S., "Evidence for mobility of uranium in fractured, heated rock," report LBL-26137, submitted to Applied Geochemistry, 1988.

Zheng, Z., Kemeny, J., and Cook, N. G. W., "Analysis of wellbore breakouts," report LBL-23941, submitted to Journal of Geophysical Research, 1987.

Zheng, Z., Myer, L. R., and Cook, N. G. W., "Borehole breakout and stress measurements," report LBL-25655, Proceedings, 29th U.S. Symposium on Rock Mechanics, University of Minnesota, 1988.

GRP Project Publications List - Chronological

1. Kemeny, J., and Cook, N. G. W., "Frictional stability of heterogeneous surfaces in contact," report LBL-25313, Proceedings of the 27th U.S. Rock Mechanics Symposium, Tuscaloosa, AL, 1986.

2. Tsang, Y. W., and Tsang, C. F., "Channel model of flow through fractured media," report LBL-21310, Water Resources Research, Vol. 23, No. 3, pp. 467-479, 1987.

3. Tsang, Y. W., Tsang, C. F., Hale, F. V., Moreno, L., and Neretnieks, I., "Channeling characteristics of flow and solute transport through a rough-surfaced fracture," report LBL-23195, June 1987.

4. Ewy, R. T., Kemeny, J., Zheng, Z., and Cook, N. G. W., "Generation and analysis of stable excavation shapes under high rock stresses," report LBL-22747, Proceedings of 6th International Congress on Rock Mechanics, Montreal, Canada, Vol. II, pp. 875-881, 1987.

5. Hopkins, D. L., Cook, N. G. W., and Myer, L. R., "Fracture stiffness and aperture as a function of applied stress and contact geometry," report LBL-25312, 28th U.S. Symposium on Rock Mechanics, Tucson, AZ, June 29-July 1, 1987.

6. Kemeny, J., and Cook, N. G. W., "Crack models for the failure of rocks in compression," report LBL-25311, Proceedings 2nd International Conference Constitutive Laws for Engineering Materials, C.S. Desai et al., editors, Elsevier Science Publ. Co., Inc., NY, pp. 879-887, 1987.

7. Muralidhar, K., and Long, J. C. S., "A scheme for calculating flow in fractures using numerical grid generation in three-dimensional domains of complex shapes," report LBL-24453, September 1987.

8. Pyrak-Nolte, L. J., Cook. N. G. W., and Myer, L. R., "Seismic visibility of fractures," report LBL-25310, Proceedings of 28th U. S. Symposium on Rock Mechanics, Tucson, AZ, pp. 47-51, 1987.

9. Pyrak-Nolte, L. J., Myer, L. R., Cook, N. G. W., and Witherspoon, P. A., "Hydraulic and mechanical properties of natural fractures in low permeability rock," report LBL-22718, Proceedings of 6th International Congress on Rock Mechanics, Montreal, Canada, Vol. 1, pp. 225-232, 1987.

10. Zheng, Z., Kemeny, J., and Cook, N. G. W., "Analysis of wellbore breakouts," report LBL-23941, submitted to Journal of Geophysical Research, 1987.

11. Daley, T. M., McEvilly, T. V., and Majer, E. L., "Multiply-polarized shear-wave VSPs from the Cajon Pass drillhole," report LBL-25289, submitted to Geophysical Research Letters, 1988.

12. Ewy, R. T., Cook, N. G. W., and Myer, L. R., "Hollow cylinder tests for studying fracture around underground openings," report LBL-25308, 29th U.S. Symposium on Rock Mechanics, University of Minnesota, 1988.

13. Flueh, E. R., and Okaya, D. A. "Near-vertical and intermediate offset seismic reflection data from west of the Whipple Mountains, SE California," report LBL-24641, submitted to Journal of Geophysical Research, 1988.

14. Moreno, L., Tsang, Y. W., Tsang, C. F., Hale, F. V., and Neretnieks, I., "Flow and tracer transport in a single fracture: A stochastic model and its relation to some field observations," report LBL-25049, Water Resources Research, Vol. 24, No. 12, pp. 2033-2048, 1988.

15. Tsang, Y. W., Tsang, C. F., Neretnieks, I., and Moreno, L., "Flow and tracer transport in fractured media--A variable-aperture channel model and its properties," report LBL-25048, Water Resources Research, Vol. 24, No. 12, pp. 2049-2060, 1988.

16. Flueh, E. R., Mooney, W. D., Fuis, G. S., and Ambos, E. L., "Crustal structure of the Chugach Mountains, Southern Alaska: A study of pegleg multiples from a low velocity zone," report LBL-24699, submitted to Journal of Geophysical Research, 1988.

17. Meike, A., "Specimen cage modification for TEM in-situ shearing, report LBL-24145, Proceedings Materials Research Society, Fall Meeting, 1988.

18. Wollenberg, H. A., and Flexser, S., "Evidence for mobility of uranium in fractured, heated rock," report LBL-26137, submitted to Applied Geochemistry, 1988.

19. Zheng, Z., Myer, L. R., and Cook, N. G. W., "Borehole breakout and stress measurements," report LBL-25655, Proceedings, 29th U.S. Symposium on Rock Mechanics, University of Minnesota, 1988.

20. Pyrak-Nolte, L. J., Myer, L. R., and Cook, N. G. W., "Transmission of seismic waves across single fractures," report LBL-26616, to be submitted to JGR.

21. Kemeny, J., and Cook, N. G. W., "The origin of slip weakening along faults in rocks," report LBL-25306, submitted to Mechanics of Materials.

22. Kemeny, J., and Cook, N. G. W., "Constraints on moment, stress drop and strain energy release due to slip weakening," report LBL-25306, in preparation.

23. Tsang, Y. W. and Hale F. V., "A study of the application of mercury porosimetry method to a single fracture," report LBL-25489, Proceedings of International Conference on Flow in Fractured Rocks, Atlanta, Georgia, May 16-18, 1988.

24. Tsang, C. F., Tsang, Y. W., and Hale, F. V., "Tracer transport in fractured rocks," report LBL-25657, Invited Paper, Proceedings of International Conference on Flow in Fractured Rocks, Atlanta, Georgia, May 16-18, 1988.

25. Tsang, C. F., "Tracer transport and model validation," Invited Paper, American Nuclear Society Annual Meeting, San Diego, California, June 13-16, 1988.

26. Carnahan, C. L., "Coupling of precipitation/dissolution reactions to mass diffusion", report LBL-26183, Chemical Modeling in Aqueous Systems II Symposium, 196th National Meeting of American Chemical Society, Division of Geochemistry, Los Angeles, CA, Sept. 25-30, 1988.

27. Pyrak-Nolte, L. J. and Cook, N. G. W., "Fluid percolation through single fractures," Geophysical Research Letters, Vol. 15, No. 11, pp. 1247-1250, 1988.

28. Asch, T., and Morrison, H. F., "Mapping and monitoring electrical resistivity with surface and subsurface electrode arrays," Geophysics, Vol. 54, No. 2, Feb. 1989.

Hydrologic Properties of Fault Zones and Fractured Rock,
Evidence for Shallow Groundwater at Yucca Mountain, Nevada

H. Wollenberg, C. Carnahan, I. Javandel, E. Majer, and J. Wang

Earth Sciences Division

Lawrence Berkeley Laboratory

Introduction

It is proposed to drill and continuously core inclined boreholes from the surface to intersect the Ghost Dance and Solitario Canyon faults at Yucca Mountain. The principal objective is to understand the hydrologic implications of faults that cut, or are in close proximity to the candidate repository horizon. These inclined boreholes will not penetrate the repository horizon, but will intersect the faults in the welded Topopah Springs tuff and in the overlying bedded and Tiva Canyon tuffs. To determine if fault zones have significantly different characteristics from tuff units, detailed examinations will be made of mineralogy and physical and hydrological properties of tuff and fault-zone core, and cross-hole hydrological and seismologic testing will be conducted. Drilling and testing of these boreholes should be completed before the sinking of the exploratory shaft and testing of deeper units. The boreholes will provide important data on fault characteristics above the candidate horizon, and will also provide valuable experience in testing the fault-bounded hydrologic systems, so that later examination of deeper units from the repository horizon can then be properly designed and performed. The studies of rock units and the fault zones above the repository horizon will determine if the faults are main channels for the movement of water from the surface to the water table or if the net infiltration is mainly through the tuff units. Examination of fault zone material and geochemical analyses will also determine whether the fault zones were channels for circulation of groundwater to shallow depths in the past.

Rationale

The work proposed here is considered to be an important part of the characterization of the Yucca Mountain site, in that data on properties of fault zones that transect the site are needed in site characterization, especially to address Performance Issues 1.1 and 1.6, to determine if the zones are potential conduits for ingress of fluids to the repository horizon, or conversely, for movement of fluids away from the horizon. In this respect, these proposed studies would complement the characterization of the unsaturated zone percolation, described in NNWSI - USGS Study Plan 8.3.1.2.2.4, where radial holes from the exploratory shaft will investigate deeper zones of the Ghost Dance fault. The proposed work, and the subsequent investigations from the exploratory shaft would also provide an assessment of the nature of material in the fault zones and possible evidence of past intermediate-depth and near-surface circulation of groundwater in today's vadose zone. Because the proposed work is based on drilling from the surface, it could begin relatively quickly, and results would be available to help in detailed planning of investigations from the exploratory shaft.

Setting

The Yucca Mountain block is bounded on the west by the Solitario Canyon Fault and on the east by a number of faults. Among these, the Ghost Dance Fault, inside the proposed repository area, will be of major hydrological concern if fault flow is an important transport mechanism. The generally eastward dip of 5 to 7° (Scott and Bonk, 1984) of stratigraphic units at Yucca Mountain has been suggested as a mechanism to divert some of the water from dispersed vertical flows through the tuff units to concentrated flow through a localized fault zone (Montazer and Wilson, 1984; Rulon et al., 1986). Since the Ghost Dance Fault is inside the Yucca Mountain repository block, significant fault flow would result in a potentially reduced ground water travel time from the repository to the water table. There are essentially no data on the

material properties of the fault to determine if it is indeed a conduit for relatively rapid ground water movement under partially saturated conditions. Equally important, if the Solitario Canyon fault and its associated breccia zone are sufficiently permeable, they could introduce fluids into the updip zone of the repository horizon.

In modeling the hydrology of Yucca Mountain, it is important to assess the impacts of faults that traverse the alternating tuff layers. If faults are barriers to fluid flow, they will partition the system into separate hydrologic blocks, and study can be focused on flows through the interior of blocks. If faults are the main conduits for fluid flow, then focus should be on the fault flow. In saturated systems, we have a clear distinction between these two possibilities. A closed fault is treated as a no-flow boundary, and an open fault can be treated as a constant potential boundary if it is connected to a constant-head reservoir.

In partially saturated systems, there may not be such a clear distinction between an open and a closed fault. Three possibilities are considered:

1. If a fault zone is breccia-filled, it might have very coarse openings that can be easily drained. If the openings are dry, water cannot be transported. However, a dry opening is not a barrier to fluid flow. If water enters locally, and saturates the opening, it will have high permeability and offer low resistance to fluid movement. Under partially saturated conditions, an "open" fault becomes a passive boundary which can transport water if water enters it, but it cannot retain water since there is only a very weak capillary force to hold water in large openings (Wang and Narasimhan, 1987).

2. If a fault is sealed with gouge and fine-grained materials, it can retain water and may even attract water with the strong capillary force associated with small openings. On the other hand, small openings have low permeability

and cannot be good conduits for transporting fluid. Under partially saturated conditions, a "closed" fault becomes a relatively wet zone that passively retains water in nearly static conditions.

3. There is a third possibility that the fault zone may have a combination of saturated and unsaturated characteristics. If the fault material can maintain both strong capillary attractive force and large permeability, then the fault can pull water away from the formation and transport it quickly away from the system. We cannot rule out the existence of such a unique combination wherein fault flow would control the partially saturated hydrology.

Downward movement of water along a fault is controlled by two important parameters: the permeability of the fault, and the magnitude of the resultant downward forces acting on the water. Forces acting on a water particle include gravitational force and surface interaction forces between water and the material coating the surfaces of the fault. Often geological materials are amenable to wetting where there is an affinity of water molecules to attach to the rock surface. Under this condition, the downward components of the resultant forces is initially very small and water is sucked into the rock matrix by the capillary forces and prohibited from downward movement. This condition continues until the rock in the neighborhood of the fault reaches a saturation level at which capillary forces are reduced, and downward forces become large enough to let water move downward. The actual depth of penetration of water in the fault depends on the amount of water entering the fault, the coating materials and the rock microstructure in the vicinity of the fault.

If the rock in the fault planes is covered with material that repels water molecules, full gravitational force acts on the water particles and water moves downward, provided it is not trapped in some micropores in the fault zone. (A good example of this condition is a potted plant whose soil has been caked and has developed some cracks. When watered, water immediately gushes out from the bottom of the pot

without reaching the root system or wetting a major part of the soil.) Therefore, to evaluate the capability of the fault zone to conduct water in the saturated zone, one needs to determine both the permeability of the fault zone and the type of material present on the surfaces of the fault planes to evaluate their wettability properties and microstructures.

The proposed inclined holes drilled from the surface to penetrate the tuff units and to intercept the faults will allow collection of tuff and fault samples, in order to compare the characteristics between the formation tuffs with the fault zone materials. With these comparisons, one can then distinguish whether the faults have open, closed, or combined characteristics.

ACTIVITIES

Task 1: Drilling/Coring

It is proposed to drill at least three sets of holes, inclined 30 to 50° and 100 to 300 m deep, to intercept the Ghost Dance fault, as shown on Figure 1. Each set would consist of two holes in a vertical plane. These three sets would extend into Tiva Canyon, Paintbrush, and Topopah Spring units, respectively. The angle of incli- nation of these holes would be selected such that their separations be appropriate for cross-hole investigations. Similarly, a set of two holes, inclined 30 to 40° and ~ 300 m. deep are proposed to be drilled across the Solitario Canyon fault and the breccia zone immediately to its west. All the holes will extend beyond the fault intersection points a distance sufficient to obtain unaffected tuff samples and to allow cross-hole testing across the fault faces. Depending on initial results of cross-hole tests, addi- tional holes might be drilled to allow interlayer and intralayer tests.

Two drilling options are considered: ı) All holes could be continuously cored with wireline core barrel retrieval. PQ hole size ($\approx$ 4.8 inch diameter) will provide sufficient space for downhole packer assemblies and 3.3-inch-diameter core. 2)

Alternatively, holes could be reverse-circulation rotary drilled using air (roughly 1/3 the cost of coring) to the vicinity of the fault zones, casing set, and then cored through the zones to total depth (L. Pisto, Tonto Drilling Co., private communication, 3/1/88). In this respect, to determine the casing point, it would be advisable to continuously core the first of each set of inclined holes, then use the combination rotary/coring on subsequent holes.

Task 2: Hydrological Field Measurements

The Ghost Dance Fault is located within the repository area, whereas the Solitario Canyon Fault and its accompanying brecciated zone are beyond the limits of this area. Because there is a concern about the use of water for early characterization activities within the repository area, different types of tests are being proposed for each of the faults.

Ghost Dance Fault Tests

Since the Ghost Dance fault holes would penetrate both the upper welded Tiva Canyon tuff and part of the welded Topopah Spring unit, the hydrological and geochemical characteristics of the core will be studied to determine if properties of these two welded units are significantly different. The nonwelded bedded unit, sandwiched between these two welded units, has been suggested to be a main conduit for water transport laterally from dispersed infiltration through the Tiva Canyon unit to concentrated flow through the fault. If the non-welded, bedded unit acts as a drainage diverter, we should detect significant differences between the Tiva Canyon and Topopah Spring, since the Tiva Canyon probably has more water flowing through it, while the Topopah Spring has lower net flow with a large fraction of infiltration diverted by the overlying bedded unit. The Ghost Dance holes would also investigate if fracture flow is significant in the Tiva Canyon and Topopah Spring. Modeling results based on

limited laboratory data suggest that fracture flow may occur in the Tiva Canyon and that matrix flow dominates in the Topopah Spring, under ambient partially saturated conditions (Wang and Narasimhan, 1985, 1986).

It is proposed to equip each hole with several inflatable packers to isolate a few intervals on both sides of the fault zone, as well as one intersecting the fault zone itself. During the period that water tests are not recommended, pressure transducers would be installed in all the isolated intervals. Time variation of air pressure is then measured both at the surface and within all the isolated intervals. In general, permeability to air of the materials between the ground surface and the borehole at a given isolated interval controls the response of the transducers due to the barometric pressure changes (Weeks, 1978). Therefore, any significant difference between the response of transducers at the fault zone with those deep in the rock matrix should be indicative of the permeability contrast between the fault and the rock matrix.

At the stage when hydrological tests become permissible, water could be injected into one of the isolated intervals in the upper borehole of the lowest three sets of slanted holes. The time variation of pressure within all isolated intervals in the same borehole and the one below would then be monitored. This test would be repeated in all other isolated intervals of the same hole. The results of these tests should identify any major contrast between the permeability of the fault and the rock matrix in the vicinity of the fault in the upper part of the welded Topopah Spring.

This procedure may then be carried out at the next pair of holes in the overlying Paintbrush and Tiva Canyon tuffs, respectively.

In addition to the pressure transient tests, tracer tests may also be carried out to estimate travel time along various sections of the fault and the rock matrix adjacent to the fault.

Solitario Canyon Fault and Brecciated Zone Tests

Perhaps the most important controlling factors for pre-waste-emplacement ground-water travel time (Issue 1.6) at Yucca Mountain are the availabity of a sufficient quantity of water anywhere in the disturbed zone, and the hydraulic conductivity of the rock between that particular area and the water table. In the unsaturated medium below the disturbed zone at Yucca Mountain, hydraulic conductivity could be a strong function of the moisture content that in turn is directly related to the quantity of the water being supplied to that volume from various sources.

The Solitario Canyon Fault and the extensive brecciated zone assoicated with it could provide an important pathway for the surface water to reach the respository level at the disturbed zone. Therefore, it is very important to address two questions: (1) How much water effectively enters the Solitario Canyon Fault zone and associated brecciated zone and manages to pass the root zone? and (2) How fast does this water travel downward to the disturbed zone?

Unfortunately, very little or no direct data are available on the spatial or temporal distribution of the net infiltration at Yucca Mountain (SCP, vol. II, page 3-202). Waddell et al. (1984) have estimated a moisture flux of about 0.5 mm/yr through the alluvium in Yucca Flat, about 40 km northeast of Yucca Mountain. Another estimate of moisture flux is given by Case et al. (1984). Their estimate is about 1 mm/yr at Frenchman Flat, ~ 40 km east of Yucca Mountain. In a more recent article, Montazer et al. (1988) have estimated a rate of 0.1 to 0.5 mm/yr for water fluxes in the matrix of the repository host-rock.

The Solitario Canyon Fault and the associated brecciated zone are located in a valley that collects runoff from a substantial area underlain by tuff units that dip east-ward beneath Yucca Mountain, and the average annual precipitation in this area is about 150 to 160 mm/yr. We therefore believe that it is important that net infiltration in this area be directly measured. Along with the inclined holes discussed below, we

propose that a shallow (~ 10 m) shaft be constructed adjacent to, and on the east side of the Solitario Canyon Fault and that several horizontal holes be drilled from a ~ 15 m-long horizontal drift constructed parallel to the fault from the bottom of the shaft. These holes should be equipped for measurements of the net infiltration rate. On the surface, rainfall similar to extreme scenarios (intensity-duration-depth) would be simulated. The catchment area above the section of interest should be calculated and the runoff corresponding to the extreme scenario should be introduced.

At least two slanted holes should be drilled from the surface to intercept the Solitario Canyon Fault zone. Both holes would be equipped with several inflatable packers to isolate a few intervals along the faults within the brecciated zone and in the welded Topapah Spring. Those isolated intervals will be initially equipped with pressure transducers to monitor variations of air pressure. Any significant difference between air permeability of the fault zone or brecciated interval and that of the intact rock may be reflected in the response observed from various packed-off intervals.

Once the air pressure monitoring is complete, one could proceed with injection of water and tracers from the isolated intervals from the upper hole, and monitoring the pressure response and travel time at the isolated intervals in the lower hole. Data from these tests should provide an indication of major changes in the saturated hydraulic conductivity between the intact rock, fault zone and brecciated area. One may also be able to estimate the saturated hydraulic conductivity of the brecciated zone and the Solitario Canyon Fault.

Task 3: Seismic Investigations

In field and laboratory studies to date, seismic researchers have seen that fracture sets, and even individual fractures, have a dramatic effect on the amplitude and velocity of seismic waves as well as the polarity of the waves. The goal of the planned Vertical Seismic Profiling (VSP) field studies at Yucca Mountain is to determine the

applicability of seismic profiling techniques, and if appropriate, to refine and apply these techniques to mapping fracture properties between boreholes and underground workings. If successful, this could provide a method to extrapolate the geology known in the boreholes and shafts to the entire repository, something that must be accomplished before licensing. The first planned seismic field work is a multi-offset, multi-source, 3-component VSP in well G4. The objective is to collect enough ray paths to tomographically map the Ghost Dance fault in the vicinity of G-4 and any other features that may also be detectable. A detailed description of the work is in the Scientific Investigation Plan USGS-SIP-6941G-02. A crucial issue in this work is the verification of the effect of the faults on the propagation of the seismic waves and on the link between the seismic results and the hydrologic regime.

As part of the work proposed here, cross-hole seismic tomography would be carried out in the inclined boreholes across the fault zones. This would provide a means to calibrate the VSP seismic results as well as to extrapolate the fault properties between the boreholes. Because permeability measurements would be carried out in the boreholes it would also be possible to correlate the seismic results to the hydrologic results. The work would be done in a fractured/faulted zone and in an intact zone for comparison. Core would be measured for seismic properties in order to further calibrate the seismic results.

Task 4: Geochemical Studies

Geochemical studies would be conducted both on the host rocks adjacent to the faults, and on any fault-filling materials. Much may be learned about the age of the faults, times when movements occurred along them, whether the faults were subject to hydrothermal convection or acted as channelways for downward moving meteoric water, and the times when such water movement occurred.

The strategy for pursuing geochemical and geochronological studies depends greatly on the condition of the faults at the borehole intersections, and the success of core recovery at the fault interfaces. It is assumed here that continuous core will be recovered across the fault zone in each borehole, but that cores of matrix blocks adjacent to the faults will not be available from all boreholes. Cores equivalent to one complete hole will be sampled at each fault. It is anticipated that drilling methods may preclude recovery and analysis of vadose water in matrix blocks.

Evidence for multiple generations of slickensiding or cataclasis in fault fillings will be searched for and interpreted in relation to isotopic and geochronologic measurements. In particular, clinoptilolite and heulandite, the most commonly occurring zeolites at NTS, are affected by slickensiding. Occurrences of these minerals will be dated by the K-Ar method.

Surface manifestations of some faults at NTS have revealed extensive void filling by calcite and kaolinite. Questions have been raised as to whether the calcite was of pedogenic or hydrothermal origin (Szabo, 1984). If the fault plane rocks contain secondary calcite, both $^{13}C/^{12}C$ and $^{18}O/^{16}O$ isotopic studies will be conducted on the calcite to determine whether these isotopes indicate a low temperature meteoric (and biogenic) origin, or whether they have a hydrothermal signature. Similar studies with respect to D/H and $^{18}O/^{16}O$ will be made on smectites and zeolites where possible. If fluid inclusions are present in the calcite they will be examined for their filling temperatures and chemistry. Measurements of ^{14}C content of pedogenic calcite will be made to determine the time since its formation. Multiple generations of pedogenic calcite precipitating in voids could provide some evidence of prior climatic history of the region and indicate whether water movement down the fault planes was a common occurrence in the past.

If hydrothermal activity is suggested by preliminary isotopic studies, further investigation of ^{226}Ra daughter products will be made, to provide evidence of deep

seated leaching processes. Hydrothermal activity along the faults may also be manifested by the presence of higher temperature zeolitic alteration, e.g. analcime, and secondary low albite and quartz, and illite and chlorite instead of smectites. Anomalously high boron contents in smectites could also be evidence of lower temperature hydrothermal activity. The presence of pyrite or other sulfides would also be diagnostic of lower temperature hydrothermal fluid flow.

Summary

The proposed inclined borehole drilling and testing activities will significantly increase our knowledge of the suitability of Yucca Mountain as a site for a repository. Though the holes will not penetrate the repository horizon or deeper units, they will be very valuable in understanding the hydrological role played by the Ghost Dance and Solitario Canyon faults. The important hydrologic differences between fault zones and tuff cannot be properly discerned until more data are in hand on the faults and tuff. The decipherment of the flow pattern in the upper tuff units will help to determine the net infiltration and the pre-emplacement hydrologic conditions, and their effect on the 1000-year pre-emplacement ground water travel time. Investigations of the upper units overlying the repository horizon are also important to the assessment of post-emplacement upward buoyancy flow. The proposed tests can also aid in predicting the movement of gases through the tuff units induced by atmospheric and topographic pumping (Tsang and Pruess, 1986). The results of these tests will aid in the planning of experiments to be conducted in the exploratory shaft.

Cost Estimate

Task 1: **Drilling and Coring**[a]

option 1: $1170 K

option 2: $ 780 K

[a]Based on conversation with Tonto Drilling Co., 1/88; NTS multipliers not included

Task 1A: Shallow shaft, drift and holes: 85K

Task 2: **Hydrological Measurements:**

Operations: $550 K

Equipment: $ 50 K

Task 3: **Seismic Surveys:**

Operations: $111 K

Equipment: $ 50 K

Task 4: **Geochemical Studies:**

Operations: $378 K[b]

[b]Includes isotopic and radiochemical analyses

References

Case, C. M., M. Kautsky, P. M. Kearl, D. M. Nork, T. F. Panian, and S. L. Parker, Unsaturated flow through the alluvium at the Nevada Test Site, Geol. Soc. Amer. Abstracts, v. 16, no. 6, p. 465, 1984.

Montazer, P., E. P. Weeks, F. Thamir, D. Hammermeister, S. N. Yard and P. B. Hofrichter, Monitoring the vadose zone in fractured tuff, Ground Water Monitoring Review, 8, p. 72-88, 1988.

Montazer, P., and W. E. Wilson, Conceptual Hydrologic Model of flow in the unsaturated zone, Yucca Mountain, Nevada, Water-Resources Investigations Report 84-4345, U.S. Geological Survey, Lakewood, CO, 55 p., 1984.

Rulon, J., G. S. Bodvarsson, and P. Montazer, Preliminary numerical simulations of groundwater flow in unsaturated zone, Yucca Mountain, Nevada, LBL-20553, Lawrence Berkeley Laboratory, Berkeley, CA, 1986.

Scott, R. B. and J. Bonk, Preliminary geologic map of Yucca Mountain with geologic Sections, Nye County, Nevada, Open-file Report 84-494, U.S. Geological Survey, Denver, CO, 1984.

Szabo, B. J., Uranium-series dating of fault-related fracture and cavity-filling calcite and opal in drill cores from Yucca Mountain, Southern Nevada, Geol. Soc. Am. Abs. with Program, Ann. Mtg, Reno, NV, v. k 16, no. 16, p. 672-673, 1984.

Tsang, Y. W., and K. Pruess, A study of thermally induced convection near a high-level nuclear waste repository in partially saturated Tuff, Water Resources Research, v. 3, p. 1958-1986, 1987.

Waddel, R. K., J. H., Robison, and R. K. Blankennagel, Hydrology of Yucca Mountain and vicinity, Nevada-California--investigative results through mid. 1983, U.S. Geol. Surv.-WRI-84-4267, Water Resources Invest. Rept., U.S. Geol. Survey, Denver, CO, 1984.
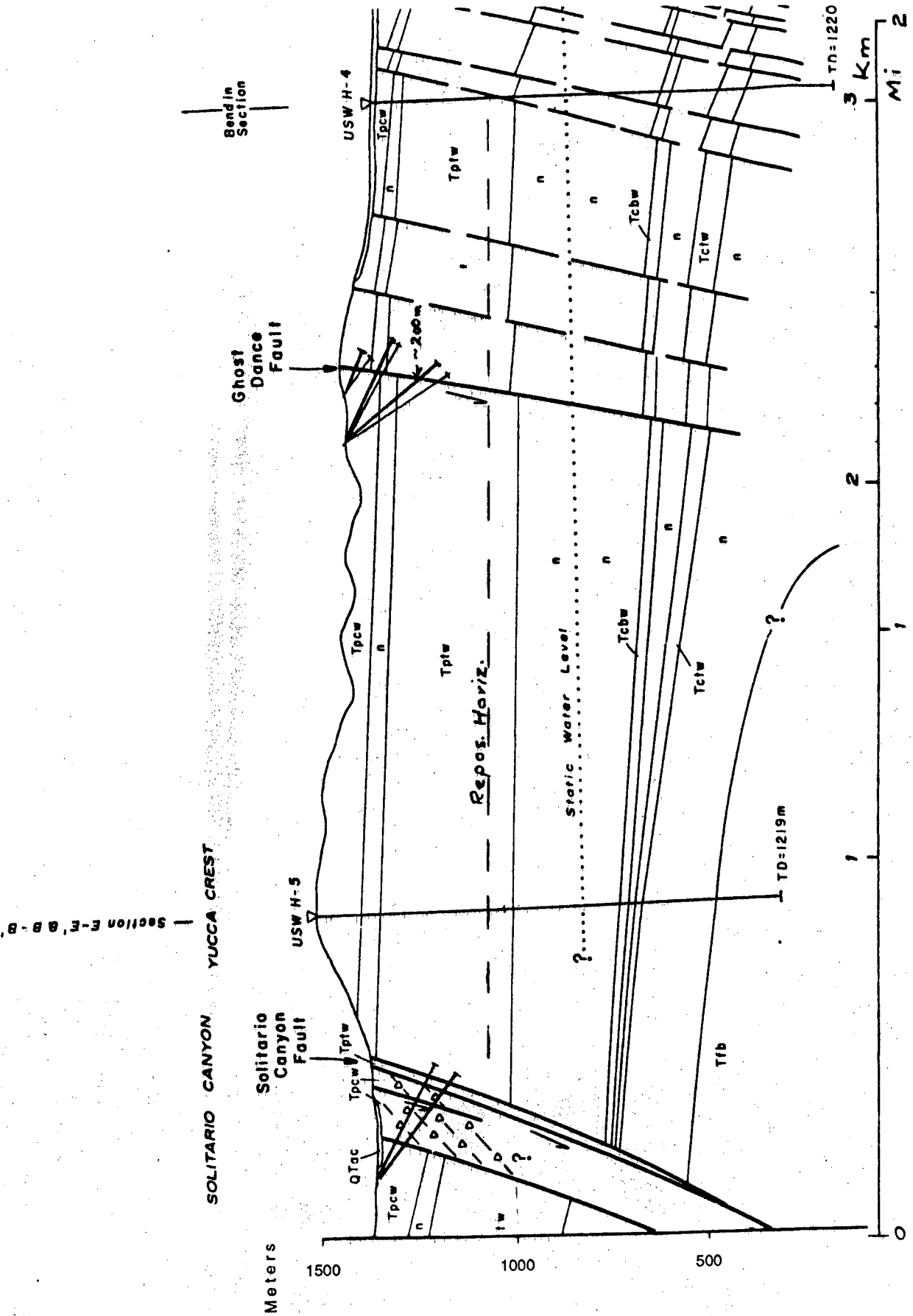
Wang, J. S. Y., and T. N. Narasimhan, Hydrologic mechanisms governing fluid flow in a partially saturated, fractured, porous medium, SAND84-7202, Sandia National Laboratories, Albuquerque, NM, LBL-18473, Lawrence Berkeley Laboratory, Berkeley, CA, *Water Resour. Res.*, 21, pp. 1861-1874, 1985.
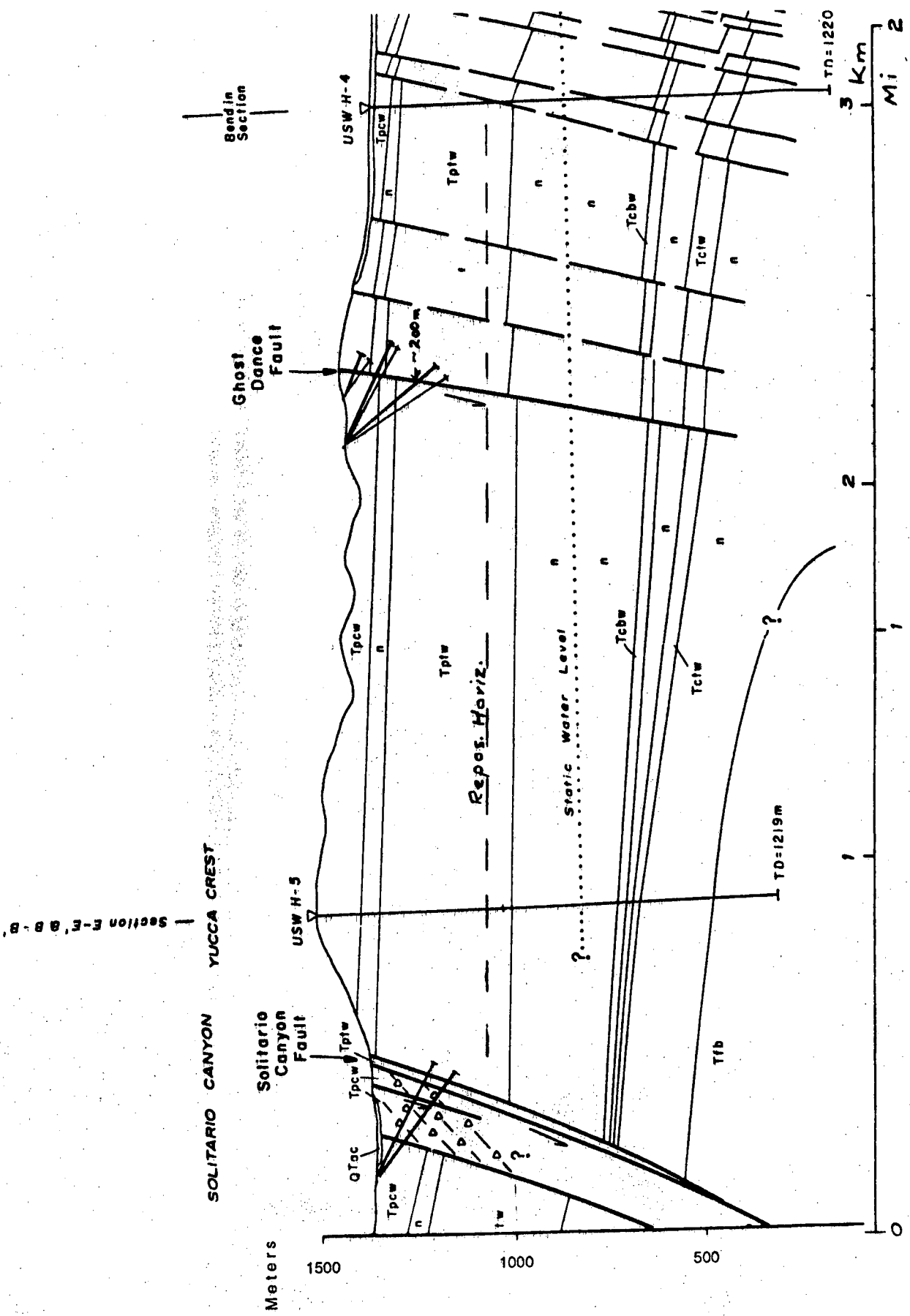
Wang, J. S. Y., and T. N. Narasimhan, Hydrologic mechanisms governing partially saturated fluid flow in fractured welded units and porous non-welded units at Yucca Mountain, SAND85-7114, Sandia National Laboratories, Albuquerque, NM, LBL-21022, Lawrence Berkeley Laboratory, Berkeley, CA 126 p., 1986.

Wang, J. S. Y., and T. N. Narasimhan, Hydrologic modeling of vertical and lateral movement of partially saturated fluid flow near a fault zone at Yucca Mountain, SAND87-7070, Sandia National Laboratories, Albuquerque, NM, LBL-23510, Lawrence Berkeley Laboratory, Berkeley, CA, 122 p., 1987.

Weeks, E. P., Field determination of vertical permeability to air in the unsaturated zone, U.S. Geological Survey Professional Paper 1051, 41p., 1978.

Figure 1.   Cross section through a portion of Yucca Mountain, showing approximate location and attitude of proposed holes (geologic section from Scott and Bonk, 1984).   n = non welded tuff, w = welded tuff, Tpc = Tiva Canyon member, Topopah Spring member, Tcb = Bullfrog member.